

Single Molecule Mechanics on Surface

M.Sc. Kwan Ho Au-Yeung

Dissertation

Submitted to the Faculty of Mechanical Science and Engineering
Technische Universität Dresden

To achieve the academic degree
Doktoringenieur (Dr.-Ing.)

First referee
Prof. Dr. Gianaurelio Cuniberti

Second referee
Prof. Dr. Christian Joachim

Third referee
Prof. Dr. Lukas Eng

Submission: 4 July 2023
Defense: 19 December 2023

Abstract

Single molecule machines on a surface can convert external stimuli into motion, allowing the study on the mechanics of individual small molecules adsorbed on a supporting substrate. Understanding the working principles of synthetic single molecular machines is of fundamental importance to developing nanoscale mechanical molecular devices able to perform work. To investigate the single molecule mechanics, scanning tunneling microscopy (STM) operating at 5 K under ultra-high vacuum (UHV) conditions not only can provide atomic resolution in real space, but also manipulation of atomic matters adsorbed on the surface.

In the first part of this work, the transmission of rotation between single molecule-gears is investigated, where the STM tip pushes the driver gear to achieve rotation. Single molecule-gears under the framework of a star-shaped (five-tooth gear) pentaphenylcyclopentadiene molecule, in which it can be rotated controllably by STM lateral manipulation. For the gear design, anchoring strategies for stabilizing the rotation and the markers for visualizing the rotation from STM images are evaluated. The motion analysis focuses on the interactions between the tip, molecule, and surface.

The second part of this thesis focuses on the dual functionality of the same zwitterionic and chiral molecule species as a molecule-rotor or a molecule-vehicle (nanocar), in which its motion is driven by tunneling electrons. Depending on its adsorption conformation on the Au(111) surface, the chemisorbed rotor exhibits unidirectional rotation, and the physisorbed nanocar can be driven fast in a controlled way. The molecule can work in two different ways induced by STM voltage pulses. By tuning the surface coverage, the conformation of the molecule can be selected to be either rotor or nanocar. Under the same experimental conditions, the dynamics of the rotor and nanocar can be directly compared.

The third part aims at exploring the origin of the unidirectional rotation of a single molecule-rotor adsorbed on the surface. A zwitterionic and chiral molecule-rotor is chosen for its intrinsic symmetry-breaking structure and strong atomic axle on the surface. Random rotation induced thermally by varying progressively the surface temperature, and unidirectional rotation by STM voltages pulses are investigated. To observe the first one-way rotational events, long time measurements/excitation of several hours can determine the possible range of surface temperatures and voltage pulses. By combining both the electronic and thermal excitations, the range of surface temperature and bias voltages can be identified, where the thermal excitation enhances the rate of unidirectional rotation.

Zusammenfassung

Einzelmolekülmaschinen auf einer Oberfläche können äußere Reize in Bewegung umwandeln und ermöglichen die Untersuchung der Mechaniken einzelner kleiner Moleküle, die auf einem Trägersubstrat adsorbiert sind. Das Verständnis der Funktionsprinzipien synthetischer Einzelmolekülmaschinen ist von grundlegender Bedeutung für die Entwicklung mechanischer molekularer Geräte im Nanomaßstab, die Arbeit verrichten können. Um die Mechanik einzelner Moleküle zu untersuchen, kann die Tieftemperatur-Rastertunnelmikroskopie (STM), welche bei 5 K unter Ultrahochvakuumbedingungen arbeitet, nicht nur eine atomare Auflösung im realen Raum, sondern auch eine Manipulation der auf der Oberfläche adsorbierten atomaren Stoffe ermöglichen.

Im ersten Teil dieser Arbeit wird die Übertragung der Rotation zwischen Einzelmolekül-Zahnradern untersucht, wobei die STM-Spitze das Antriebszahnrad antreibt, um eine Rotation zu erreichen. Einzelmolekül-Zahnräder unter dem Gerüst eines sternförmigen (fünfzahnigen) Pentaphenylcyclopentadien-Moleküls, in dem es durch laterale STM-Manipulation kontrolliert gedreht werden kann. Für das Zahnraddesign werden Verankerungsstrategien zur Stabilisierung der Rotation und Marker zur Visualisierung der Rotation aus STM-Bildern bewertet. Die Bewegungsanalyse konzentriert sich auf die Wechselwirkungen zwischen der Spitze, dem Molekül und der Oberfläche.

Der zweite Teil dieser Arbeit befasst sich mit der doppelten Funktionalität derselben zwitterionischen und chiralen Molekülspezies als Molekül-Rotor oder Molekül-Vehikel (Nanocar), wobei die Bewegung durch tunnelnde Elektronen angetrieben wird. Je nach seiner Adsorptionskonformation auf der Au(111)-Oberfläche, erfährt der chemisorbierte Rotor eine unidirektionale Rotation, und das physisorbierte „Nanocar“ kann auf kontrollierte Weise schnell angetrieben werden. Das Molekül kann durch STM-Spannungsimpulse ausgelöst auf zwei verschiedene Weisen arbeiten. Durch Abstimmung der Oberflächenbedeckung kann die Konformation des Moleküls entweder als Rotor oder als Nanocar gewählt werden. Unter den gleichen experimentellen Bedingungen kann die Dynamik des Rotors und des „Nanocar“ direkt verglichen werden.

Der dritte Teil zielt darauf ab, den Ursprung der unidirektionalen Rotation eines einzelnen Molekül-Rotors, der an der Oberfläche adsorbiert ist, zu erforschen. Ein zwitterionischer und chiraler Molekül-Rotor wird aufgrund seiner intrinsischen symmetriebrechenden Struktur und seiner starken atomaren Achse auf der Oberfläche ausgewählt. Untersucht wird die zufällige Rotation, die thermisch durch Variation der Oberflächentemperatur induziert wird, und die unidirektionale Rotation durch STM-Spannungspulse. Um die ersten einseitigen Rotationsereignisse zu beobachten, können Langzeitmessungen/Anregungen von mehreren Stunden den möglichen Bereich von Oberflächentemperaturen und Spannungsimpulsen bestimmen. Durch die Kombination von elektronischer und thermischer Anregung kann der Bereich der Oberflächentemperatur und der Vorspannungen ermittelt werden, in dem die thermische Anregung die Rate der unidirektionalen Rotation steigert.

Contents

1	Introduction.....	11
2	Fundamentals of Scanning Tunneling Microscopy	15
2.1	Brief history	15
2.2	The working principle	15
2.3	Scanning tunnelling microscopy	18
2.4	Scanning tunneling spectroscopy	19
2.5	Manipulation modes.....	20
2.6	Lateral manipulation.....	20
2.7	Manipulation induced by inelastic tunneling electrons.....	21
2.8	Manipulation induced by electric field	23
3	Experimental setup, materials and methods	25
3.1	The systems.....	25
3.2	Substrates	30
3.3	Imaging	31
3.4	STM image processing and data analysis.....	32
4	Single molecule machines on surface investigated by STM	33
4.1	Overview	33
4.2	Molecular design.....	34
4.3	Types of single molecule machines	34
4.4	Gears	35
4.5	Motors/Rotors	37
4.6	Molecule-vehicles (Nanocars)	38
5	Transmission of rotation between molecule-gears	43
5.1	PPCP as a framework for synthesizing molecule-gears.....	43
5.2	Gear 2: PPCP molecule-gears with extended teeth.....	49
5.3	Gear 3: PPCP molecule-gears with chemical marker.....	53
5.4	Gear 4: transmitting motion between three PPCP gears.....	57
5.5	Summary and outlook.....	63
6	A Rotor and Nanocar in One Molecule	65
6.1	Rotors versus Nanocar	65
6.2	Design of the molecule.....	66
6.3	Deposition on Au(111).....	67
6.4	Chemisorbed DMNI-P: Rotor	68

6.5	Interchangeable chirality by flipping the rotor	71
6.6	Chemisorption versus physisorption of DMNI-P	73
6.7	Physisorbed DMNI-P: Nanocar	75
6.8	Action spectra: The role of inelastic tunneling electrons	77
6.9	Exploring the minimum energy for rotation	80
6.10	Electric field induced motion	82
6.11	Summary and outlook	84
7	Thermal and electronic contributions to unidirectional rotation of molecule-rotors	87
7.1	The Maxwell's demon	87
7.2	The Szilárd's engine	88
7.3	The Feynman's ratchet-and-pawl device	89
7.4	Micro-reversibility principle	90
7.5	The rotor unit	93
7.6	Experimental conditions for thermal excitation	94
7.7	Thermal excitation	94
7.8	Interplay between thermal and inelastic electronic excitation	95
7.9	Summary	99
8	Summary and outlook	101
9	Appendix	103
9.1	On surface synthesis: Cyano-vinylene linked chains via Knoevenagel Condensation	103
9.2	Testing non-contact atomic force microscopy and obtaining bond-resolved images	107
10	Bibliography	109
	Scientific contributions	115
	Acknowledgement	119
	Statement of authorship	121

List of abbreviations

DFT	Density functional theory
d^2I/dV^2	Second derivative of tunneling current over bias voltage
dI/dV	Differential conductance
DMBI-P	2-(1,3-dimethyl-1H-benzoimidazol-3-ium) phenolate
DMNI-P	2-(1,3-dimethyl-1H-naphtho[2,3-d]imidazol-3-ium-2-yl) phenolate
DOS	Density of states
fcc	Face centered cubic
HB-NBP	hexa-tert-butyl-pyrimidopentaphenylbenzene
HB-NBP	hexa-tert-butyl-pyrimidopentaphenylbenzene
hcp	Hexagonal closest package
He, LHe	Helium, liquid helium
HOMO	Highest occupied molecule orbital
IETS	Inelastic electron tunneling spectroscopy
LDOS	Local density of states
LT	Low temperature
LUMO	Lowest unoccupied molecule orbital
N₂, LN₂	Nitrogen, liquid nitrogen
nc-AFM	Non-contact atomic force microscope
o-MeI-DMBI-I	2-(2-Methoxyphenyl)-1,3-dimethyl-1H-benzoimidazol-3-ium iodide
PES	Potential energy surface
PPCP	pentaphenylcyclopentadiene
PPCP	pentaphenylcyclopentadiene
SPM	Scanning probe microscope, Scanning probe microscopy
STM	Scanning tunneling microscopy, Scanning tunneling microscope
STS	Scanning tunneling spectroscopy
UHV	Ultra-high vacuum
vdW	van der Waals

List of figures

Figure 1. Outline of this work.	14
Figure 2. Principle of scanning tunneling microscopy.	16
Figure 3. The operation of a scanning tunneling microscope	19
Figure 4. Lateral manipulation by STM tip.....	21
Figure 5. Schematic diagram of inelastic tunneling manipulation.	23
Figure 6. The vacuum and LT-STM setups.	26
Figure 7. Besocke Beetle-type STM scanner.....	28
Figure 8. Pan-slider STM scanner.	29
Figure 9. Photograph of a sample holder.....	30
Figure 10. STM topography (30 nm × 30 nm) of Au(111).....	31
Figure 11. Brief overview of gear fabrication methods in terms of nanotechnology..	35
Figure 12. Chemical structure of a six-tooth molecule-gear HB-NBP.....	36
Figure 13. A molecule-rotor adsorbed on a surface in an STM junction.....	38
Figure 14. The first molecule-vehicle: a molecule-wheelbarrow.	39
Figure 15. Side view of rolling a wheel molecule on the surface	40
Figure 16. The GAZE molecule for the second international Nanocar Race.....	40
Figure 17. Transmission of rotation between molecule-gears on surface.....	44
Figure 18. Structure of the double-decker molecule-motor.	45
Figure 19. Chemical structure of pentaphenylcyclopentadiene.....	45
Figure 20. STM image of PPCP molecules.....	46
Figure 21. PPCP-derivatives.....	48
Figure 22. Overview and the structure of molecule-gear 2 on Au(111).....	49
Figure 23. Motion of molecule-gear 2.....	50
Figure 24. Precise repositioning of molecule by tip manipulation.	51
Figure 25. Train of molecule-gears 2.....	52
Figure 26. Overviews and the structure of gears 3 on Au(111).....	53
Figure 27. Tip-induced debromination on a gear 3 molecule.	54
Figure 28. Non-concentric rotation of a single molecule-gear 3.....	55
Figure 29. Handle behaviour between two molecule-gears 3.....	56

Figure 30. Overviews and the structure of molecule-gears 4 on Au(111).	57
Figure 31. Rotation of a single molecule-gear 4.	58
Figure 32. Stepwise collective rotational sequence between two gears 4.	59
Figure 33. Rotation blocked by the tert-butyl groups	60
Figure 34. Stepwise collective rotational sequence between three gears 4.	61
Figure 35. Co-existence of a molecule-rotor and a nanocar	66
Figure 36. Scheme of o-OMe-DMBI-I undergoing the dissociation reaction	67
Figure 37. STM images of DMNI-P on Au(111) at increasing coverage.	67
Figure 38. Anchoring and rotation of DMNI-P rotor	68
Figure 39. DMNI-P rotor on Au(111).	69
Figure 40. Response time influenced by different adsorption positions.	70
Figure 41. Flipping of the chiral rotor molecule	71
Figure 42. Separation of two different cases of dimers.	73
Figure 43. Lateral manipulation of DMNI-P rotor and nanocar	74
Figure 44. Manipulation of DMNI-P nanocar.	75
Figure 45. Manipulation of DMNI-P nanocar by negative bias.	76
Figure 46. Adsorption geometry of the DMNI-P nanocar.	76
Figure 47. Yield for DMNI-P rotor and nanocar	77
Figure 48. Simulation of vibrational modes	79
Figure 49. Relative tip height time series	81
Figure 50. Threshold voltage for movement versus tip height.	82
Figure 51. Scanning tunneling spectroscopy of the DMNI-P.	83
Figure 52. Maxwell's demon.	87
Figure 53. Szilárd's engine.	88
Figure 54. Schematic drawing of Feynman's ratchet and pawl machine.	89
Figure 55. Schematic potential energy profiles in the simplest pictures.	91
Figure 56. Schematic diagram of DMNI-P rotor chemisorbed on Au(111).	93
Figure 57. Thermal excitation of DMNI-P rotation.	94
Figure 58. Rate over bias voltage at different fixed temperatures.	95
Figure 59. Plots of yield over bias voltage	97
Figure 60. Summary of combining thermal and electronic excitations.	99

List of tables

Table 1. An overview of three types of single molecule machines	34
Table 2. Comparison of PPCP derivatives: motion behaviour and gearing effect.....	63

List of supplementary figures

Figure A 1. Activating chemical reaction thermally on surface	103
Figure A 2. Proposed reaction pathway	104
Figure A 3. Overview STM images.....	105
Figure A 4. Structure of a CN-vinylene-linked trimer.....	105
Figure A 5. Scheme of a qPlus sensor.	107
Figure A 6. Frequency sweep for identifying the resonant frequency (f-center).....	108

1 Introduction

“What would happen if we can arrange the atoms one by one the way we want them” [1] was one of the early quotes about nanotechnology raised by R. P. Feynman in his inspiring talk in 1959. Nowadays, the state-of-art techniques in nanotechnology such as ion trap [2], optical [3] or magnetic [4] tweezers, and scanning probe microscopy (SPM) [5,6] demonstrate the fascinating possibilities to manipulate individual atoms or molecules, and ultimately build up a nano-scale device.

In this sense, what would happen if we can control an individual molecule which is capable of harnessing energy from local external stimuli and converting it into mechanical motion, such as rotation and translation [7-9] as a “machine”? Such a “single molecule machine” can be precisely arranged and positioned, allowing for controlled interactions and transmission of motion, eventually performing useful work [10]. Indeed, the advent of single molecule machines opens up unprecedented opportunities for advancements in physics, chemistry, nanotechnology, materials science, and other disciplines, leading us towards a future where atomic level engineering holds the key to potential molecular or quantum devices [11]. Nonetheless, before reaching the next level for engineering molecular devices, the detailed molecule mechanics has to be understood from the efforts of both experiments and theories. To achieve the sub-nanoscale control and visualization experimentally, a technique working as an “atomic finger” is one of the possibilities.

In order to probe the mechanics of a single molecule in real space, scanning tunneling microscopy (STM) is the state-of-the-art instrument that can provide atomic resolution in between the quantum tunneling junction (typically less than 1 nm spatial separation) of an atomically sharp metallic tip and a conductive surface [12]. This technique invented by G. Binnig, H. Rohrer, E. Weibel, and C. Gerber in 1981 (G. Binnig and H. Rohrer were awarded the Nobel Prize in Physics in 1986) has revolutionized the fields of, but not limited to, surface physics [13], materials science [14], solid-state quantum computing [15,16], and biology [17].

STM provides not only atomic resolution in real space, but also the possibility of manipulating atoms/molecules (e.g., moving them one by one). After the demonstration of positioning Xe atoms on a Ni(111) surface by D. M. Eigler and E. K. Schweizer in 1990 for “writing” the logo of “IBM” [5], atomic and molecular manipulation becomes a hot topic because of its revolutionary ability to see and build atom by atom (Chapter 2). This method (not limited only to solely STM, but incorporation also with ultra-fast optical and magnetic setups) benefits the

fundamental single-molecule studies of, e.g., vibrational and electronic excitations [18] [19], electron spin resonance [20], photocurrent excitation [21,22], and more.

On the other hand, careful choices of technical setups (Chapter 3) are essential for investigating the ultra-fast and sub-nanoscale motions of single molecules. The presence of a supporting substrate is beneficial for single molecular components, for examples, molecular switches, gears, rotors, motors, and vehicles. The atomic arrangement of such surfaces becomes a crucial parameter in the quantum world [23] [24]. For a cryogenic system operating at low temperature near absolute zero (liquid helium) where thermal diffusion of molecules is unfavorable unless the application of external stimuli, stepwise movements of molecules can be realized. In this sense, an ultra-clean environment is a crucial prerequisite, otherwise the cold system will be covered by ambient molecules in less than a second.

A single organic molecule is an assembly of atoms that can move together, exhibiting classical motion by quantum processes, and therefore, it is called semi-classical mechanics (Chapter 4). For a single molecule supported or spatially confined on a surface (i.e., an almost 2D space), classical mechanical motion as a final state triggered by STM tip-induced manipulation, translation, and rotation can be observed. Inspired by macroscopic machines, molecule-gears, rotors/motors, and nano-vehicles (Nanocar) can be investigated but with completely different mechanisms (Chapters 5 – 7).

The recent honor of Nobel Prize in Chemistry (2016) given to the three pioneers B. L. Feringa, J. F. Stoddart, and J-P Sauvage "for the design and synthesis of molecular machines" has raised even more potential interests of molecular machines ranging from fundamental quantum science [6,11,25-29], materials science [30,31], to biomedical applications [32-34]. As a focus of this work, single-molecule studies should be distinguished from the measurements on assembly of molecules or in bulk, in which individual molecules can be investigated, in contrast to only the average characteristics of molecules.

This thesis is structured as follows:

Chapter 2 explains the fundamentals of scanning tunneling microscopy (STM) as an experimental tool used in this work. Scanning tunneling spectroscopy (STS), and manipulation modes will be elucidated. Chapter 3 addresses the experimental methods and setup details, including the ultra-high vacuum setup, the cryostat for low-temperature (typically $T = 5$ K) measurement, and STM scanners.

Chapter 4 points to the key concept of STM investigation on single molecule machines adsorbed on the surface, and provides an overview, including a literature review, on

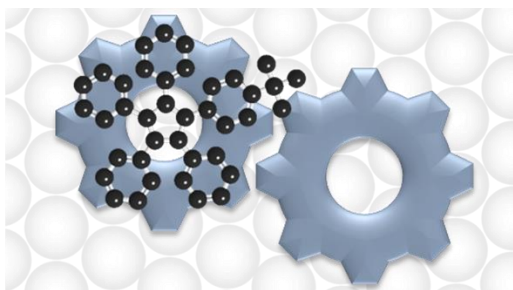
three main types of single molecule machines: molecule-gears, molecule-rotors, and molecule-vehicles (Nanocar).

Chapters 5 – 7 consist of the key findings and details of this work. In Chapter 5, motivated by fabricating molecular mechanical devices, single molecule-gears supported by the Au(111) surface will be presented. By designing gears with 1.2 – 1.3 nm diameter in the framework of star-shaped pentaphenylcyclopentadiene (PPCP), it allows the investigation of the interlocking between the five-tooth gears by LT-STM, and the corresponding motion on the Au(111) surface.

Chapter 6 shows two other classes of single molecule machines: molecule-rotor and molecule-vehicle (“Nanocar”). The studied molecule is a single-molecule machine with two distinct functionalities, i.e., a rotor and a nanocar, depending on its conformations on the Au(111) surface. Such dual functionality allows the comparison of inelastic electrons tunnelling excitation for a controlled translation or a unidirectional rotation on the same molecule and in the same experimental conditions. It is a rare case that the same molecular species can work as a molecule-rotor or a nanocar powered by inelastic tunneling electrons and/or electric field, depending on their adsorption geometries on Au(111).

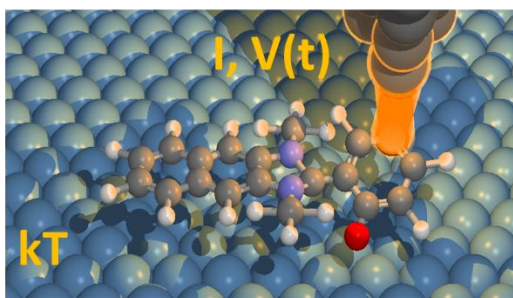
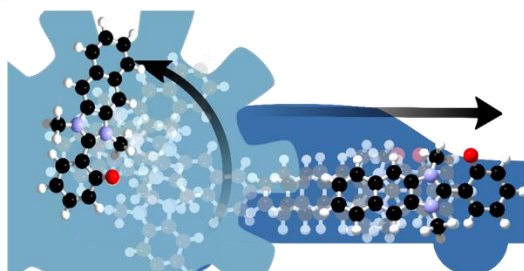
Chapter 7 presents an in-depth study on the origin and the processes of unidirectional rotation will be elucidated, leading to possible new perspectives on how a molecule-rotor rotates. Aiming at exploring the limit of the law of thermodynamics, the interplay between STM electronic and thermal excitation for unidirectional rotation of a molecule-rotor will be explained.

Finally, Chapter 8 summarizes the key findings, and illustrates the perspectives on the ongoing and future works.



Chapter 5:
Transmission of rotation
between molecule-gears

Chapter 6:
A rotor and nanocar in
one molecule



Chapter 7:
Thermal and electronic
contributions to unidirectional
rotation of molecule-rotors

Figure 1. Outline of this work.

2 Fundamentals of Scanning Tunneling Microscopy

This chapter explains the fundamentals of scanning tunneling microscopy (STM). It addresses different measurement modes and their data interpretations. Furthermore, descriptions of STM as a tool of atomic manipulation shall be presented.

2.1 Brief history

“But I am not afraid to consider the final question as to whether, ultimately – in the great future – we can arrange the atoms the way we want; the very atoms, all the way down!” R. P. Feynman in 1959 at his visionary talk [1].

Scanning tunneling microscopy (STM) is an experimental scanning probe technique based on the quantum phenomenon of tunneling. It was invented in 1981 by G. Binnig, H. Rohrer, E. Weibel and C. Gerber at IBM in Zurich, Switzerland [35]. G. Binnig and H. Rohrer were awarded the Nobel Prize in Physics in 1986. Following the first STM image of the atomic structure of the Si(111)-(7 × 7) surface by G. Binnig, H. Rohrer, E. Weibel, and C. Gerber [13], this advance has allowed us to visualize single atoms and molecules in real space with sub-Angstrom resolution. In 1990, the first positioning of single Xe atoms on a Ni(110) surface with a low-temperature STM (4 K) by D. M. Eigler and E. K. Schweizer [5] revealed the great potential - “The processes (atomic manipulation) we describe are in principle applicable to molecules also.” (Molecular manipulation is of focus in this thesis). Given the vision from the prior efforts, STM has become - and still is - the state-of-the-art technique in materials science, physics, chemistry, biology, and engineering.

2.2 The working principle

Quantum tunneling was discovered long before the invention of STM. Following the birth of quantum theories in the early 1900s, physicists found out the wave-particle duality of particles and electrons. Several microscopic physical effects can only be explained by the wave-particle duality according to de Broglie [36]. Tunneling effect is one of the first examples predicted by theories and soon confirmed by experiments. Examples like auto-ionization of excited states of atomic hydrogen under a strong electric field [37], field emission from metals under an electric field [38], and α -decay of heavy nuclei [39] have been the first applications of the tunneling theory.

An overview of theoretical treatments of electron tunneling is important for understanding STM. As shown in the schematic diagram for the one-dimensional case (Figure 2a), it allows an electron in real space, coming from region **I**, to pass through a potential barrier (region **II**), then eventually can be found in region **III** with decreased amplitude. In other words, contrary to classical physics (e.g., a ball hitting a brick wall), the electron is not blocked by the potential barrier, but instead, a part of the wave function is “permitted” to reach region **III** with a lower probability to find it.

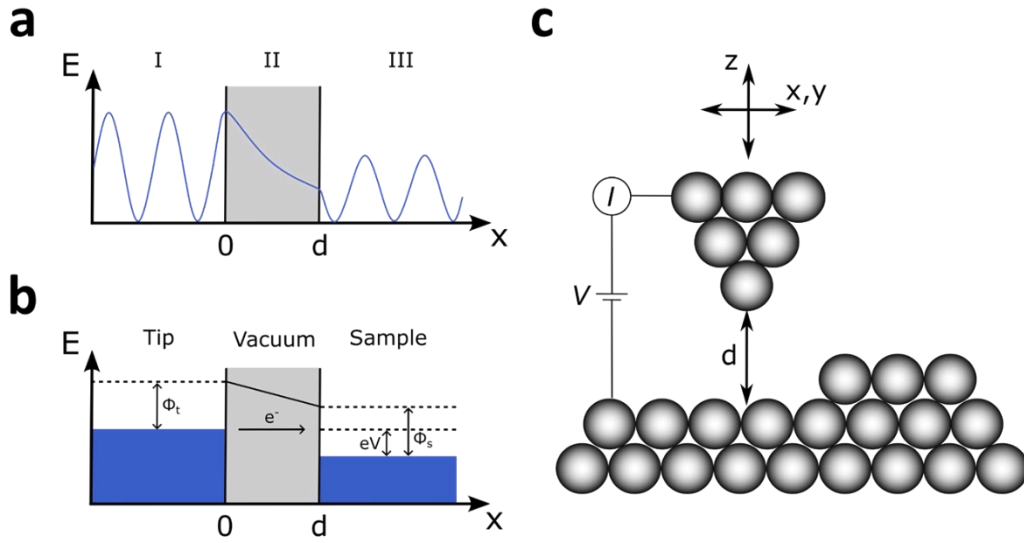


Figure 2. Principle of scanning tunneling microscopy. (a) Energy diagram of the general tunneling phenomenon. (b) Energy diagram for a general scanning tunneling microscopy, including tip, (vacuum) barrier, and sample. (c) Illustration of the general setup. An atomic shape tip (one atom at the tip apex) can scan laterally (x, y). The distance d between the tip apex to the sample is controlled by the z -position of the tip.

The original idea from the inventors of the STM was to use the tunneling effect for developing a new spectroscopic method in real space [40]. From the view of STM, region **II** represents the tunneling gap between an STM tip and a sample as depicted in Figure 2b. Given the two rectangular barriers as the simplest case, the electron states of both electrodes (tip and sample respectively) are filled up to the Fermi energies $E_{F,T}$ and $E_{F,S}$. In particular (Figure 2c), bias voltage V can be applied to the metal-vacuum-metal (tip-vacuum-sample) junction, also known as tunneling junction, where it allows the electron to tunnel through the barrier. The bias polarity defines the direction of the electron flow: positive bias generates a net flow of electrons going from the tip to the sample. Hence, the tunneling current I can be measured.

To theoretically understand the origin of atomic resolution achieved by STM, a solution for the tunneling probability can be obtained by solving the time-independent

Schrödinger equation [12]. For the one-dimensional case, transmission coefficient T exponentially depends on the thickness of the barrier d , giving the results:

$$T \propto e^{-2kd} \text{ with } k = \frac{\sqrt{2m_e\phi}}{\hbar} \quad (2.1)$$

m_e is the mass of an electron, ϕ is the average work function of the two electrodes, and \hbar is the reduced Planck constant (obtained from the Planck constant h divided by 2π). For example, a typical barrier height of metals work function is about 5 eV, and the transmission coefficient changes of one order of magnitude for $d = 1 \text{ \AA}$. For gold as a substrate used in this work, $d = 1.0003 \text{ \AA} \pm 0.0075 \text{ \AA}$ reaches the factor of 10. As a result, such exponential dependence of tunneling probability and barrier distance in real space gives a strong contrast, and thus the sub-nanometer resolution of STM.

Based on the formalism from J. Bardeen [41] and later used by J. Tersoff and D. R. Hamann [42], the tip and sample are separated parts of the system. In this model, there are two electron wave functions ψ_t and ψ_s for tip and sample, respectively. If both are far apart from each other, the corresponding electron wave functions will decay exponentially into the barrier, i.e., no tunnelling between the two. The presence of a counter-electrode is treated as a perturbation potential for the respective unperturbed states. Hence, the probability that an electron is transferred from one electrode to the other is related to the tunneling matrix element $M_{t,s}$.

$$M_{t,s} = -\frac{\hbar}{2m_e} \int (\psi_t^* \nabla \psi_s - \psi_s \nabla \psi_t^*) d\vec{S} \quad (2.2)$$

The integral is calculated over any surface separating tip and sample in the barrier passed by the whole tunnelling current. Therefore, the tunnelling current can be expressed as:

$$I = -\frac{4\pi e}{\hbar} \int_{-eV}^0 |M_{t,s}|^2 \rho_t(\epsilon) \rho_s(\epsilon + eV) (f(\epsilon) - f(\epsilon + eV)) d\epsilon \quad (2.3)$$

This expression introduces the density of states (DOS) ρ for the tip and sample. And in the following step, we can further simplify Eq. 2.3 by assuming the tunnelling matrix reflects the probability of the electron tunneling from one electrode to the other (Figure 2a). In other words, the matrix can be simplified as the exponential function in Eq. 2.1. The DOS of the metallic tip can be approximately considered to be energetically flat around the Fermi energy, which can be assumed as constant. The following is the result of the model:

$$I = -\frac{4\pi e}{\hbar} e^{-2kd} \rho_t(0) \int_{-eV}^0 \rho_s(\epsilon + eV) (f(\epsilon) - f(\epsilon + eV)) d\epsilon \quad (2.4)$$

Importantly, this equation reveals that the current is not only exponentially dependent on the tip-surface distance, but also dependent on the integral of the DOS of the sample.

2.3 Scanning tunneling microscopy

In terms of “imaging”, the essential element is the contrast of the object of interest compared to the rest of the measured area. The origin of the word “microscope” came from the rise of the optical microscope in the 1600s [43], the contrast is defined by the light-matter phenomenon. In STM, the contrast is defined by the local density of states of the sample (LDOS) during scanning. Thanks to the exponential dependence of the tunneling current (Eq. 2.1), about 1 Å distance change between tip and sample gives a change in transmission coefficient a factor of 10. This essentially relates to the contrast difference of STM, leading to the sub-Angstrom resolution. Experimentally, such a small signal is filtered and amplified by a factor of 10^9 V/A.

In general, “imaging” or “scanning” of STM means that after defining the size of the area of interest and the number of pixels ($x_n \times y_n$) at a certain I, V set point (constant current mode), the tip travels end-to-end (x_1 to x_n) of the area of interest as a “line”. After the first line, the tip will continue scanning starting at the next nearest pixel (from y_1 to y_2) as the second line (again from x_1 to x_n), and so on (y_n). Depending on the setup, the typical scanning direction is from top to bottom or bottom to top. The scanning time of an image is typically in the range of minutes.

There are two different operation modes:

Constant current mode:

Constant current mode is the most common measurement mode, where a feedback loop is employed to keep the tunneling current constant. To achieve this, a piezoelectric controller regulates the z position of the tip based on the I, V set point by keeping I constant (as well as V). The advantage is the possibility of tip crash is lower than using constant height mode, especially without enough knowledge of the desired scan area. In this case, the effective signal is the topography, or tip-height difference, z .

Constant height mode:

In constant height mode, the feedback loop is switched off. In this case, the tip scans across the sample at a fixed height. Special care (considering the tip-surface and tip-molecule distances) is required to avoid unintentional tip crashes. This mode is often used for high-resolution imaging (e.g., CO-functionalized tip) or fast scanning. In this case, the effective signal is the tunneling current I .

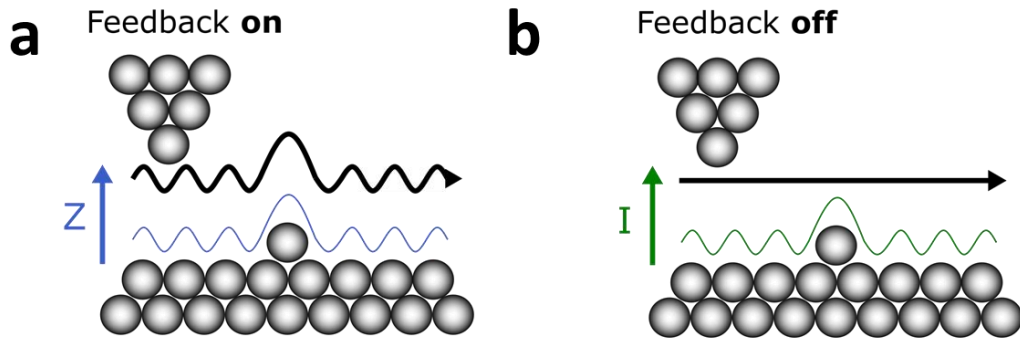


Figure 3. Schematic representation of the operation of a scanning tunneling microscope in (a) constant current mode and (b) constant height mode. (a) In constant current mode, topography (difference of tip height z as effective signal) over a surface will be recorded. (b) In constant height mode, tunneling current as an effective signal over a surface will be recorded.

2.4 Scanning tunneling spectroscopy

Following the results from Eq. 2.4, STM does not measure the physical height of the sample, but the LDOS with the nanoprobe. In the first years of intense research after the birth of the STM, the interests were mainly focused on semiconductors [44]. It was very soon to notice that for semiconductors, the STM topographies depend essentially on the applied voltage bias between tip and sample due to the relatively large semiconducting bandgap. The first work in 1985 was performed by R. S. Becker and co-workers, where the surface states of Si(111)-(7 × 7) surface were imaged [45]. The different bandgap V -dependent signatures of materials give rise to a novel method for locally probing the DOS of materials, or in this work, the electronic resonances of single molecules/adsorbates.

Theoretically, by taking the first derivative of Eq. 2.4, it yields

$$\frac{dI}{dV} = -\frac{4\pi e}{\hbar} e^{-2kd} \rho_t(0) \int_{-eV}^0 \rho_s(\epsilon + eV) \frac{\partial f}{\partial \epsilon} d\epsilon \quad (2.5)$$

The differential conductance dI/dV depends on the LDOS of the sample. Experimentally, the dI/dV signals can be obtained by the lock-in amplifier. During the measurement, the tip can be placed in the desired x,y position. Then by defining the parameters I and V at a certain tip height, the feedback loop is switched off (i.e., constant height mode). The lock-in amplifier supplies an additional sinusoid bias modulation V_{mod} to the applied bias V_0 at a certain frequency ω . By expanding a Taylor series of $I(V)$:

$$I(V) = I(V_0) + \frac{dI(V_0)}{dV} V_{mod} \sin(\omega t) + \frac{d^2 I(V_0)}{dV^2} V_{mod}^2 \sin^2(\omega t) + \dots \quad (2.6)$$

The first derivative is obtained by the second term of the Taylor series. Since the lock-in technique acts as a bandpass for the applied frequency, the current is proportional to dI/dV and can be spontaneously measured during the measurement. As a result, a plot of dI/dV over the sweep of bias voltage can be obtained.

By measuring all the I/V signal over a certain area (x, y) , the STM can “map” the dI/dV signal in the sub-Angstrom scale. This can be done experimentally by employing the lock-in amplifier when imaging the area of interest. Therefore, one can obtain the dI/dV map at each pixel spontaneously with the standard topography at a fixed applied bias voltage.

2.5 Manipulation modes

STM does not only allow imaging conductive surfaces and molecular adsorbates with high spatial resolution, but also provides a nanoscale probe able to manipulate matter at the atomic scale. Note that for manipulation, it is only possible to do at low temperature under ultra-high vacuum (UHV) conditions for minimizing the thermal diffusion of molecules. (The UHV system aims at preventing unwanted adsorbates that are physisorbed on a cold surface.) Recent advances have shown that tip manipulation can induce chemical reactions, translate, rotate, and switch single molecules on surfaces. The following sections explain the different modes of tip-induced manipulation: lateral manipulation, inelastic tunneling, and electric field.

2.6 Lateral manipulation

The lateral manipulation mode involves atomic forces, e.g., van der Waals (vdW) forces that can position single adsorbates [46]. By employing this technique, the first example was conducted by D. M. Eigler and E. K. Schweizer from IBM in California, the USA, positioning 35 individual Xenon (Xe) atoms on a Ni(110) surface to “write” the logo

“IBM” [5]. During the process, the tip is brought near to the surface (typically 3 – 5 Å) and the tip moves laterally across the surface. The parameters for moving single molecules are in the range of 1 nA and 10 mV (resulting tunneling resistance $R = 10\text{ M}\Omega$) at constant current mode.

The lateral manipulation procedure involves three steps: (1) allowing the tip to approach the molecules vertically under a small bias to increase the tip–molecule interactions, (2) laterally driving the tip parallel to the surface in a precisely controlled trajectory, and (3) retracting the tip to normal scanning position. Note that it is also possible to operate at constant height mode, but special care (considering the tip–surface and tip–molecule distances) is required to avoid unintentional tip crashes. Since vdW forces can be attractive or repulsive, different lateral manipulation modes can be achieved: pushing, pulling, and sliding. Pushing mode involves repulsive interactions; pulling and sliding modes involve attractive interactions.

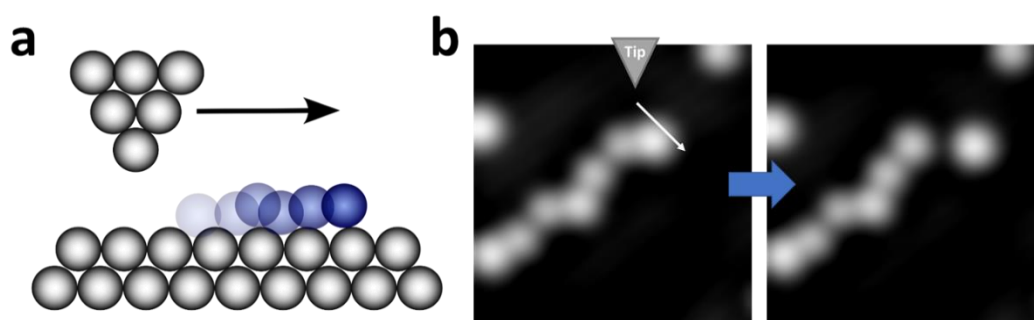


Figure 4. Lateral manipulation by STM tip. (a) Schematic diagram of tip-induced lateral manipulation. The blue ball illustrates as an adsorbate on the surface. (b) Pushing one Bromine (Br) atom out of a chain of Br atoms experimentally at $T = 5\text{ K}$ on the $\text{Au}(111)$ surface. Parameters: $V = 10\text{ mV}$, $I = 8\text{ nA}$.

2.7 Manipulation induced by inelastic tunneling electrons

While lateral manipulation has the advantage to position single molecules along a certain distance on surfaces, manipulation by inelastic tunneling electrons can also provide valuable information, such as the mechanical and electronic properties, of the adsorbates.

Recently, there are still ongoing debates, for examples, about the cooperative electric field and inelastic tunneling effects on the movement directionality of molecules [47] [7], and the origin of molecular motion and excitation modes [29]. Given that the molecular “classical” motion (e.g., rotation and translation) can be visualized by recording subsequent images, such semi-classical complexity includes the questions about tunneling mechanism, electrostatic mechanism, the properties of molecules adsorbed on metal surfaces based on their unique designs, thermodynamics, and

more. In the last two International Nanocar Race [48-50], organic chemists and physicists were able to separately study more than 10 different structural and conceptual molecule-vehicles worldwide. These gave a great opportunity for comparing molecules driven by STM tips, and more importantly, investigating the fundamental mechanism of how a molecule moves. All these also define a major extent of the motivation in this work (Chapters 5 and 6).

For elastic tunneling electrons, the energy of the electron is conserved, meaning that the initial filled state and the final empty state have the same energy. In contrast to elastic tunneling electrons, inelastic tunneling electrons lose energy, for example, to vibrational modes during the tunneling process. For tunneling current $I = 1$ nA, the average time interval between two electrons transfers events is 0.1 ns, giving a 10^{-4} inelastic efficiency [51]. Hence, on average one electron/ 10^{-6} s can deliver energy from inelastic tunneling electrons to vibrational modes of the adsorbates, e.g., single organic molecules, leading to chemical reactions, conformational changes, or motions on surfaces [52-56]. Furthermore, more than a tool for simply moving single molecules, analyzing the parametric dependence of the excitations can retrieve the intrinsic properties of the molecules, for examples, different vibrational modes and the threshold of excitation [57,58]. This type of analysis can be done by plotting the “action spectroscopy” [58] and will be discussed in Chapters 6 and 7.

In the case of tunneling into resonances, the adsorbate undergoes an electronic transition into an excited state. During relaxation, the adsorbate can dissipate the energy by hopping to another position on the surface. Furthermore, it is possible for the inelastic tunneling electrons to excite and move single molecules at the vibrational regime (V -dependent also), where the energy in this regime is lower than the energy of the electronic resonances.

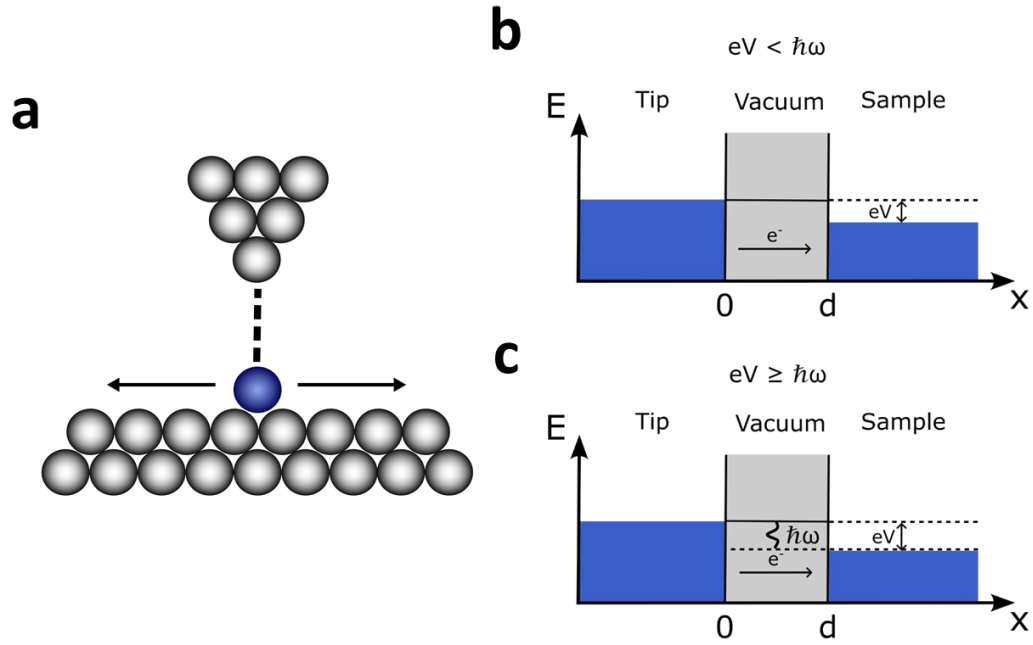


Figure 5. (a) Schematic diagram of inelastic tunneling manipulation. Blue ball illustrates as an adsorbate on the surface. (b – c) Elastic and inelastic tunneling through a tunneling barrier (vacuum) between two electrodes (tip and sample). $\hbar\omega$ corresponds to the energy of a vibrational quantum. (b) For energies below $\hbar\omega$, only the elastic channel is available. (c) At energies higher than or equal to $\hbar\omega$, the inelastic channel is opened.

2.8 Manipulation induced by electric field

When a bias voltage is applied, a static electric field is generated between the tip and the surface. Due to the distance between tip and surface, the electrostatic field generated locally and experienced by the atoms and adsorbates on the surface is huge (in the range of 10^7 V/cm). For molecules having a large intramolecular charge separation or dipole moment, one can excite and move single molecules controllably on the surface by using electric field [47]. Note that such effect is also polarity dependence.

3 Experimental setup, materials and methods

It is of importance to maintain a dirt-free environment with the minimum thermal effect and nanoscale stability for the single molecule experiments. In this chapter, the design of the vacuum chambers, the scanning tunneling microscopy, and materials will be described.

3.1 The systems

The custom-built low-temperature scanning tunneling microscope under ultra-high vacuum (UHV) conditions (CreaTec Fischer & Co. GmbH, Industriestr. 9, 74391 Erligheim, Germany) was used for all the results.

3.1.1 Ultra-high vacuum systems

All the experiments were carried out under ultra-high vacuum (UHV) conditions, i.e., with a base pressure of about 1×10^{-10} mbar. A combination of different pumps for different vacuum systems has been employed as depicted in Figure 6. Such setup can be divided into three units separatable by the all-metal gate valves: load-lock, preparation chamber, and STM chamber. This is beneficial for different preparation processes such as sample cleaning, deposition of molecules, and transfer of samples from the ambient environment, together with the individual pressure monitoring by ionization gauges at each unit. The load-lock can be evacuated by the turbo molecular pump coupled with the rough pump ($\sim 1 \times 10^{-2}$ mbar), which can reach up to 1×10^{-8} mbar. A combination of ion-getter pumps with the titanium sublimation pumps (TSP) maintains the preparation and STM chambers at the low to mid 10^{-10} mbar range. Together with the low-temperature effects (“cryo-getter effect”) from the cryostat in the STM chamber, 1×10^{-10} to 10^{-11} mbar can be achieved.

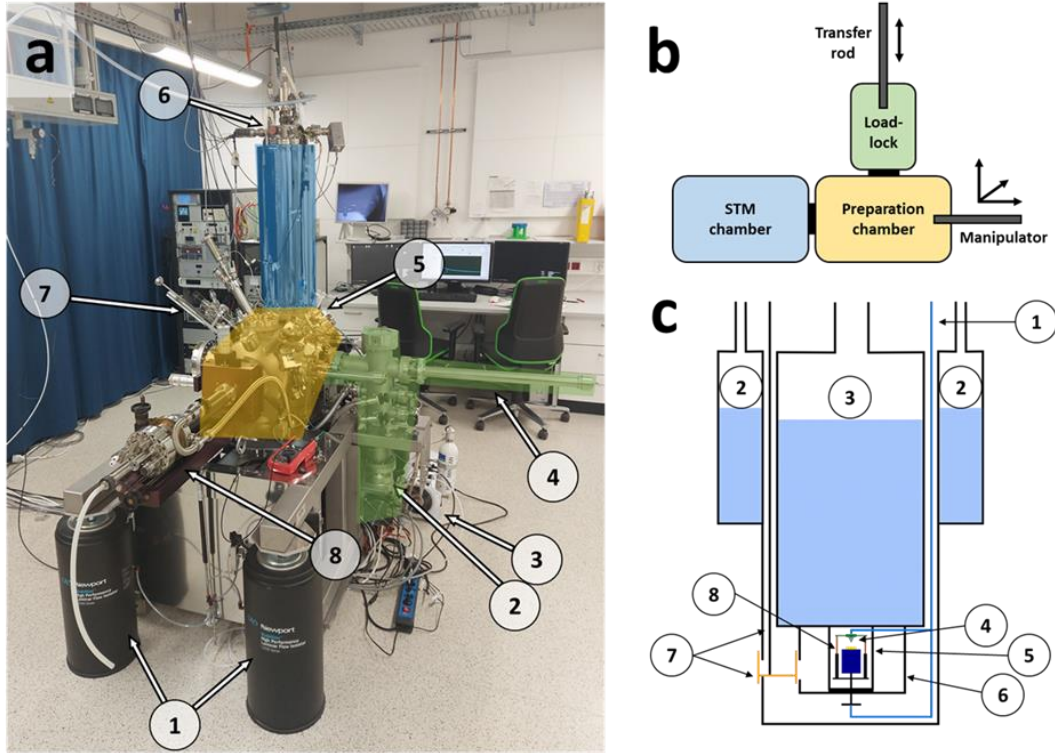


Figure 6. The vacuum and LT-STM setups. (a) Photograph of the vacuum setup. 1: Pneumatic feet. 2: Molecular turbo pump. 3: Rough pump coupled to the turbo pump. 4: Horizontal transfer rod at the load-lock. 5: Sputter gun. 6: Electronic feedthrough for STM operation. 7: Molecular evaporator. 8: Manipulator at the preparation chamber. (b) The three colours in (a): blue, orange, and green represent the three chambers schematically. (c) Sketch of the STM and cryostat system. 1: Push-pull mechanism. 2: LN₂ reservoir. 3: LHe reservoir. 4: STM. 5: Inner cryo-shield held at LHe temperature. 6: Outer cryo-shield held at LN₂ temperature. 7: The shutter gates are opened by the wire from the top.

3.1.2 Load-lock

The load-lock is designed for the transfer of materials (such as STM tips and substrates) from the ambient to the UHV environment, or vice versa. The turbo molecular pump coupled with the rough pump can differentially pump the molecular evaporator, the manipulator, and the gas lines. The transfer rod can be used to horizontally carry the materials in the direction of the preparation chamber. It is perpendicular to the direction of the manipulator in the preparation chamber for further transfer of materials. A heating lamp is also equipped for degassing materials from ambient.

3.1.3 Preparation chamber and components

The preparation chamber consists of several components: a manipulator, a storage, a sputter gun, a metal evaporator, and a Knudsen cell molecular evaporator. The

manipulator (x, y, z, θ) can be used for positioning materials inside the preparation and STM chambers. With the electrical feedthrough at the head, one can apply power (I, V) for annealing the substrates (i.e., resistive heating). The storage can be used to hold six STM tips and five sample holders in the preparation chamber. A specific slot of the storage has the option for the electrical feedthrough. In addition, the storage has a built-in filament for preparing oxidized tungsten tips by electron bombardment.

For preparing the samples, the sputter gun can remove the uppermost layers of the Au crystal and adsorbents. Single metal adatoms can be deposited on the surface by the metal evaporator. To deposit organic molecules, evaporation can be achieved by employing the Knudsen cell molecular evaporator, typically in the range of 100°C – 300°C depending on the nature of the synthetic molecules (e.g., mass and estimated decomposed temperature).

For estimating the amount of molecules deposited, a quartz-crystal microbalance in front of the molecular evaporator can be employed to detect the mass-sensitive frequency change (sensitivity in the range of ± 0.1 Hz) upon evaporation. The quartz crystal is driven to oscillate at about 6 MHz. By monitoring the resonance frequency during evaporation, deposition parameters can be optimized efficiently. Moreover, for analyzing the gas composition, a mass spectrometer is available.

3.1.4 STM Chamber

The goal of reaching 5 K is achieved by a two-stage cryostat coupling to the STM. The outer cryostat is filled with liquid nitrogen (LN_2), which has a capacity of 14 L. The inner cryostat is filled with liquid helium (LHe), which has a capacity of 4 L. The usual consumption of LHe is 100 mL/h, allowing about 80 h of cooling time until the next refill. To decouple the 5 K-cooled STM to the outer environment at room temperature (RT), a shutter can be opened for transferring samples. The electrical cabling of the STM is led through the cryostat. During measurement, the STM scanner is hung with three springs, where this setup provides a high mechanical vibrational damping of the scanner. A push-pull mechanism controls the position of the STM scanner for transfer, in which it has to be mechanically restricted. In order to isolate the mechanical noise outside of the chambers, the whole setup is supported by four pneumatic feet, and the STM scanner is stabilized by the eddy current damping system. This vibration isolation system is the essential effort to obtain a vertical resolution of 0.01 pm in STM, where stability of the tip-sample spacing at 0.001 pm is desired [12].

3.1.5 STM scanners

Before 2021, we used the Besocke Beetle-type [59,60] design as the STM head (Figure 7) in the laboratory (Barkhausen Bau, TU Dresden). The slip-stick motion of the piezo-

materials enables the coarse approach of the tip towards the sample, where such coarse motion uses the non-flat ramp formed by three segments with a slight angle. The complete stroke of the z-coarse approach is around 0.6 mm. In the center of the ramp, the inner piezoelectric tube is placed. This tube regulates the fine approach while the STM tip is held by magnets on this tube, achieving the tunneling distance between the tip and the sample in the range of 5 - 10 Å. The lateral (x,y) motion is controlled by the three outer tubes in order to reduce the noise level.

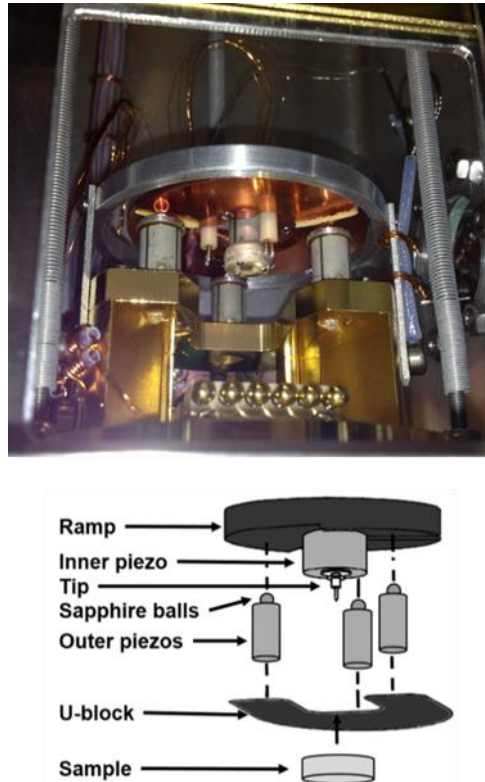


Figure 7. Besocke Beetle-type STM scanner. Upper: Photograph of the STM without housing. Three outer piezo tubes can be clearly seen. Lower: Schematic drawing of the design.

In December 2021, the STM head was replaced by a Pan-slider type scanner [61] (Figure 8). The vertical (z) moving part is a sapphire prism containing a tube piezo scanner. The stepping is actuated by six shear piezo stacks. While the original design did not allow for coarse x,y-motion of the sample relative to the tip, a lateral moving table was constructed using shear piezo elements.

Thanks to the decoupling of the lateral motion, the major advantage of the Pan-design over the Besocke Beetle-design provides more reliable and stable z-motion. For the Besocke Beetle-design, if the ramp ring is rotated downwards for the approach (z-motion), this motion is always accompanied by a slight unintentional shift in the lateral direction and vice versa. In practical use, retraction of the tip is usually necessary when

switching between different operation modes, for example, from STM to non-contact atomic force microscopy (nc-AFM) modes or vice versa. Hence, the Pan-design allows the users to approach the tip to the same scanning area or even the same desired single molecule, which is usually critical when using the Besocke Beetle-type. In other words, the new scanner head is beneficial and flexible for employing additional functions like nc-AFM (Chapter 9 shows the tests of nc-AFM in the laboratory) or optical setup in the future. Recently, the nc-AFM operation has been successfully tested and evaluated (not used in this thesis).

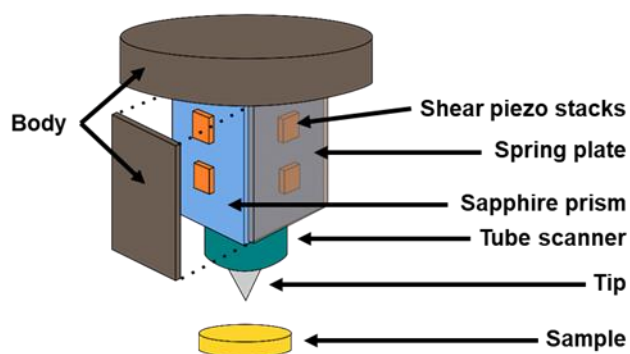
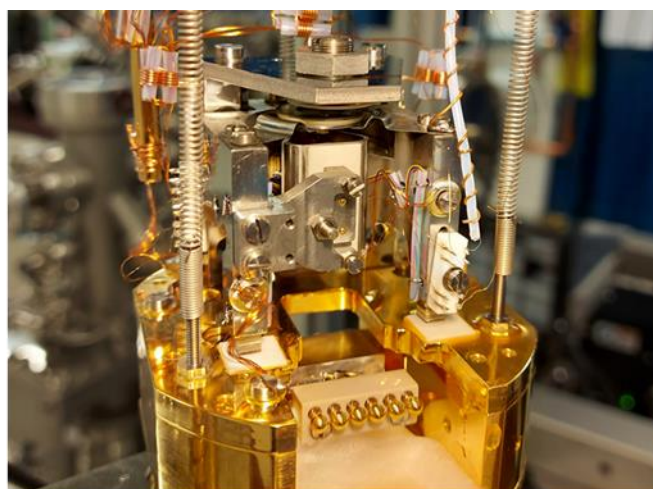


Figure 8. Pan-slider STM scanner. Upper: Photograph of the STM without housing. The Sapphire prism at the centre can be seen. Lower: Schematic drawing of the design.

3.1.6 Zener diode and temperature-dependence measurements

More than only measuring at the lowest stable temperature ($T = 5$ K), measurements at variable temperatures can be conducted by using the embedded Zener diode located in the scanner. The sample temperature can then be controlled by adjusting the applied current. Normally, a new temperature set point can be stabilized within 1 hour. The temperature is monitored within ± 0.1 K by a silicon diode. This technique makes

possible for the studies of temperature-dependence physical phenomena, for examples, thermal excitation of molecule-rotors (Chapter 7) and thermo-electric effects in the presence of Kondo correlations [62]. In principle, the Zener diode can heat up the STM to 300 K. However, since the piezo materials are specifically designed for low-temperature measurements, drift from the scanner would make the measurement at room temperature extremely challenging, especially for single-molecule experiments. On the other hand, operating at LN₂ temperature (without using LHe) is also possible in this setup.

3.2 Substrates

A single crystal Au(111) has been used as the substrate for all the experiments (Figure 9). The gold crystal, which is commercially available from MaTeck GmbH, is precisely cut along the (111)-facet. It is fixed on a heating oven and clamped with a star-shaped molybdenum sheet. By connecting two copper wires to the contact plate, it is possible to apply heat to the sample (resistive heating). The temperature can be measured by a K-type thermocouple at the contact plate.

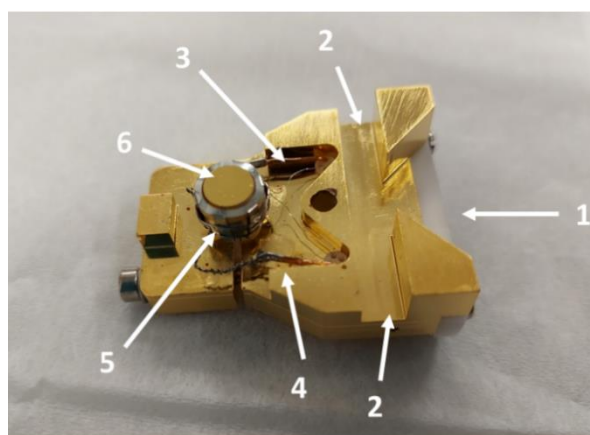


Figure 9. Photograph of a sample holder. 1: Contact plate for heater and thermocouple connections. 2: Claws for holding with the manipulator. 3: Thermocouple. 4: Connection cables for heater and thermocouple. 5: Oven. 6: Sample crystal Au(111).

In order to obtain an atomically flat Au(111) surface, standard sputtering and annealing cycles can be performed in the preparation chamber. Holding by the manipulator, the sample holder can be positioned in front of the sputter gun at 45°. By inducing Ar gas into the preparation chamber, sputtering (Ar⁺ ions; applied power at 0.5 keV) at a pressure of 4×10^{-5} mbar is done for 10 minutes in order to remove the topmost layers of the Au crystal. After that, annealing the sample for 10 minutes at 450°C heals and reconstructs the Au(111) surface. In the standard procedure, three cycles are usually done to obtain an atomic-flat Au(111) surface. After the cleaning

procedure, the sample holder is immediately cooled by LN₂ (through the manipulator) before transferring it inside the cryostat to reduce the consumption of LHe.

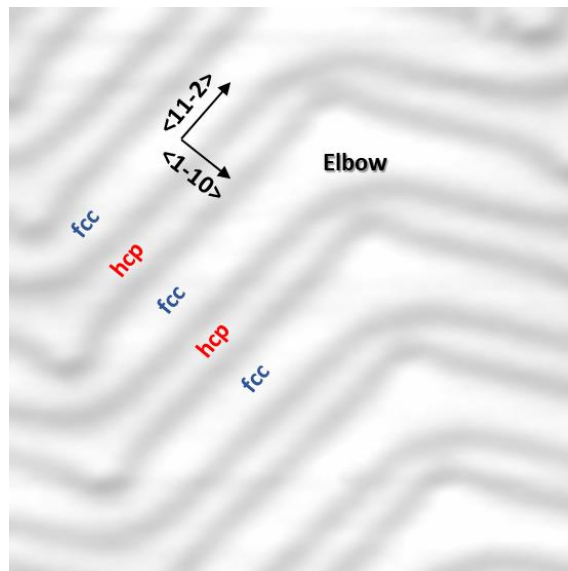


Figure 10. STM topography (30 nm × 30 nm) of Au(111). Herringbone reconstruction (periodic length ~30 nm) can be clearly observed, where the face-centered cubic (fcc) and hexagonal close packing (hcp) domains are separated by the soliton walls and the ridged structures are formed. STM image was taken under $I = 5$ pA and $V = 0.5$ V in constant current mode.

Figure 10 shows an STM image of an atomically cleaned Au(111) surface. From the nature of the Au(111), the strain release is expected because there is one additional gold atom compared to the unit cell (23 atoms instead of 22 atoms) at the topmost layer. This mechanism can be understood in a two-step process [63]: (i) The top layer densifies into a so-called $22 \times \sqrt{3}$ stripe pattern by inserting an extra Au atom into an $\langle 1-10 \rangle$ atomic chain every 22 lattice constants. This results in a 0.22 Å apparent height difference seen by the STM topography. (ii) The formation of a stripe pattern mainly releases the strain in the topmost layer along the $\langle 1-10 \rangle$ direction. Hence, a so-called herringbone reconstruction (periodic length ~30 nm) can be clearly observed, where the face-centered cubic (fcc) and hexagonal close packing (hcp) domains are separated by the soliton walls and the ridged structures are formed. The fcc-domains are wider than the hcp-domains. In addition, dislocations are formed at the elbows of the herringbone pattern during the reconstruction, where they are generally the most favorable adsorption sites for molecules.

3.3 Imaging

In the experiments, the vast majority of STM images have been obtained in the constant current mode (feedback on) with the bias voltage (V) applied to the sample with a tungsten (W) tip. Typical tunneling current set points are in the range of 3 pA

to a few hundred pA, amplified by a low-noise preamplifier by a factor of 10^9 V/A. For specific scanning purposes e.g., atomic resolution with a CO-functionalized tip, constant height mode (feedback off) has been used.

An atomic-sharp tip is desired in order to obtain useful STM images. This can be typically achieved by dipping the tip inside the metallic surface until the expected features on the surface like step edges or round protrusions (i.e., defect or additional Au adatoms) are clearly resolved.

3.4 STM image processing and data analysis

Apart from the commercial Createc STMAFM software accompanied by the STM and its electronics, image analysis is done by the SPM-specialized software Gwyddion [64]. Image processing and analysis generally include the followings: resizing, cropping, filtering (noise reduction), contrast tuning, and color mapping. Line profiles obtained from the STM topographies can also be plotted. Numerical data is processed, analyzed, and visualized by a combination of Microsoft Excel and Originlab (OriginLab Corporation, One Roundhouse Plaza, Suite 303, Northampton, MA 01060, USA.).

4 Single molecule machines on surface investigated by STM

This chapter will provide an overview and a literature review of single molecule machines on the surface, from the semi-classical motion and molecular design to a review of three main types of single molecule machines: gears, motors/rotors, and nanocars.

4.1 Overview

During the manipulation of single molecule machines by STM tip, initial and final states are identified by STM images, for examples, observing a rotation or a lateral translation event. While the observed classical motion is undoubtedly the result, the intramolecular quantum processes providing the movement are complex depending on the excitation and the molecular system.

In the next chapters, three types of single molecule machines will be discussed: gears, rotors, and nanocars. They are multi-atomic molecules that are large enough that their intramolecular collective mechanical motions become almost classical [27]. As an exemplary explanation, although gears and rotors share the same resulting classical motion, the driving modes are different in terms of the tunneling regimes and excitation modes. For driving a train of molecule-gears (Chapter 5), van der Waals interactions are the dominant forces by lateral manipulation with high tunneling resistance (e.g., $V = 10$ mV, $I = 10$ pA); for actuating the rotors and nanocars (Chapter 6 and 7), a much boarder range of tunneling parameters is implemented (e.g., $V = 50$ mV – 1500 mV, $I = 50$ pA – 1000 pA), contributing to many possible vibrational modes and electronic resonances via tunneling electrons. The ways to gain directionality are also different, where the rotation direction of gears is mostly guided by the trajectory of the STM tip, with a focus on how molecules transmit motion between others. On the other hand, the directionality of the rotors and nanocars is governed by inelastic tunneling electrons, their internal chemical components, adsorption on the surface, and the corresponding excited electronic states.

4.2 Molecular design

The motivation of this work is to investigate the underlying mechanisms of single molecule machines on the surface. The first step involves molecular designs for optimizing the functionalities on the surface; however, so far there is no general design rule for fabrication. For example, it is a big challenge to predict the adsorption geometry and the molecule-surface interaction of molecule, especially in the cases of flexible and non-planar molecules [55,65,66]. Challenges were also found for the limited gear quantity of effective transmitting rotation between molecule-gears (Chapter 5) due to their intra-and inter-molecular many degrees of freedom. A small adsorption geometry variation in the same molecule species can lead to a significant effect on their functionalities (Chapter 6). All these challenges have attracted huge interest in their prospects in nanotechnology.

4.3 Types of single molecule machines

Type	Motivation	Functionality
Gears	Design for effectively transmitting rotation between mechanically interlocked molecules	The shape defined by chemical structure (e.g., phenyl rings) acting as teeth of gears at the outer ring. Rotational axle at the center of the molecule. The directionality of rotation can be controlled
Motors/Rotors	Design for the rotating unit coupled with a perpendicular rotational axle (stator)	Directed electronic-driven rotation. Multiple quantum processes can contribute to the resulting rotation. e.g., inelastic tunneling electrons
Nanocars	Design for lateral translation across the surface or coupling with a horizontal axle	Directed electronic-driven translation. Multiple quantum processes can contribute to the resulting translation. e.g., inelastic tunneling electrons

Table 1. An overview of three types of single molecule machines on surface investigated by STM in this thesis.

Table 1 presents an overview of three different types of single molecule machines adsorbed on surfaces, investigated by STM in this work. The following will discuss the current advances and challenges individually.

4.4 Gears

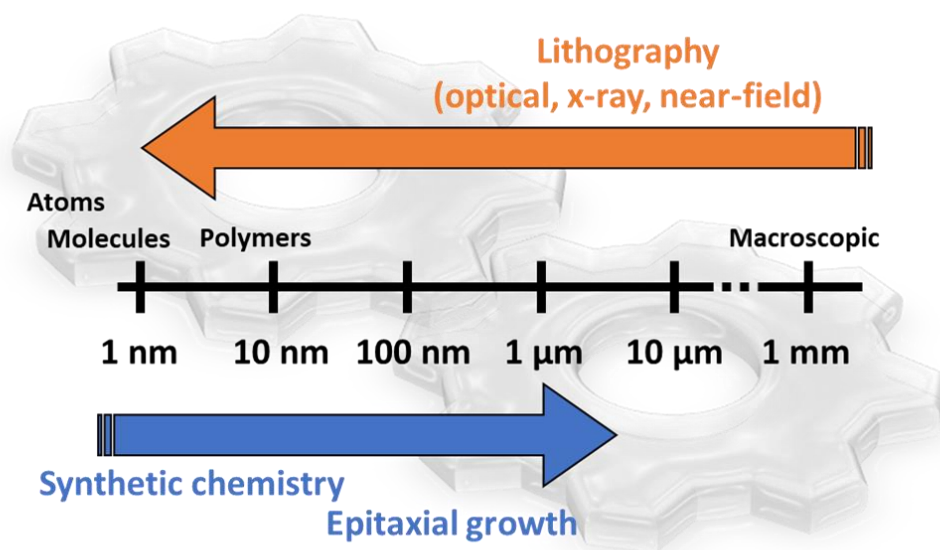


Figure 11. Brief overview of gear fabrication methods in terms of nanotechnology.

Gears with different sizes (Figure 11) can be fabricated from macro-scale (mm) to nano-scale (nm) by using bottom-up or top-down approaches [67,68]. For top-down fabrication, several kinds of lithography methods have been reported, for examples, optical lithography and focus beam lithography. Such an approach can fabricate SiO_2 solid-state gears with a diameter ranging from 30 nm to 150 nm, with the options of six-tooth or eight-tooth [69]. In this example, 15 nm-thick solid-state nanogears were fabricated by electron-beam lithography, resulting in a 30 nm outer diameter and six teeth. By employing atomic force microscopy (AFM) manipulation, mechanical experiments and rotation between interlocked gears have been presented.

On the other hand, for the bottom-up approach, i.e., finding the minimum number of atoms needed for the gearing effect, artificial chemical synthesis methods have shown promising results [70]. At the level of a single molecule, a direct observation of single PF_3 molecules chemisorbed on $\text{Ni}(111)$ on their gearing effect (hindered rotation) has been reported in 1987 [71]. In this study, the authors compared NH_3 molecules adsorbed on metallic surfaces, which could randomly rotate. The comparison results have shown that there was a weak potential barrier that hindered the rotation of PF_3 , compared to NH_3 . Such potential barrier was coverage dependence, thus indicating the interactions between molecules were the cause of such hindering effect, or gearing

effect, leading to the questions of mechanically transmitting motion between molecules.

From the work of W. Ho and colleagues in 1998, stepwise and random rotation of single O₂ molecules adsorbed on the Ni(111) surface induced by STM tip has been demonstrated [57]. Another breakthrough came in 2007, a molecular rack-and-pinion device was demonstrated by employing LT-STM, known as the first interlocked molecular gear device [72]. It was realized by using a molecule with sixfold symmetry derived from hexa-tert-butyl-pyrimidopentaphenylbenzene (HB-NBP) that formed close-packed molecular islands on Cu(111). At the border of an island, an additional molecule can generally be found, which can be laterally manipulated by the STM tip at 7 K. This molecule-gear equipped with a pyrimidine marker demonstrated that the gear rotated by the gearing effect, instead of only skidding and slipping along the edge. Two years later, the first complete and stable rotation of a molecule-gear HB-NBP mounted on an atomic axle induced by STM manipulation was demonstrated [73].

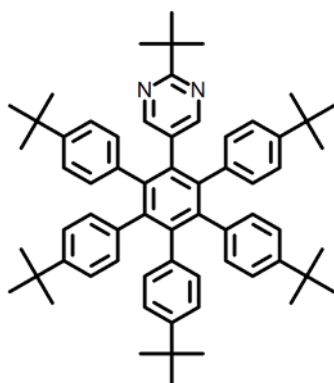


Figure 12. Chemical structure of a six-tooth molecule-gear HB-NBP [72,73].

More recent works focus on transmitting rotations between molecule-gears in a controlled manner by the STM tip. In a study [74], the transmission of motion between two HB-NBP molecules each mounted on a single Cu adatom was demonstrated, using a third HB-NBP molecule as a “molecular handle”. Furthermore, a later study on fine tuning the gear-gear distance by adjusting the underneath atomic axles has shown the importance of mechanical entanglement between the HB-NBP gears [75].

One limitation of rotating HB-NBP on metal surfaces is that they are very mobile on the surface, i.e., not stable for STM imaging due to weak adsorption [73]. Constructing interlocked, or trains of molecule-gears by mounting them on atomic axles such as defects and metal adatoms can indeed achieve stable rotation. However, these are technically complex procedures when doing STM experiments: additionally depositing adatom on the surface, then positioning the adatoms one-by-one, and mounting the single gears on top. Alternative anchoring strategies for stable rotation are

consequently required to build more demanding gearing systems. Chapter 5 will present a five-tooth star-shaped molecule-gears, and their corresponding anchoring strategies, markers design, and transmission of stable rotation.

4.5 Motors/Rotors

A molecule motor/rotor consists of two parts that can rotate with respect to each other [76]. For a rotor adsorbed on a surface, the simplest design consists of a rotating unit as the rotor is connected to an atomic axle and anchored to the surface as the stator (Figure 13). The most important aspect of a molecule-motor/rotor is to produce work, hence, unidirectionality is required as a current focus of the field (more will be discussed in Chapter 7).

The investigation of single molecule mechanics (e.g., rotation and translation) started in the 1990s. The first known discussion of single molecule rotation was at the Loch Lomond NATO workshop “Nano-Age mechanics” in 1995 (in a special session where the researchers could discuss possible topics freely) organized by H. Rohrer (the co-inventor of STM), according to a personal interview with C. Joachim (who participated in the workshop).

Soon enough, in 1998, there were two first demonstrations of single molecule rotation on surfaces. W. Ho and co-workers studied the non-directional stepwise rotation of a single oxygen (O_2) molecule physisorbed on the Pt(111) surface by STM voltage pulses at 8 K [57]. They analyzed and presented the threshold applied voltage bias needed for the rotation, explained by the vibrational relaxation rate of the molecule. On the other hand, J. K. Gimzewski, C. Joachim, and co-workers investigated the thermally induced rotation (room temperature) of a single hexa-tert-butyl decacyclene (HC-DC) molecule on Cu(111) [77]. The continuous random rotation of the single molecule was observed within a void (a molecular “vacancy”) in a monolayer of HC-DC. The rotational barrier was confirmed by the computed potential energy profile. Although the above two examples did not show unidirectional rotation, they shed light on the possibility and the desire for precise control of the rotation of single molecules on a surface.

Later, a single molecule-rotor rotating in one direction by STM manipulation was first presented in 2011, where the directed rotation of a single butyl methyl sulfide (BuSMe) molecule can be actuated under the excitation of the tunneling current in the STM junction. Another finding of the BuSMe rotor was that the directionality (> 0.95) is related to the symmetry breaking contributed by the molecule and/or STM tip [78].

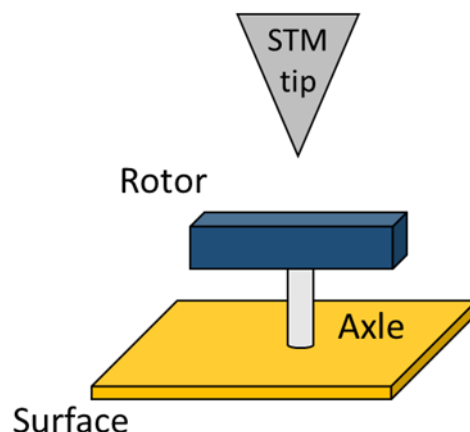


Figure 13. Schematic drawing of a molecule-rotor adsorbed on a surface in an STM junction. The rotation is induced by the STM tip manipulation.

Nonetheless, the fundamental driving mechanism in the STM junction is still far behind the complete understanding, where experiments are limited by the fact that the parameters/contributions are mixed together. For example, electrostatics interactions cannot be easily treated individually concerning inelastic tunneling excitation in STM experiments because both applied voltage and tunneling current are required to achieve tunneling effect. Possible contributions are listed below and will be discussed in detail in Chapter 7: Electrostatics interactions, elastic and inelastic tunneling electrons, electronic excited state(s), symmetry breaking by chirality, and short-range forces (e.g., van der Waals (vdW) forces), etc.

As a parallel direction, the designs of molecular motors/rotors often take macroscopic devices as inspiration. To decouple the rotary unit from the surface, a complex single stator-motor system was reported in 2013 [8], known as the “double-decker” design. The complex motor is composed of a tripodal stator at the bottom, a star-shaped rotor unit on top, and a ruthenium atomic ball bearing connecting these two components. Rotational direction can be controlled. This will be discussed in Chapter 5.

4.6 Molecule-vehicles (Nanocars)

A molecule-vehicle is a single molecule with a few nanometers having a chassis chemically bonded to molecular wheels, similar to macroscopic vehicles. The molecular wheels are envisioned to exhibit rotation on the surface with the rotational axis parallel to the surface depending on the intramolecular degrees of freedom between the atoms and chemical bonds.

The first discussion about the size limit of an automobile down to a single molecule was part of the discussion at the Loch Lomond NATO workshop “Nano-Age mechanics”

in 1995. The design, synthesis, and driving efforts of building molecule-vehicles started in the early 1990s [48,79]. The first design and the complete synthesis of a molecule-vehicle, a molecule-wheelbarrow, was done by C. Joachim and G. Repenne in 2002 [80,81]. The idea of introducing “wheels” came from a discussion between C. Joachim and G. Repenne when a colleague of theirs stopped by the meeting room [49]. The wheelbarrow molecule is equipped with two wheels (instead of legs), developed from an earlier prototype “Lander” molecule family [82]. The “Lander” was developed earlier; however, the molecule was designed for investigating the electronic properties, not the mechanics. Moreover, due to the deposition process (sublimation), only a few molecules could survive, molecular fragments were found instead on the surface. And now the first question was: can the wheels “roll” on the surface? Such rolling, totally different from the macroscopic wheels, involves large conformational changes and complex adsorption geometries of a given molecule on surfaces.

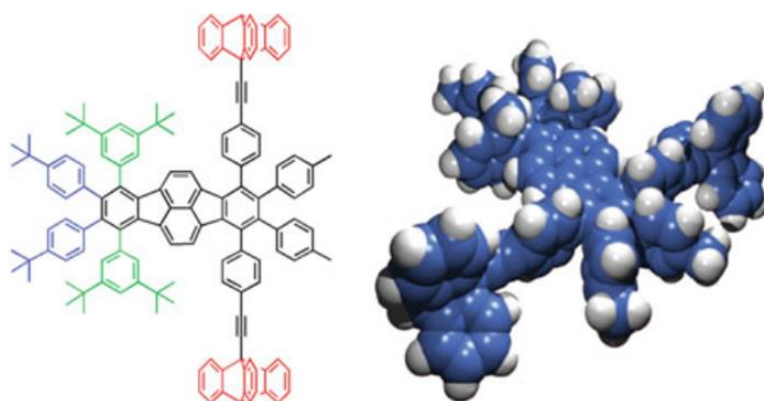


Figure 14. The first molecule-vehicle: a molecule-wheelbarrow. Reproduced with permission from Springer Nature of ref. [83].

In order to drive a molecule-vehicle with a complex structure in a controllable way, the early attempts were to use the pushing mode (lateral manipulation) of the STM tip since for large molecules, the molecule-surface interaction is usually strong. For the case of the wheelbarrow, unfortunately no experimental evidence could prove the wheels rolling on the surface due to the strong electronic interactions between the π -system of the wheels and the Cu(100) surface. No STM manipulation in moderate parameters can generate lateral motion. This result, however, has shed light on the importance of chemical structures on the molecule-surface interactions.

Later, the first direct observation of the rolling mechanism on the surface [84,85] showed that by using the tip (Figure 15), a single molecular wheel “taken” from the two wheels of the molecule wheelbarrow can be rolled on Cu(110). In this series of studies, it gave the first evidence that the molecule moved across the surface due to the rolling motion of the “wheels” by recording the signal of tunneling current.

Nonetheless, the rolling was not fully controllable possibly due to the Cu(100) crystal orientations and strong molecule-surface interactions. Later on, the first “motorized” nanocar was designed and synthesized by B. L. Feringa and co-workers in 2011 [55], which consists of four Feringa-type motors as wheels and a chassis. Propelled motions of individual Feringa-motor unit as the wheels on the surface allowing the lateral movement was observed by STM voltage pulses (i.e., without pushing by the tip). Another contribution was made by J. M. Tour, their nanocars (the term “nanocar” was coined by J. M. Tour) were built around a semi-rigid chassis with different varieties of wheels, such as C₆₀ and p-carborane [50].

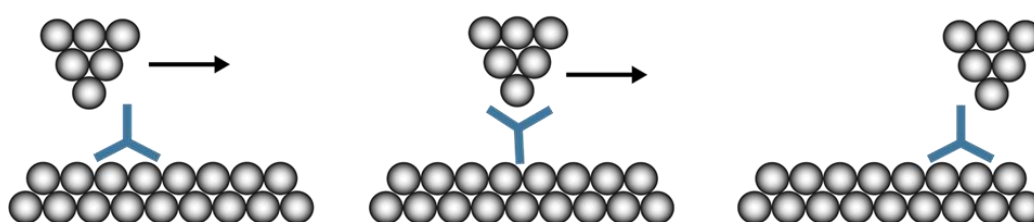


Figure 15. Side view of rolling a wheel molecule on the surface [84].

Indeed, further studies found that having a mobile nanocar translating across the surface in a controllable way, wheels are not the only option. Instead, in some cases, single molecules presenting an asymmetric structure or a strong charge separation on the metal surface can be driven by STM manipulation (inelastic tunneling electrons and/or electric field) [47,86].

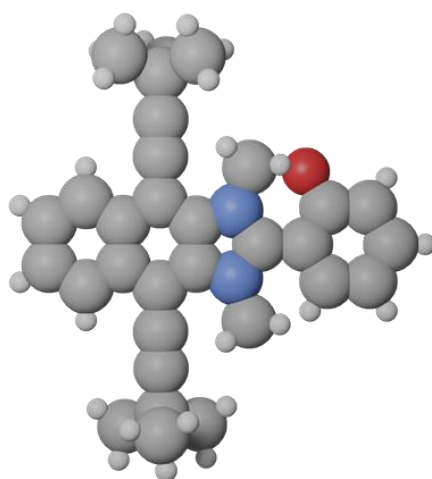


Figure 16. The GAZE molecule for the second international Nanocar Race.

In the first (2017) [48] and second (2022) [87] international Nanocar Race organized by C. Joachim (I was the co-pilot of the team GAZE, Dresden), 14 (6 in the first race and 8 in the second one) different groups of investigators from different countries gathered in Toulouse. More than a race itself, the discussion and debates about the underlying mechanism under long time experiments (massive amount of data) were valuable. They were massive experiments that clearly challenge the synthetic chemistry methods, where the size requirement for the second race was more than 70 atoms for a molecule. They also reached the limit of different STM systems (racing with speed), and the ability of nanocars to be driven for a long time (the first race was 36 hours; the second was 24 hours).

5 Transmission of rotation between molecule-gears

Manipulating and coupling of molecule-gears is the prerequisite for realizing a nanoscale mechanical machine. This chapter presents the study of the transmission of motion between molecule-gears in nanoscale by STM lateral manipulation. By designing gears with 1.2 – 1.3 nm diameter in the framework of star-shaped pentaphenylcyclopentadiene (PPCP), it allows the investigation of the interlocking between the five-tooth gears, and the corresponding motion on the Au(111) surface. Parts of the text and figures are reproduced from ref. [88] and [89] with permission of American Chemical Society and Springer Nature.

5.1 PPCP as a framework for synthesizing molecule-gears

Synthesized by the group of C. Kammerer and G. Rapenne in Toulouse, France, chemical modifications within the framework of a star-shaped pentaphenylcyclopentadiene (PPCP) molecule, taking a five-tooth macroscopic gear as an analogy. PPCP incorporates a central planar five-membered ring surrounded by five aromatic groups, thus exhibiting a star-shaped geometry (Figure 19a). In order to study transmission of motion between molecules adsorbed on the surface, the following will address the anchoring strategies and markers for visualizing by STM imaging, tip-induced manipulation (tip-molecule interactions), and molecule-molecule interactions (Figure 17).

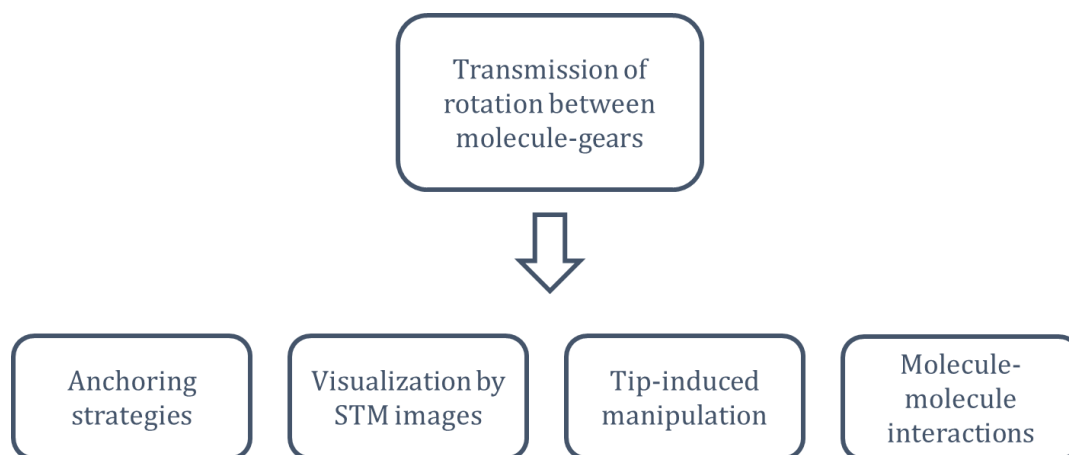


Figure 17. A scheme illustrating the design rules to achieve transmission of rotation between molecule-gears on surface.

5.1.1 Anchoring strategies

More than a choice of fabricating a five-tooth gear, the cyclopentadiene core has a unique advantage that can stabilize possible rotary motion, ideally favoring rotary motions over translations (i.e., no extra lateral movement except pure rotation at a fixed centre). It is known that the anionic character of PPCP can incorporate with a metal centre, thus forming a complex metal-organic structure [90]. From an earlier STM study [8], PPCP was bonded to a ruthenium centre while keeping the rotational degree of freedom around the metal-cyclopentadiene axis, forming a so-called “double-decker” stand-alone molecule-motor (Figure 18). In particular, an additional tripodal scorpionate ligand acted as a supporting anchoring subunit for the upper PPCP-motor subunit. Such a motor can be rotated by STM tip manipulation in a controllable way.

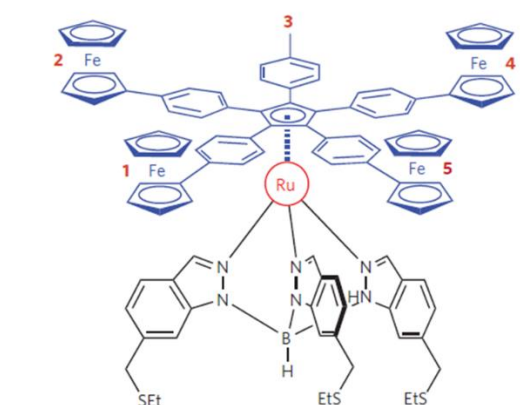


Figure 18. Structure of the double-decker molecule-motor. Reproduced from ref. [8] with permission of Springer Nature.

Here, the stable metal-organic bond is achieved by the anionic character as abovementioned. In other words, by dehydrogenation, the cyclopentadiene core becomes a radical character. Hence, if one “removes” the metal-tripodal ligand (the anchoring subunit), and “leaves” the single PPCP unit alone on a metal surface, the “direct” interaction between the molecule and surface allows a stable rotation [88]. Figure 19b shows an illustration of such an anchoring strategy. After locally applying a tip-induced voltage pulse on a pristine PPCP molecule (left), a dehydrogenated radical character is formed with the Au(111) surface (right).

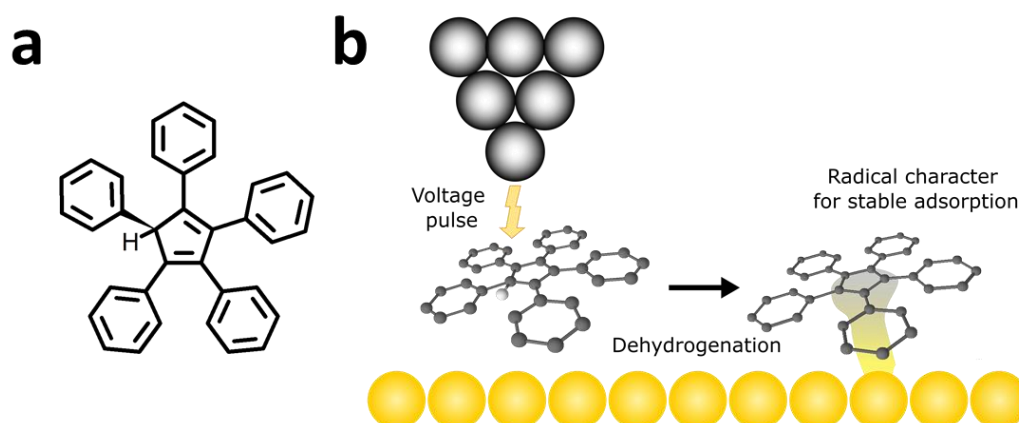


Figure 19. (a) Chemical structure of pristine star-shaped pentaphenylcyclopentadiene (PPCP). (b) Schematic image of tip-induced dehydrogenation on the Au(111) surface.

5.1.2 Markers for visualizing rotation by STM imaging

In this work [89], after depositing the PPCP molecules on the Au(111) surface, the STM topography shows a clear feature contributed by the pristine centre core as a high protrusion (Figure 20a; lower molecule). After applying a voltage pulse at 3 V, the pristine PPCP appears lower in the line profile, indicating a successful dehydrogenation event. Figure 20b shows the topographic comparison of pristine and radical PPCP, with the aid of the line profiles. Note that both pristine and radical molecules do not show the expected “star-shape” due to the flexibility of the phenyl ring. Further manipulations of the radical PPCP have demonstrated a stronger anchoring on the surface [89]. Note that not all PPCP molecules show a higher protrusion, indicating that only a small part of the molecules undergoes dehydrogenation during the thermal deposition process.

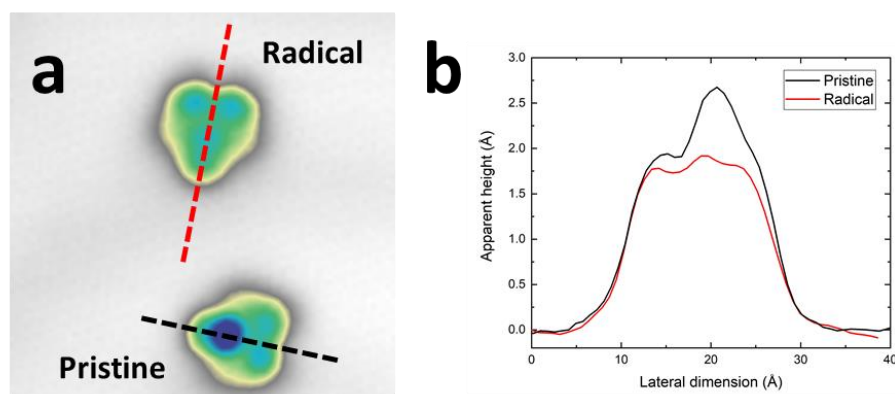


Figure 20. (a) STM image, and (b) the corresponding line profiles of the pristine and radical PPCP molecules. The radical PPCP was dehydrogenated by STM voltage pulse (not shown). The peak-to-peak apparent height difference is about 0.7 Å. (Image size: 6.3 nm × 6.3 nm; V = 500 mV; I = 20 pA)

The results of manipulating PPCP have shed light on several aspects: first, the flexible phenyl rings (teeth) lead to many possible conformations, where the expected star-shaped structure is the only stable conformation on the Au(111) surface, thus making it a challenging determination of gears coupling. Modifications on the chemical substitutions of the teeth are possible. Second, tip-induced dehydrogenation one-by-one on single gears is a complex experimental procedure. Alternative substitutions and on-surface reactions (e.g., molecules become radical already during thermal deposition) can simplify the process. Furthermore, even if the PPCP gear is completely flat and stable on the Au(111) surface, the observation of rotary motion from STM topography will be challenging due to the five-fold symmetry. Each stepwise rotation station appears the same in the topographies, making it not possible to retrieve the successful event. A “marker” is therefore needed for easy-visualization of rotation events [72].

5.1.3 Modification of PPCP designs

Therefore, design modifications were envisioned to enhance the molecule-surface interactions, favor the tip-molecule interactions, and easy-visualize the rotary motion by STM imaging. For the goal of increasing tip-molecule interactions and STM visualization, the five surrounding aromatic groups can be modified with different moieties as shown in Figure 21. Additionally, in terms of anchoring strategy, the precursor molecules (gears **3** and **4**) incorporate a Br atom on the central ring since this halogen affords a good balance between precursor stability and the ease of homolytic carbon-halogen bond cleavage. In this case, similar to the case of dehydrogenation, the homolytic cleavage of the C-Br bond leads to increased interaction of the resulting radical character with the substrate would thus provide an anchoring point similar to Figure 19b. Note that for all the chemical modifications, the products are the mixture of regioisomers [88] from the nature of five-fold symmetry from the PPCP framework; for simplicity here, only one regioisomer is shown.

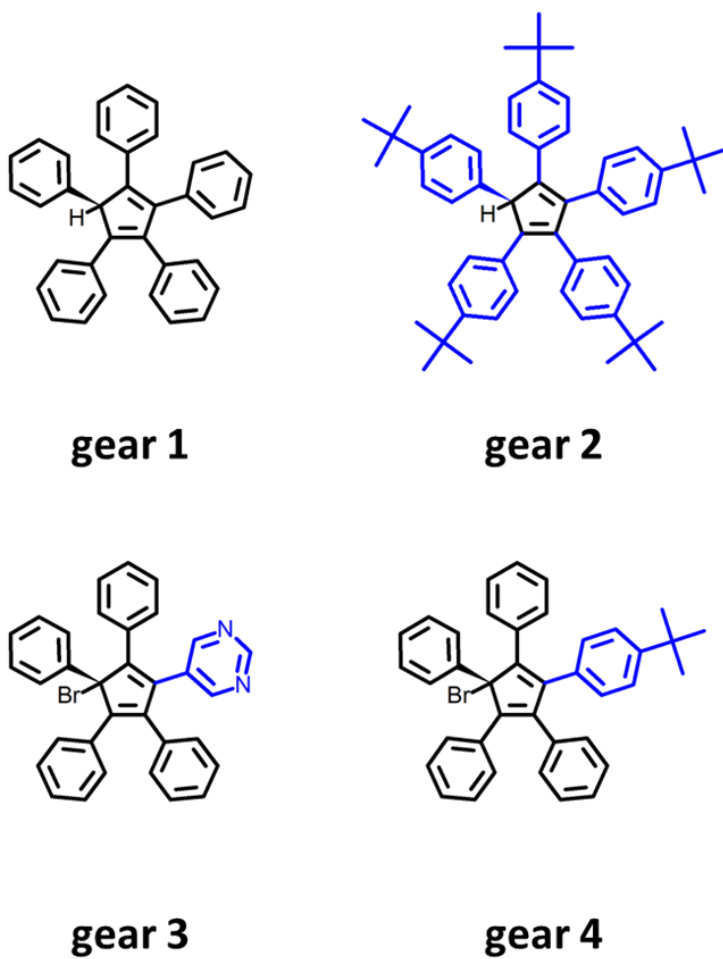


Figure 21. PPCP-derivatives. Gear 1: the original PPCP. Gear 2: All five phenyl rings are replaced by five 4-tert-Butylphenyl groups for higher stability on the surface. Gear 3: One of the phenyl rings is replaced by an aromatic pyrimidine tooth as a “chemical marker”. Gear 4: One of the phenyl rings is replaced by a 4-tert-Butylphenyl group as a “steric marker”. Note that gears 3 and 4 are brominated at the cyclopentadiene core.

5.2 Gear 2: PPCP molecule-gears with extended teeth

5.2.1 Deposition on Au(111)

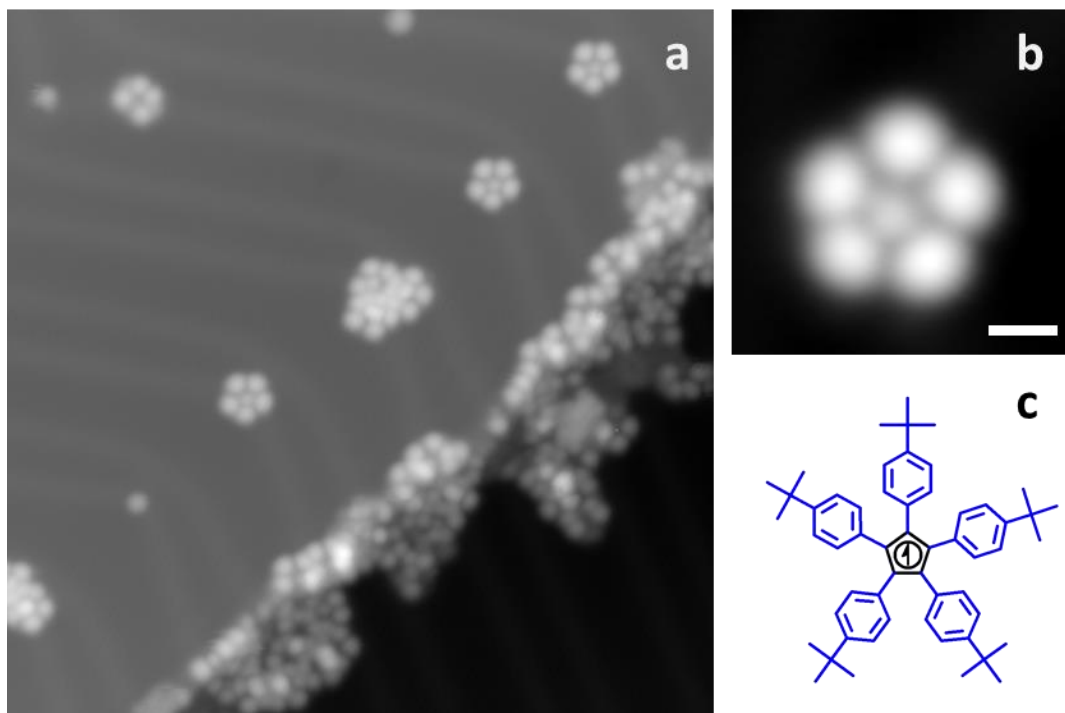


Figure 22. Overview and the structure of molecule-gear **2** on Au(111). (a) Overview STM image (40 nm × 40 nm) was taken under the conditions of $V = 500$ mV and $I = 5$ pA. (b) Close-up STM image of a single gear **2** molecule. Scale bar = 1 nm. (c) Chemical structure of gear **2**.

Gear **2** is the first modification to improve the adsorption stability on Au(111), compared to gear **1**. After deposition of gear **2** on the Au(111) surface held at room temperature (Figure 22a), the majority of the single molecules can be found adsorbing on the kink sites formed by the herringbone reconstruction; only a few small clusters can be found. A number of fragments can be found along the step edges of the Au(111) surface. According to the close-up image (Figure 22b), the star shape appearance of a single molecule has a very good agreement with the expected chemical structure (Figure 22c). Compared to the case of gear **1**, the tert-butyl groups provide stronger molecular adsorption. The adsorbed gear **2** can be rotated by STM lateral manipulation without the need for voltage pulses, suggesting that the C-H cleavage has occurred during evaporation.

5.2.2 Single molecule rotation

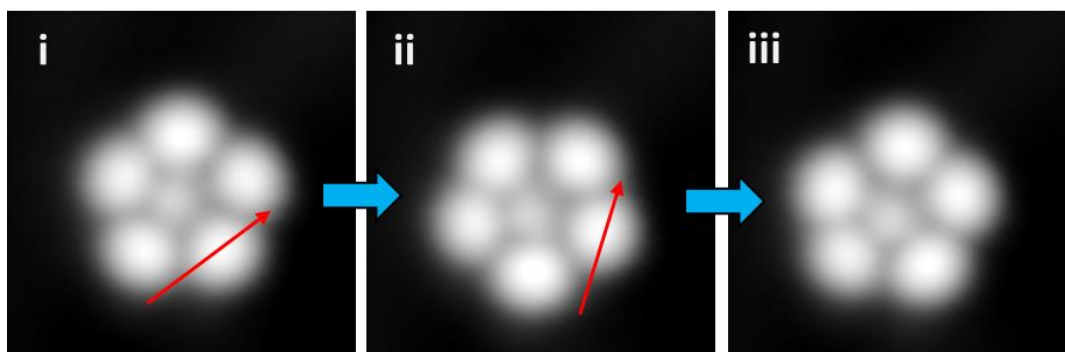


Figure 23. Motion of molecule-gear **2**. The red arrows indicate the tip manipulation trajectories ($V = 10$ mV and $I = 500$ pA). STM images ($5\text{ nm} \times 5\text{ nm}$) were taken under $V = 500$ mV and $I = 5$ pA.

Tip-induced manipulation has been carried out to investigate the motion and the anchoring strategy. More lateral manipulation details can be found in Chapter 2. All lateral manipulations were applied in constant current mode. The red arrows indicate the tip manipulation trajectories ($V = 10$ mV and $I = 500$ pA). After the first manipulation (Figure 23i), one step of rotation ($\sim 36^\circ$) has been observed in the subsequent STM image (Figure 23ii). A very similar appearance in Figure 23iii can be found after the second manipulation. The molecule rotates according to the manipulation signal. However, it is not trackable in the STM images. In addition, compared to gear **1** that at a certain adsorption geometry, STM images do not show the star-shaped molecule but triangular shapes (Figure 20a as an example), the tert-butyl groups stabilize the adsorption of the molecule on the surface by keeping the molecule always flat.

5.2.3 Repositioning of molecules by manipulation

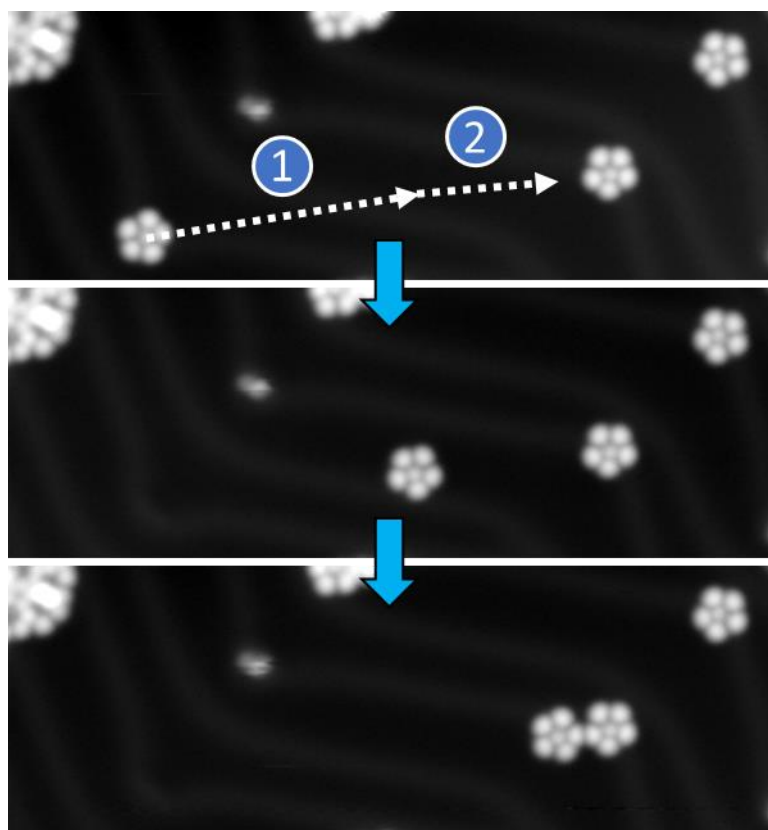


Figure 24. Precise repositioning of molecule by tip manipulation. In the sequence, a single molecule-gear **2** from the left is brought to a new adsorption position near another gear on the right. Two separated lateral manipulation steps have been employed: (1) and (2). The total displacement of the molecule is about 24 nm in this particular case. STM images (40 nm × 14 nm) were taken under $V = 500$ mV and $I = 4$ pA.

Since small molecular clusters are rare on the surface, repositioning of molecules can be achieved by stronger tip lateral manipulation. It is necessary for mounting multiple gears as a train for the study of the transmission of motion. Figure 24 shows an exemplary sequence. The molecule on the left is first brought to a new position for a displacement of around 14 nm, which is about halfway to the destination. A second manipulation is applied to bring the molecule closer to another one. In this case, the displacement is around 10 nm, and as a result, the total displacement is about 24 nm. Together with the stable single molecule rotation (Figure 23), it indicates that the gears obtain a good balance between anchoring and lateral translation during manipulation.

5.2.4 Transmission of motion

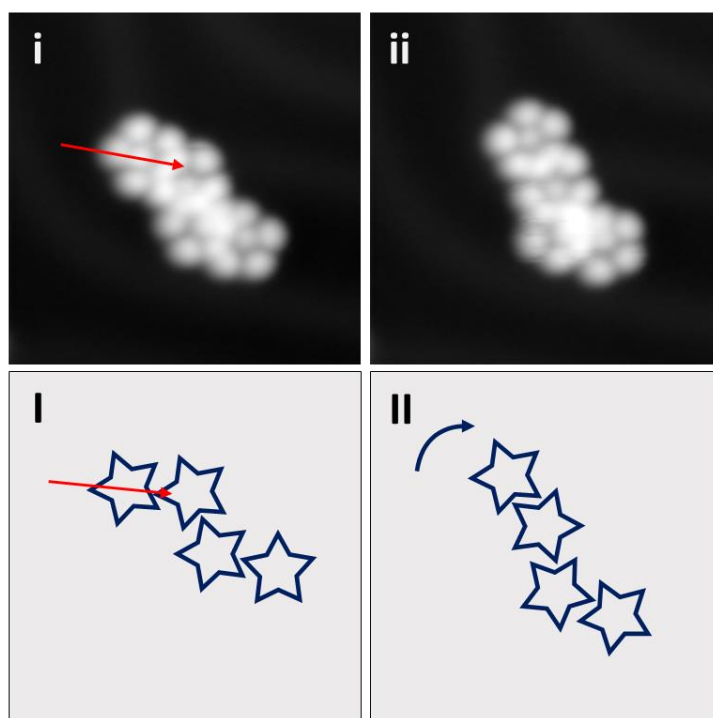


Figure 25. Train of molecule-gears **2**. (i – ii) Sequence of motion between four gears. The red arrows indicate the tip trajectories ($V = 10$ mV and $I = 2.2$ nA). (I – II) Corresponding schematic diagrams of the gear motion (not in scale). STM images ($12\text{ nm} \times 12\text{ nm}$) were taken under $V = 500$ mV and $I = 3$ pA.

By using the above method, multiple gears can be brought together from different distances manually. Figure 25 demonstrates an example of a gear train consisting of four molecules. After interlocking all four gears, it is not possible to induce any motion by manipulating the gear teeth. Interestingly, by driving the tip across the centre of the molecule, it can easily lead to lateral displacement. Such a strategy is used for rotating three or more interlocked trains. As shown in the sequence (Figure 25), lateral manipulation was applied to the topmost gear at constant current mode ($V = 10$ mV and $I = 2.2$ nA), and the red arrows indicate the tip trajectories. The subsequent image shows both a small degree of rotation and lateral displacement from all four gears.

5.3 Gear 3: PPCP molecule-gears with chemical marker

5.3.1 Deposition on Au(111)

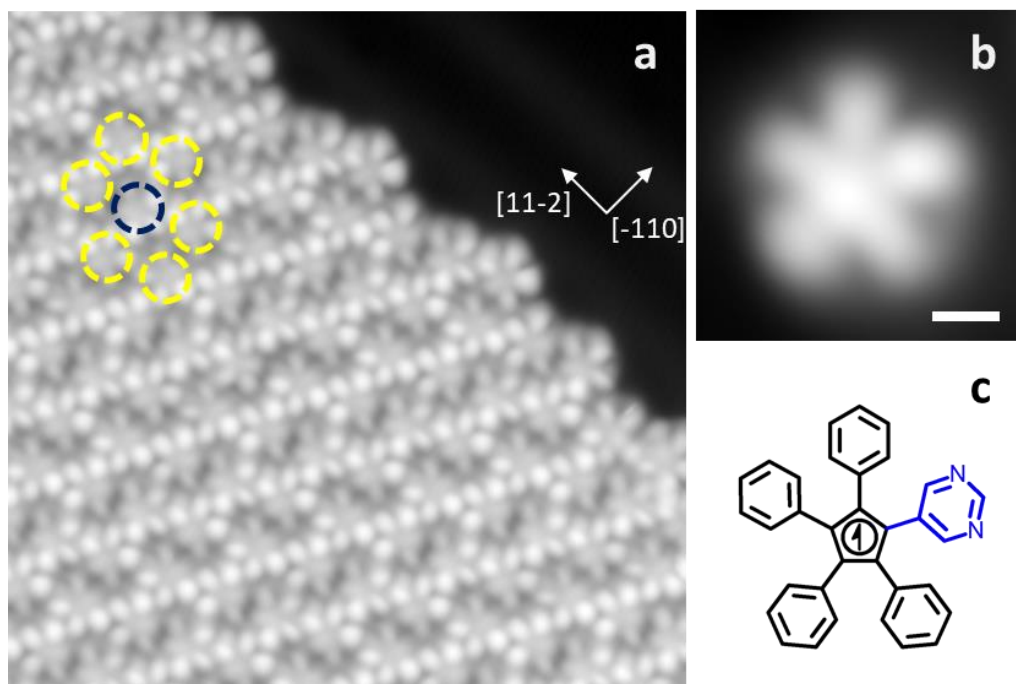


Figure 26. Overviews and the structure of gears **3** on Au(111). (a) Overview STM image ($15\text{ nm} \times 15\text{ nm}$) taken at $V = 500\text{ mV}$ and $I = 7.2\text{ pA}$. (b) STM image of a single gear **3** molecule (radical). Scale bar = 0.5 nm . (c) Chemical structure of gear **3**.

Then we investigate if a chemical marker (gear **3**) can be trackable for observing the stepwise rotation from STM images. After deposition of gear **3** on the Au(111) surface held at room temperature, close-packed molecular islands and small clusters of molecules can be found, growing from the step edges of Au(111) (Figure 26a). The molecules interlock with each other and form zig-zag lines. The close-packed molecules orient in a C_2 symmetry, where two molecules occupy the same unit cell. The nearest-neighbor distance is $1.21\text{ nm} \pm 0.01\text{ nm}$. After isolating a single molecule, a star-shaped appearance from the topography in Figure 26b can be clearly identified, corresponding to the expected chemical structure in Figure 26c. Note that the black arrow at the core represents the radical character of the molecule.

For the chemical marker, gear **3** does not show the expected contrast difference equipped with a pyrimidine moiety in this case (Figure 26b). In the previous studies, pyrimidine moieties have been observed from the studies of HB-NBP [72], where at a certain applied voltage bias of imaging ($> 2.2\text{ V}$ on a Cu(111) surface) one can observe a different topographic contrast of this group, compared to the other four teeth. Hence,

it was possible to trace the stepwise rotary motion from the STM topographies in that case. However, a different behavior has been found for the same HB-NBP adsorbed on a Pb(111) surface [74], where no contrast difference can be found. The same absence of such electronic marker effect suggests that the pyrimidine moiety adopts a conformation that reduces its electronic interactions with the surface.

5.3.2 Anchoring strategy: Debromination by pulse

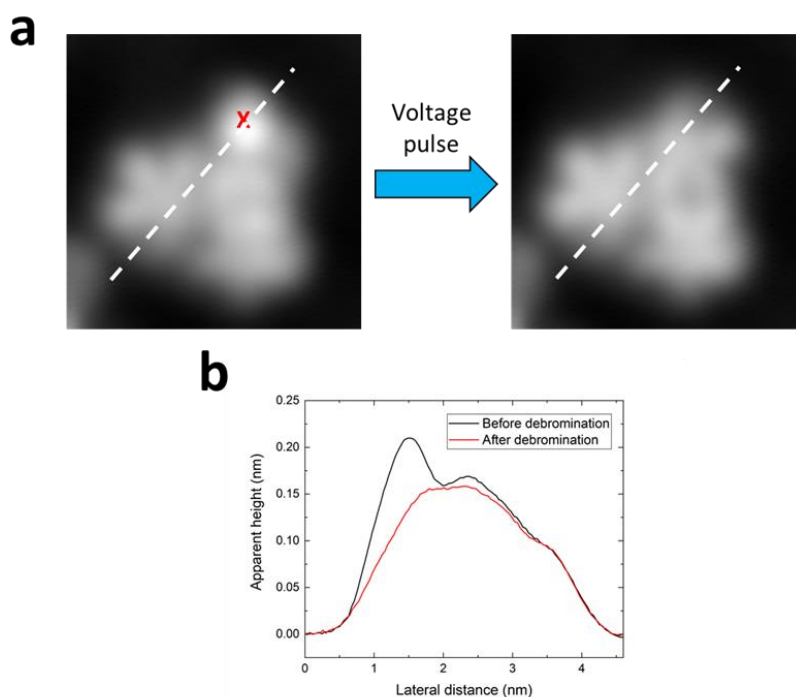


Figure 27. Tip-induced debromination on a gear **3** molecule. (a) A 3.0 V voltage pulse is locally applied. Position is shown as red mark. The lobe with higher apparent height is flattened in the subsequent image, indicating a successful debromination. (b) Comparison of line profiles before and after debromination, respectively. STM images (4.5 nm \times 4.5 nm) were taken under $V = 500$ mV and $I = 3.0$ pA.

Another key feature of gear **3** is the signature of the C-Br moiety at the core. While the vast majority of the molecules (Figure 27a) do not show a higher apparent height similar to the case of gear **1**, a small number of molecules however show a higher lobe as shown in Figure 20a. By applying a voltage pulse ($V = 3$ V), one can flatten such a high lobe, as a result, the molecule appears the same as the lower two molecules (flattened; Figure 27b). This indicates that the homolytic cleavage of C-Br bond has occurred upon the thermal deposition process ($T = 185^\circ\text{C}$) on the Au(111) surface held at room temperature [91]. In other words, compared to the original design C-H bond, where additional voltage pulses are usually required to flatten the PPCP molecules, the early cleavage of C-Br bond facilitates the overall experimental procedure.

5.3.3 Single molecule rotation

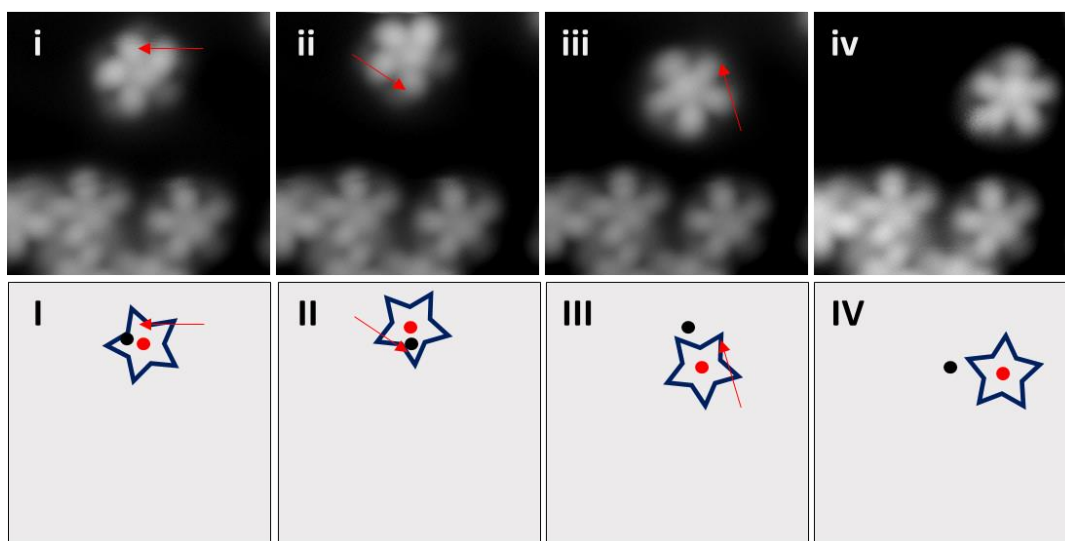


Figure 28. Non-concentric rotation of a single molecule-gear **3**. Red arrows indicate the trajectories of lateral manipulations ($V = 10$ mV, $I = 8$ pA; tunneling resistance = 1.25 G Ω) achieved by the STM tip. (i – iv) The manipulations induced both rotations and small lateral shifts. (I – IV) Corresponding schematic diagrams of the gear rotations (not in scale). Black and red dots indicate the lateral displacements before and after manipulations, respectively. All STM images (5 nm \times 5 nm) were taken under the conditions of $V = 500$ mV and $I = 7.2$ pA.

Figure 28 shows a sequence of motion when manipulating gear **3**. STM records images before and after each manipulation in all of the following sequences. All of the steps show successful movements induced by the STM tip. However, the motion shows small lateral shifts with some degree of rotation, indicating a non-concentric or unstable rotation. Moreover, the directional control by the tip is not optimized since the gears are “pulled” by the tip, i.e., in the opposite direction of the tip trajectory.

5.3.4 Transmission of motion between molecule-gears

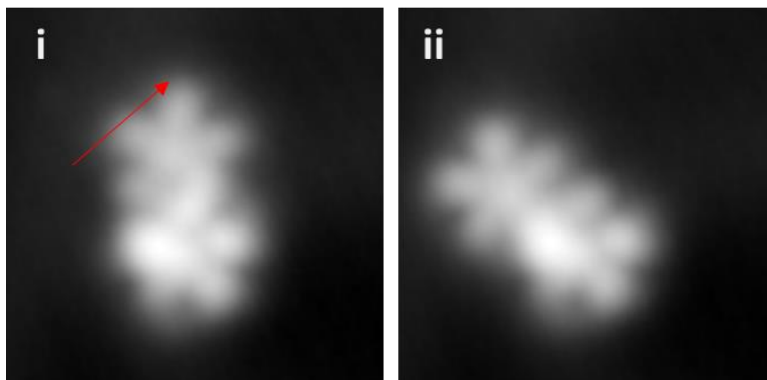


Figure 29. Handle behaviour between two molecule-gears 3. (i – ii) Lateral manipulation ($V = 30$ mV and $I = 8$ pA; Tunneling resistance = 3.75 G Ω) on the driver gear (red arrow for trajectory) generates a handle-like behavior of rotation in an opposite direction. All STM images (5 nm \times 5 nm) were taken under the conditions of $V = 500$ mV and $I = 3$ pA.

Further attempts on transmitting rotation of two interlocked gears show a “handle-like” behaviour, similar to ref. [74]. In Figure 29i, when driving the upper gear as a “driver gear”, it shows a lateral displacement in counter-clockwise (CCW) in the subsequent image Figure 29ii, in which the driver has been pulled by the STM tip. The lower gear, “follower gear”, rotates CCW together with the driver without lateral displacement.

5.4 Gear 4: transmitting motion between three PPCP gears

5.4.1 Deposition on Au(111)

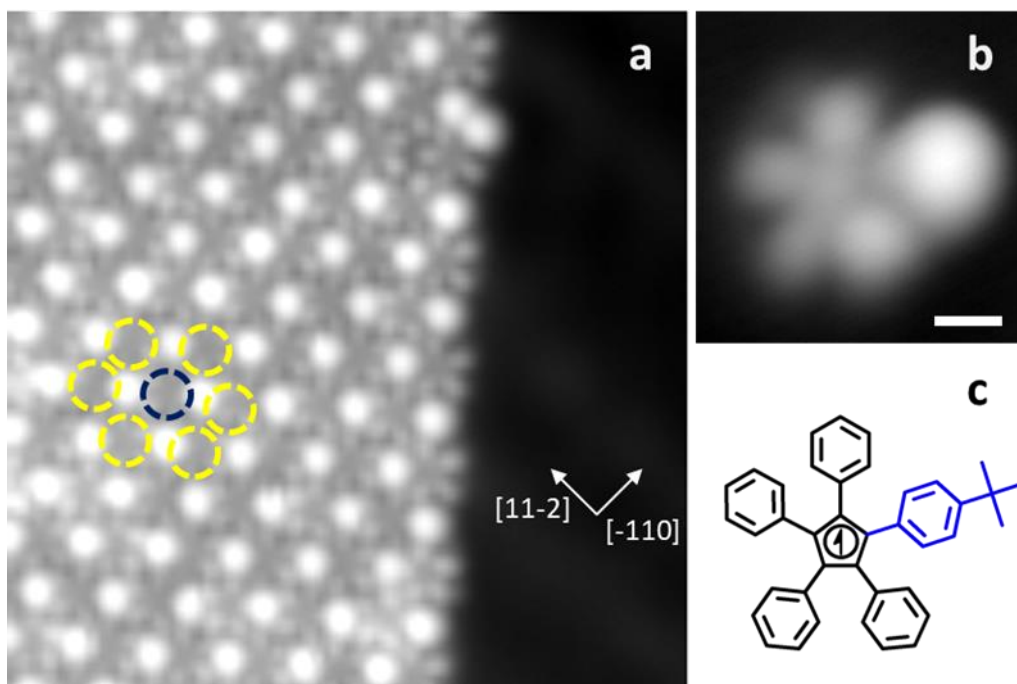


Figure 30. Overviews and the structure of molecule-gears **4** on Au(111). (a) Overview STM image ($15\text{ nm} \times 15\text{ nm}$) was taken under the conditions of $V = 500\text{ mV}$ and $I = 7.2\text{ pA}$. (b) STM image of a single gear **4** molecule. Scale bar = 0.5 nm . (c) Chemical structure of a gear **4** molecule.

Given the results from gear **2** and **3**, the tert-butyl group is both visible from STM images and provides additional adsorption stability, gear **4** with a tert-butyl group attached to one of the teeth being investigated. After deposition of gear **4** on the Au(111) surface held at room temperature, close-packed molecular islands and small clusters of molecules can be found, growing from the step edges of Au(111) (Figure 30a), similar to the case of gear **3**. The close-packed molecules orient in a C_2 symmetry, where two molecules occupy the same unit cell. The nearest-neighbor distance is $1.36\text{ nm} \pm 0.02\text{ nm}$ due to the larger tert-butyl group as the tooth.

The brighter lobe can be easily assigned to the tert-butyl group after isolating a single gear **4** from the island (Figure 30b – c). This confirms that the tert-butyl group can act as a steric marker due to its distinguishable apparent height of about 0.22 nm , which is relatively higher than the planar phenyl ring at about 0.17 nm on the Au(111) surface. Compared to the case of HB-NBP which requires $V > 2.2\text{ V}$ for the visualization of the chemical marker [72], this can have a lower possibility to induce unintended motion during scanning. The molecule the tert-butyl group can be visualized at low

bias ($V = 0.5$ V) in this case, where it is not a disturbing scanning parameter. In addition, the molecule shows a flat centre, indicating that same as the case of gear 3, the cleavage of C-Br bond occurs during the deposition procedure.

5.4.2 Single molecule rotation

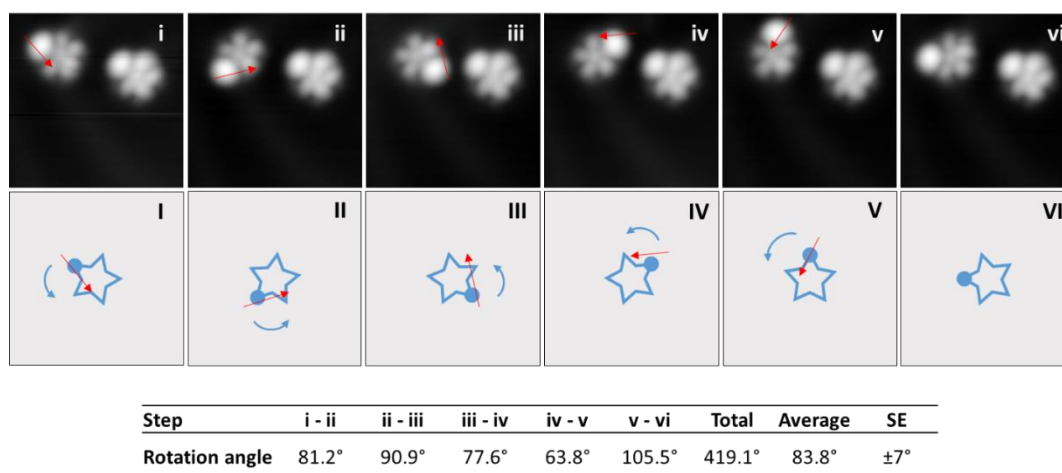


Figure 31. Rotation of a single molecule-gear 4. Red arrows indicate the trajectories of lateral manipulations ($V = 10$ mV and $I = 8$ pA; tunneling resistance = 1.25 G Ω) achieved by the STM tip. (i - vi) Rotational sequence of a single molecule-gear 4. The molecule on the right acts as a reference. (I - VI) Corresponding schematic diagrams of the gear rotations (not in scale). All STM images (6.5 nm \times 6.5 nm) were taken under the conditions of $V = 530$ mV and $I = 13$ pA.

Apart from isolating the molecules one by one with the tip manipulation, a gentle STM tip crashing near the island can efficiently extract a larger number of molecules. Small groups of two to four molecules can be found. Figure 31 shows a stepwise sequence of full rotation (by five manipulation steps) achieved by gear 4. All lateral manipulations (red arrows) were applied in constant-current mode ($V = 10$ mV and $I = 8$ pA). The STM tip drives the driver gear by interacting with the tert-butyl tooth in order to generate a CCW rotation. The rotational angles are on average 84° , and a maximum total rotation of 419° from this sequence is rotated. The rotation is stable and concentric (i.e., fixed at one point), indicating that the interactions between the cyclopentadienyl radical and the gold surface strongly anchor the gear at the pinning position.

5.4.3 Two interlocked molecule-gears

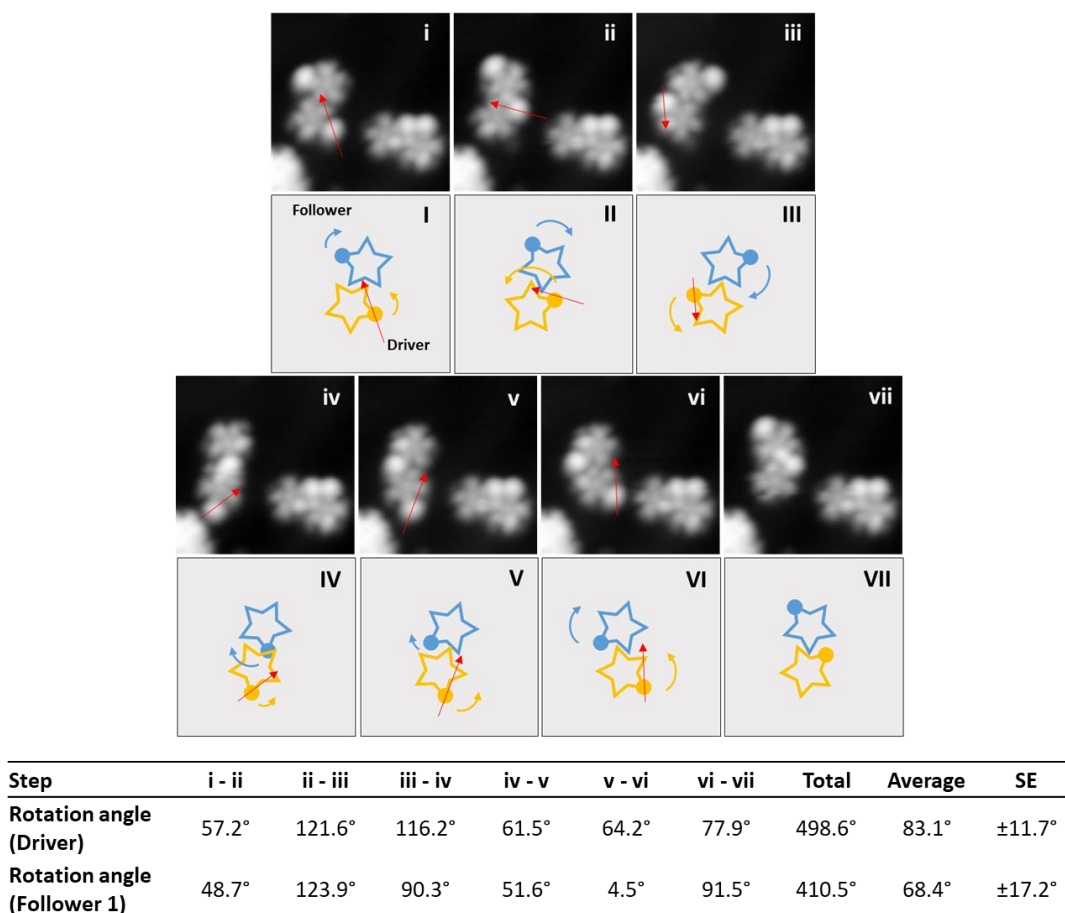


Figure 32. Stepwise collective rotational sequence between two interlocked molecule-gears **4**. Red arrows indicate the trajectories of lateral manipulations ($V = 10$ mV and $I = 14$ pA; tunneling resistance = 0.71 G Ω) achieved by the STM tip. (i – vii) The rotations between two gear **4** molecules. The other two molecules on the right act as a reference and their motion sequence. (I – VII) Corresponding schematic diagrams of the gear rotations (not in scale). All STM images (6.5 nm \times 6.5 nm) were taken under the conditions of $V = 530$ mV and $I = 13$ pA.

Given the stable rotation of a single molecule, now it is interesting to investigate the transmission of rotation. In Figure 32, a sequence of stepwise and complete rotations of two interlocked gears **4** is demonstrated. A sequence of six lateral manipulations ($V = 10$ mV and $I = 14$ pA) is performed. The STM tip drives the driver gear by interacting with the tert-butyl tooth in order to generate a CCW rotation. Simultaneously, such CCW rotation mechanically transmits to the follower gear. As a result, the follower gear rotates clockwise (CW). In this particular sequence, each rotational angle is on average 83° for the driver and 68° for the follower, in total 499° for the driver and 410° for the follower. Interestingly, larger rotational angles between steps ii and iii (122°) and steps iii and iv (116°) are observed, while the tert-butyl teeth of the gear directly

interact with and pass the phenyl rings, possibly because of the larger molecular interactions and/or the larger size of the tert-butyl group. A slight lateral shift of the driver (around 0.4 nm) is observed between steps v and vi, only leading to a small rotational angle on the follower (5°). This also indicates that the gear-gear distance is critical for transmitting rotation between molecule-gears with many degrees of freedom [92,93]. In other words, the collective rotational degrees of freedom of the follower are in competition with many other possible intramolecular mechanical modes.

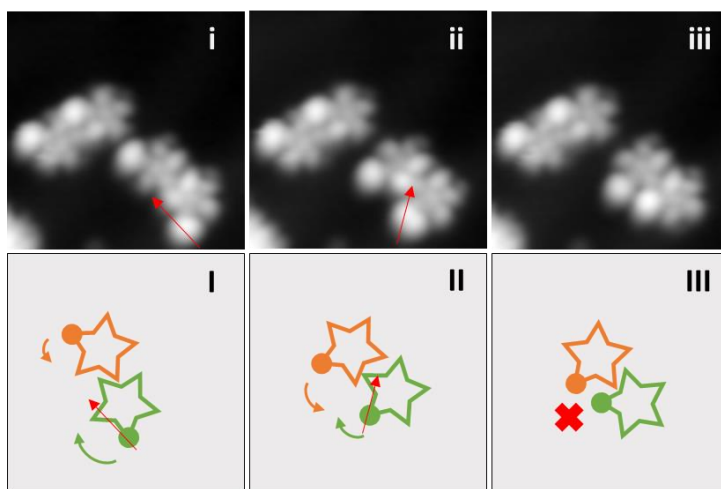


Figure 33. Rotation blocked by the tert-butyl groups between two interlocked gears **4**. Red arrows indicate the trajectories of lateral manipulations ($V = 10$ mV and $I = 14$ pA; Tunneling resistance = 0.71 G Ω) achieved by the STM tip. (i – ii) Manipulation of the driver leads to effective transmission of rotation. (ii – iii) The two tert-butyl teeth cannot pass each other. No further manipulations in this direction. (I – III) Corresponding schematic diagrams of the gear rotations (not in scale). All STM images (6.5 nm \times 6.5 nm) were taken under the conditions of $V = 530$ mV and $I = 13$ pA.

As observed in Figure 32ii – iii and iii – iv, the tert-butyl group has a different behavior (i.e., larger rotational angle) when interacting with the bare phenyl rings of the neighbour. We deduce that when the larger tert-butyl groups from both gears interact, both gears may stop rotating. Indeed, a sequence of rotation (Figure 33) shows an interesting behaviour when the two individual tert-butyl teeth interact by lateral manipulation ($V = 10$ mV and $I = 14$ pA). In Figure 33i – ii, the STM tip drives the driver by interacting with the tert-butyl tooth in order to generate CCW rotation, and simultaneously the follower rotates CW. In step iii, no further rotation to the same direction can be achieved when the two tert-butyl teeth interact with and cannot with each other.

5.4.4 Three interlocked molecule-gears

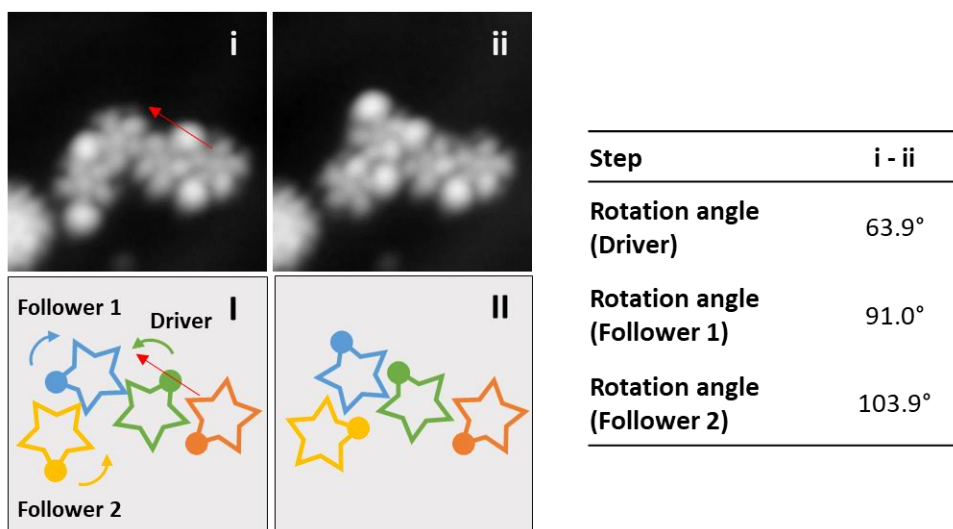


Figure 34. Stepwise collective rotational sequence between three single molecule-gears 4. Red arrows indicate the trajectories of lateral manipulation ($V = 10$ mV and $I = 14$ pA; tunneling resistance = 0.71 G Ω) achieved by the STM tip. (i – ii) STM tip manipulation at the third gear as a driver induces a three-in-a-train collective rotation. The gear on the right side does not interlock with the driver, therefore no rotation can be observed. (I – II) Corresponding schematic diagrams of the gear rotations (not in scale). All STM images (6.5 nm \times 6.5 nm) were taken under the conditions of $V = 530$ mV and $I = 1.9$ pA.

A collective rotation among three molecule-gears is demonstrated in Figure 34. It is however a rare case, also known as the first example of transmitting rotation between three molecules [88]. While manipulating (red arrow) the tert-butyl tooth of the third gear as a driver, a step in the transmission of rotation among three interlocked gears was induced. The train of gears is in a zigzag alignment.

At first, a CCW rotation (64°) is initiated by the driver, while simultaneously, follower 1 rotates CW (91°) and then follower 2 rotates CCW (104°). Before manipulation, the gear-to-gear distance between driver and follower 1 is 1.20 nm, and 1.26 nm between the two followers. After a rotational step (Figure 34ii), slight lateral displacements for all three gears have been observed: the driver-follower 1 distance becomes 1.30 nm and the two followers' distance is 1.38 nm. Note that the gear on the right side (brown) did not interlock with the driver at a sufficient distance, thus no rotation was observed. No further rotation after this sequence was observed within the same train of molecules possibly due to the strong interactions of interlocked tert-butyl groups between gears.

A comparison of the motions can be made between gears 3 and 4. On the basis of the results, only gear 4 shows transmission of rotation up to three interlocked gears. Given that the tunneling parameters are very similar (tunneling resistance = 0.71 – 1.25 G Ω)

for both gears, the driving potential energy increases are nearly the same in all rotations. In addition, assuming that the interactions between the bare phenyl rings from both gears **3** and **4** are the same, this suggests that during manipulation the presence of the tert-butyl group of gear **4** provides a more favourable tip-gear interaction than the planar phenyl ring of gear **3** [50].

On the other hand, the increase in potential energy induced by the tip manipulation allows the train of three gears to find a minimum-energy path on the corresponding ground-state potential energy surface (PES) and thus makes possible the transmission of rotation along the train. The end of the scenario indicates that after following this minimal-energy path, a deep minimum-energy well exists on the PES of the three molecules interacting with each other, which stabilizes the final conformation imaged in Figure 34ii.

Following this argument, for more than three molecule-gears in a train, no successful transmission of rotation can be induced. A possible reason is that the tip-induced potential energy increase in the driver is not able to excite the rotational degrees of freedom of the followers, but is directed toward others' degrees of freedom on the PES. Another possible reason is that the molecule-gears are too "soft" (i.e., many degrees of freedom) for interlocked rotation [92].

5.5 Summary and outlook

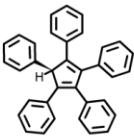
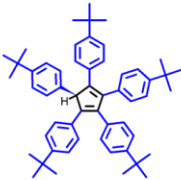
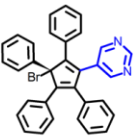
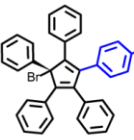
Molecule-gears on Au(111)	 gear 1	 gear 2	 gear 3	 gear 4
Dehydrogenation /debromination	By voltage pulse + partially occur upon deposition	By voltage pulse + partially occur upon deposition	By voltage pulse + partially occur upon deposition	Occur upon deposition
Anchoring (single gear)	Yes	Yes	No	Yes
Rotation/mobility (single gear)	Yes	Not trackable	Rotation with lateral shift	Yes
Transmission of rotation	Handle-like behaviour	Not trackable	Handle-like behaviour	Full rotation between 2; Up to 3 gears (1 step)

Table 2. Comparison of PPCP derivatives: motion behaviour and gearing effect.

In this Chapter, the molecular adsorption, tip-induced manipulation, and gearing effect from more than two interlocked PPCP derivatives on the Au(111) surface are presented. Table 2 summarizes the key findings:

- (1) **The anchoring strategy** has been activated by the C-H or C-Br cleavage at the cyclopentadiene core, and consequently achieved by the radical character. Both dehydrogenation and debromination can be induced by STM voltage pulse. On the other hand, for all PPCP derivatives, the reaction undergoes during the thermal deposition process, reducing the experimental complexity when constructing trains of gears. Compared to a very strong anchoring with a chemisorbed molecule, the radical character provides a weaker anchoring, but with sufficient flexibility to reposition the gears by lateral manipulation.
- (2) **Tip-induced lateral manipulation** acts as a tool for investigating the stability of the rotation, directly related to the anchoring strategy (i.e., the evaluation of the “strength” of the atomic axes). This allows the evaluation of the concentric rotation of a molecule-gear.

- (3) **Mechanically transmitting motion** between gears is possible for all the PPCP derivatives from this work. However, handle-like behaviors have been observed when the gears (e.g. gears **1** and **3**) have relatively weak interactions with the Au(111) surface. From the case of gear **4**, the promising transmission of rotation between two molecules suggests that the tert-butyl groups as the steric marker further stabilize the rotary motion. This marker also facilitates the tip-molecule interactions for manipulation, compared with gear **3**.

Realization of mechanical molecular devices such as a molecular Pascaline calculator requires the novel design of gear components, effective driving forces/methods, and careful choices of supporting platforms/substrates. As an emerging field of research, efforts on identifying the important general criteria of such systems are demanded. As a vision, there are a few general challenges to be tackled:

- (1) **The stiffness of “soft” organic molecules.** From a number of theoretical studies [92-95], the stiffness of the gear component directly determines the number of gears limited as a train. In agreement with the results from the previous studies on HB-NBP and this work, they coincidentally suggest that the C-C single bonds with many degrees of freedom between the gear core and the teeth are the limitation of the current designs. The possibility of fabricating and manipulating nanoscale solid-state gears can be an alternative solution with the latest advance in lithography, e.g., helium ion beam lithography for the fabrication of sub-nanometer Si-chips [96].
- (2) **The mechanical gear-gear contact.** The gear-gear distance, the opening angle of successive teeth, and gear-gear interactions are critical criteria as demonstrated in various theoretical studies [93,95]. An understanding of fundamental forces is still heavily needed.
- (3) **The strength of the driving mechanism.** The input torque given by the STM tip manipulation (non-mechanical contact) is possibly too small for driving multiple interlocked molecule-gears. From the literature [74,75], a “molecular handle” has been found to be useful for facilitating the transmission of motion. It is however still an open question for such effect.

6 A Rotor and Nanocar in One Molecule

This chapter examines a single-molecule machine with two distinct functionalities, i.e., a rotor and a nanocar, depending on its conformations on the Au(111) surface. Such dual functionality allows the comparison of inelastic tunnelling electron excitation for a controlled translation or a unidirectional rotation on the same molecule and in the same experimental conditions. Parts of the text and figures are reproduced from ref. [97] with permission of American Chemical Society.

6.1 Rotors versus Nanocar

After the discussion of transmitting motion between single molecule-gears in Chapter 5, another two classes of single molecule machines will be discussed. In this case, by using inelastic tunneling electrons in the STM junction, the rotation and translation of molecules on surfaces can be excited. It is important to distinguish that the rotational directionality discussed in Chapter 5 is provided by the trajectory of STM lateral manipulation (i.e., mainly van der Waal forces), while the process of inelastic tunneling electrons excitation involves vibrational and electronic states of the molecule.

In order to trigger the rotation of a single molecule, a stable rotational axle for the restriction of lateral diffusion is essential. On the other hand, mobile physisorbed molecules with legs, wings, or wheels have been proposed to investigate translations induced by the STM tip [49,50,98-100]. The first two editions of the international Nanocar Race [48,50] have provided examples of controlled lateral motions on a surface induced by inelastic tunneling and electric fields.

While the classical motion (rotation and translation as the result) of molecules on surfaces can be excited in the STM tunneling junction by quantum processes, both semi-classical motions should share the same excitation process by first approximation. However, due to the nature of chemisorption and physisorption, it is experimentally not straightforward to directly compare both motions. In previous studies [47,78,89,101], either chemisorbed (strongly anchored rotor) or physisorbed (weakly adsorbed nanocar) molecules were studied individually with different types and structures of molecules. In this work, a molecule species demonstrates both functions, which is a rare (and even seems counter-intuitive) case for direct comparison. The following will present a zwitterionic molecule adsorbed on Au(111) with selective chemisorption or physisorption that can rotate in one direction or

translate controllably, depending on its conformation on the surface [97]. Motion analysis will give insights into electronic excitation process.

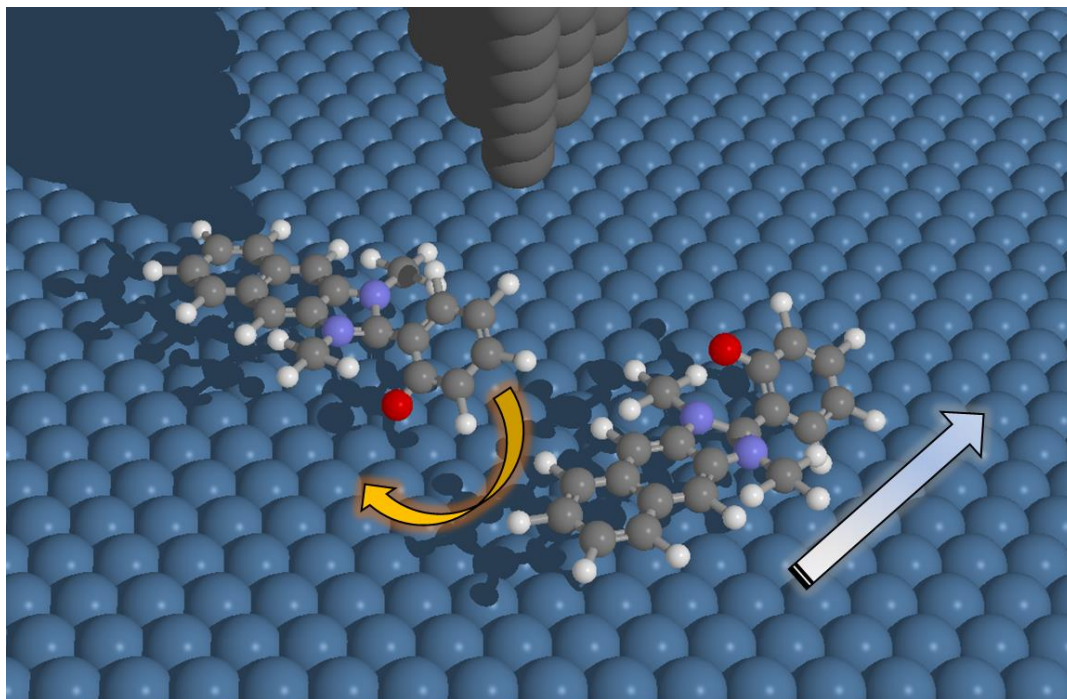


Figure 35. A Schematic diagram showing the co-existence of a molecule-rotor and a nanocar in the same species on surface.

6.2 Design of the molecule

2-(2-Methoxyphenyl)-1,3-dimethyl-1H-benzimidazol-3-ium iodide (o-OMe-DMBI-I) [102] and further DMBI derivatives have been first synthesized to be employed as air-stable n-type dopants in organic electronic devices [103]. It was discovered that during the sublimation process the molecules undergo partial decomposition reactions with the halide separation or the splitting of a methyl group [104]. In UHV conditions, previous work [19] found that when sublimating o-OMe-DMBI-I, the molecules undergo the dissociation reaction with the release of methyl iodide (the counterion) and the cleavage of the methoxy group (Figure 36a). As a result, the chemisorbed molecule on the Au(111) surface was found to be the zwitterionic phenolate DMBI-P. The study demonstrated that the chemisorbed molecule can rotate unidirectionally by applying STM voltage pulses.

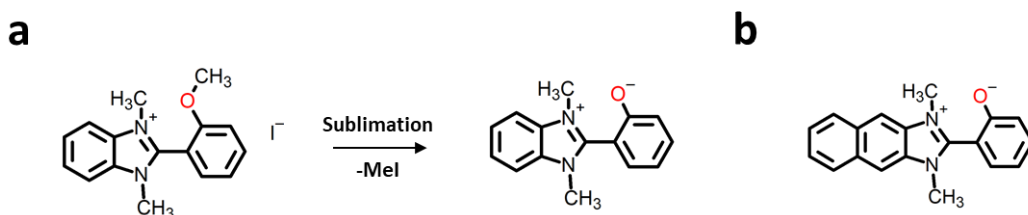


Figure 36. (a) Scheme of o-Me-DMBI-I undergoing the dissociation reaction (cleavage of MeI) during sublimation under UHV conditions. (b) The design of zwitterionic DMNI-P.

In this work (Figure 36b), synthesized by the group of F. Lissel (IPF Dresden), a zwitterionic molecule (without the need of undergoing the disassociation reaction during sublimation) is envisioned for further studies on its motion behavior. A zwitterionic molecule has a net charge of zero, but negative and positive charges on individual atoms in its structure. For the new design, the zwitterionic phenolate makes the methoxy cleavage superfluous. It also has an elongated part to a naphthyl, obtaining 2-(1,3-dimethyl-1H-naphtho[2,3-d]imidazol-3-ium-2-yl) phenolate (DMNI-P).

6.3 Deposition on Au(111)

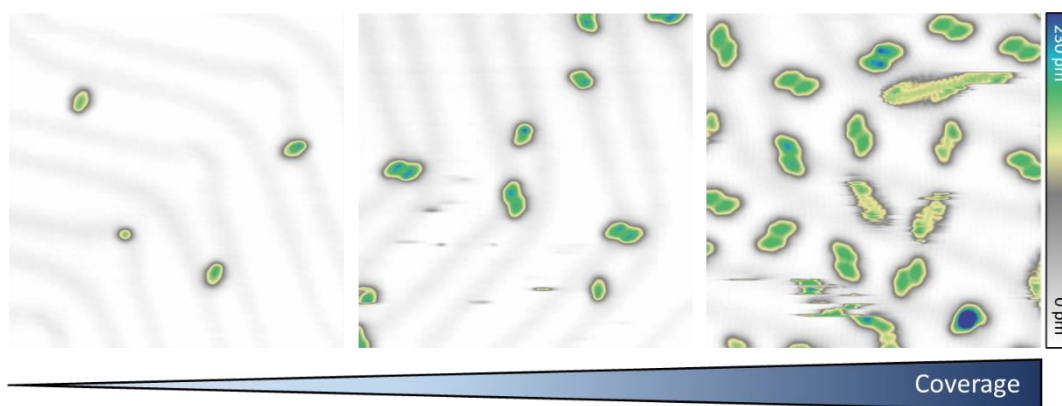


Figure 37. STM images of DMNI-P on Au(111) at increasing coverage: low (6 DMNI-P in 40 nm × 40 nm), moderate (38 DMNI-P in 40 nm × 40 nm), and high (92 DMNI-P in 40 nm × 40 nm) coverage, respectively. Close-up STM images (20 nm × 20 nm) were taken under (a – b) $I = 5$ pA, $V = 0.2$ V, and (c) $I = 5$ pA, $V = 0.1$ V.

The molecular coverage can be selected by varying the parameters of thermal deposition ($T_{\text{evap}} = 225$ °C) of the DMNI-P molecules under UHV conditions on the Au(111) surface held at room temperature. In this case, increasing the molecular deposition time finds higher coverage as shown in Figure 37. STM experiments were performed after cooling the sample to $T = 5$ K. Single molecules were first found from the sample with relatively low coverage (6 DMNI-P in 40 nm × 40 nm). Then, a mixture

of singles and dimers was observed when the sample reached moderate coverage (38 DMNI-P in 40 nm x 40 nm), and eventually dimers become dominant when increasing to high coverage (92 DMNI-P in 40 nm x 40 nm). Single molecules and dimers can be observed where the majority occupies the kinks of the Au(111) reconstruction sites. The upcoming section focuses on the sample with low coverage, and the corresponding chemisorbed molecule-rotors. Different adsorption geometries have been observed when the molecules form dimers.

6.4 Chemisorbed DMNI-P: Rotor

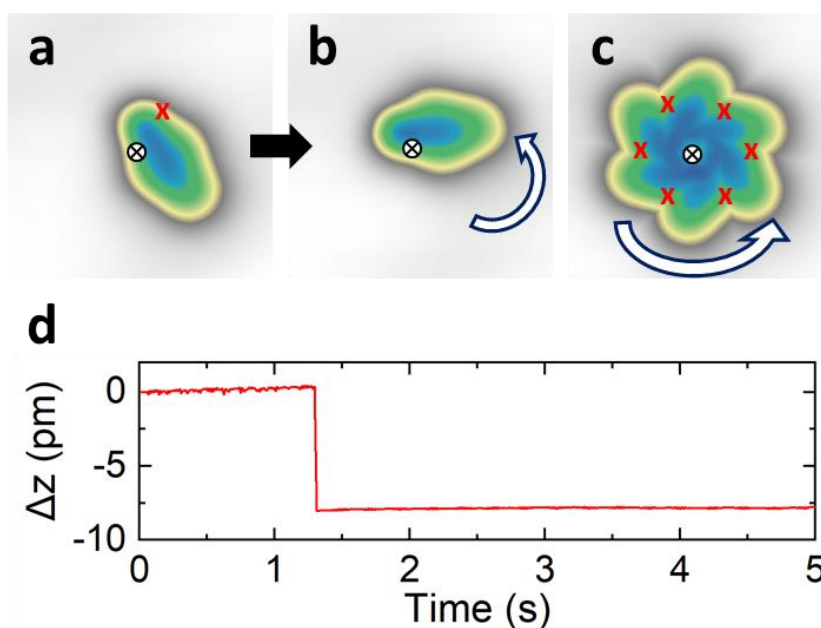


Figure 38. Anchoring and rotation of DMNI-P rotor. (a) STM image of the molecule anchored at a fixed position (black cross); a voltage pulse is applied at the position of the red cross. (b) STM image of the same DMNI-P rotor after the voltage pulse, showing a one-step rotation ($\theta = 60^\circ$; CCW); the anchoring point (center of rotation) is indicated in black. (c) By combining the images of the six stations rotating in one direction (CCW), a common anchoring point is identified (black cross). (d) Exemplary tip-height over time plot $\Delta z(t)$ measured during a pulse. A voltage pulse was applied under $I = 250$ pA and $V = 0.5$ V for 5 s in constant current mode. STM images ($3 \text{ nm} \times 3 \text{ nm}$) were taken at $I = 5$ pA and $V = 0.2$ V.

From Figure 38a, an isolated single adsorbed DMNI-P shows the naphthyl unit at the tail of the molecule together with the widening of the structure roughly in the middle, as the two methyl groups of the imidazole unit appear wider in the STM image because they are not planar.

The STM tip apex is positioned above the position of the carbon atom opposite to the oxygen atom of the molecule (red mark in Figure 38a), and subsequently a STM voltage pulse is applied at constant current mode. A sudden change in the relative tip height

(Figure 38d) from the time series can be recorded, indicating a motion has occurred. It is important to note that distinguish from the cases in Chapter 5 which focuses on the lateral manipulation with low bias voltage and tunneling current (i.e., van der Waals interactions are the dominant force). This study focuses on how inelastic tunneling electrons excite the motion of DMNI-P molecules.

The subsequent image (Figure 38b) shows that the molecule has rotated 60° counterclockwise (CCW) to the next stable station. By applying a succession of pulses following the position of the molecule, a complete CCW rotation of the molecule over six stations of 60° each can be observed, corresponding to the stable adsorption positions on Au(111). The center of rotation (axle) can be experimentally determined by superimposing the STM images of six stations from a complete rotation cycle (Figure 38c). The adsorption geometry calculated by density functional theory (DFT) (calculations done by D. A. Ryndyk, TU Dresden) is shown in Figure 39b – c confirming that the single DMNI-P chemisorbs on Au(111) by charge back-donation at the oxygen position.

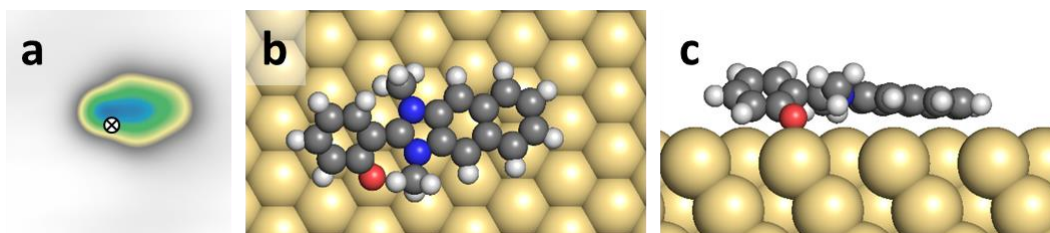


Figure 39. (a) DMNI-P rotor on Au(111). The anchored point is indicated as black cross. (b – c) Adsorption geometry of the anchored DMNI-P in (b) top and (c) side view respectively, calculated by DFT (calculation done by D. A. Ryndyk).

By investigating 251 pulses on different rotors, the molecule rotates in steps of 60° and in the same direction in 99% of the cases. Recording continuous rotation at different stations is not possible by keeping the tip at the same position in this case since the entry port for the electron tunnelling allowing a one-step rotation is not located at the anchoring point. In other words, it is necessary to reposition the lateral tip position after each one-step rotation (Figure 38c). When applying pulses at negative biases, the molecule rotates in the opposite direction, compared to those at positive biases. Moreover, from the structure of DMNI-P with the extended 6-membered ring (naphthyl group) compared to DMBI-P, it is expected that the effects from the molecule-surface interactions, e.g., van der Waals forces, will become stronger. Indeed, statistical analysis (Figure 40) shows that when the rotor goes across the solitons of the herringbone reconstruction (from 1 to 2 and 3 to 4 for this case), it requires a longer time for the rotational events. It is known that it is a common effect from the solitons that gives a slightly higher energy barrier to overcome [98].

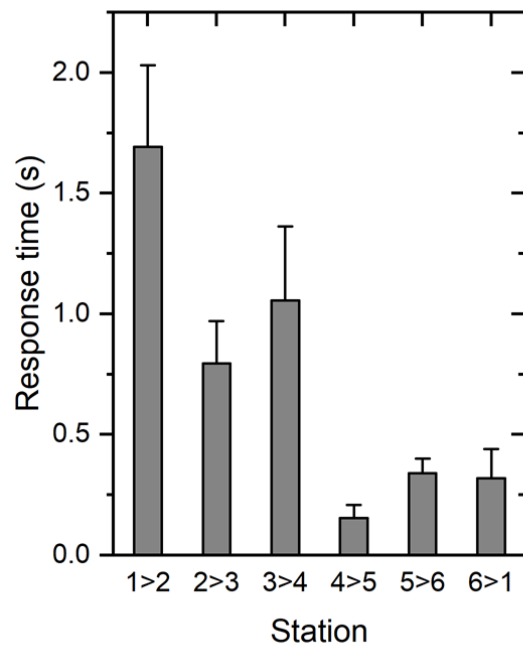


Figure 40. Response time influenced by different adsorption positions.

6.5 Interchangeable chirality by flipping the rotor

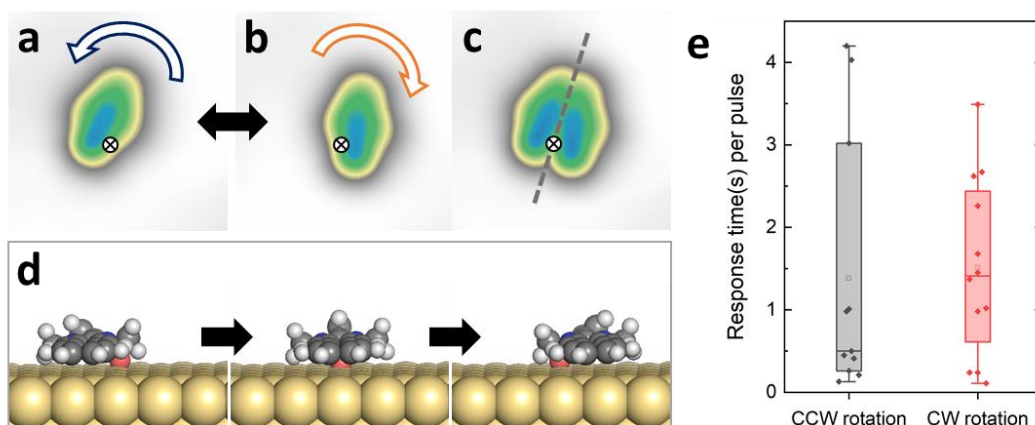


Figure 41. Flipping of the chiral rotor molecule leads to a change of rotation direction (CCW \rightarrow CW). (a) Initially, by applying positive voltage pulses ($V = 0.4 - 1.0$ V, $I = 500 - 700$ pA), the rotor rotates in the CCW direction. Then, a stronger pulse is applied above the molecule ($V = 3.5$ V, tip-surface distance = 10 Å; position not shown). (b) After the pulse, subsequent manipulations show that the rotation direction has been changed from CCW to CW. (c) Combining the two images (a) and (b) by $\text{img } c = \max(\text{img } a, \text{img } b)$ gives rise to the mirror image, indicating that the molecule is symmetrically flipped to the opposite side without losing the anchoring point (indicated by black marks). (d) Sequence of DFT calculated adsorption geometries illustrating the flipping (calculations done by D. A. Ryndyk). (e) Comparison plot between CCW and CW rotation of the effective pulses (rotational events) in terms of the response time with the same pulsing parameter ($I = 500$ pA, $V = 500$ mV). No significant behavioural difference (t-test: $p = 0.71$) between the two types of chirality.

When DMNI-P adsorbs on the surface, it is a chiral molecule (i.e., becomes chiral on a surface) due to the asymmetric phenolate group. This gives rise to the opportunity to study the motion behaviour of different types of chirality due to the fact that the DMNI-P molecule rotates in another direction if it has a different chirality. In other words, when applying voltage pulses at positive bias, the right-hand molecules (e.g., Figure 38) always rotate CCW, and the left-hand ones rotate CW.

Investigations on the relationship between chirality and molecular rotary motion by means of STM manipulation have been long: e.g. prochiral molecules manipulated by chiral STM tips [78,105], and C_2H_2 molecules physisorbed on the chiral PdGa(111) surface [106]. These studies have shown that the chirality originating from STM tips, molecular structures, and/or functional surfaces plays an important role in inducing unidirectional rotation by breaking the symmetry in the system (producing useful work as a goal in the field of single molecule machinery). More details about the origin of the unidirectional rotation of DMNI-P will be discussed in the next Chapter. The following presents the interchangeable chirality of DMNI-P by STM manipulation.

In Figure 41, flipping of the chiral rotor leads to the change of rotation direction without breaking the Au-O bond, from CCW to CW in this particular case. From Figure 41a, one can see the STM image of a left hand-DMNI-P, which rotates CCW by positive voltage pulses (typically 0.4 – 0.7 V). After applying a stronger voltage pulse (1.5 – 3.5 V) or by lateral manipulation, the molecule moves (flips) to the opposite side of the bond without changing its anchoring point (Figure 41b). The STM image after flipping clearly shows that the molecule presents the right-hand chirality. By applying pulses with similar parameters, the unidirectional rotation in the opposite direction is observed, i.e., the flipped molecule rotates now clockwise (CW). The flipping is illustrated in Figure 41c after superimposing the two images of Figure 41a and b, where the left-hand and right-hand but the same molecule shares the same anchoring point. Note that the flipping can be repeated several times by the same method, and with different modes of manipulation (e.g., laterally).

The sequence of DFT calculations (Figure 41d) done by D. A. Ryndyk has revealed that the rotation of the phenolate-head of the molecule gives rise to such flipping while the naphthimidazole remains adsorbed on the surface shifted laterally. When comparing the rotational behaviour of the two types of chirality (Figure 41e), CCW rotation has shown no significant difference (t-test: $p = 0.71$) to CW rotation with the same pulsing parameter ($I = 500$ pA, $V = 500$ mV).

6.6 Chemisorption versus physisorption of DMNI-P

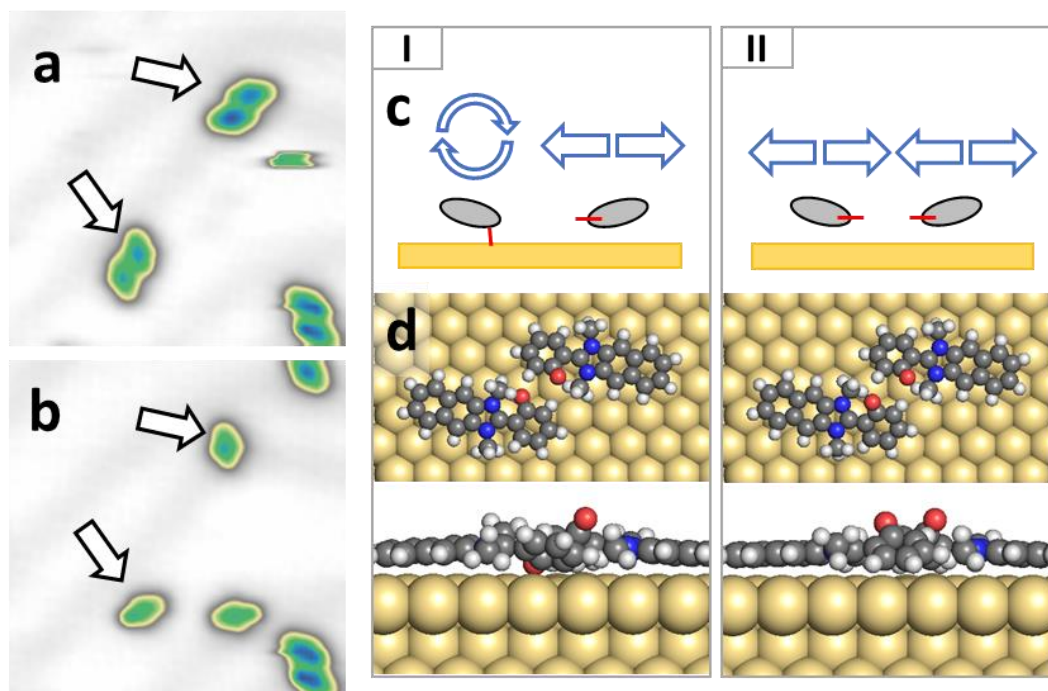


Figure 42. Separation of two different cases of dimers. STM images ($10\text{ nm} \times 10\text{ nm}$) (a) before and (b) after applying a voltage pulse (5 V, outside of the image), respectively. Dimers can be isolated into single ones (arrows). (c) Schematic diagrams of cases **I** and **II** after separation of dimers. Case **I** shows a molecule rotating and the other translating, and **II** shows both translation behaviours. The red lines illustrate the oxygen moieties undergoing chemisorption or physisorption on the Au(111) surface. STM images were taken under (a) $I = 20\text{ pA}$, $V = 0.2\text{ V}$, (b – c) $I = 10\text{ pA}$, $V = 0.2\text{ V}$. (d) Adsorption geometry calculated by DFT for **I** and **II**, respectively (calculations done by D. A. Ryndyk).

As mentioned earlier, coverage-related adsorption geometries have been observed, where from moderate coverage, DMNI-P dimers start becoming dominant on the Au(111) surface. Figure 42a presents the STM image of a few dimers, formed by identical DMNI-P molecules. By applying pulses, the dimers can be separated into single DMNI-P molecules. In this particular case, a strong voltage pulse was applied outside of the scan area (e.g. 5 V, 160 pA; laterally about 8 nm away from the target). An equivalent separation can be obtained by applying weaker pulses (e.g., $\sim 2\text{ V}$, 5 nA) directly above the dimer. After separation (Figure 42b), single adsorbed molecules can be found, where at least one of both molecules has experienced a lateral displacement. In other words, different from the anchored rotor, a certain population of DMNI-P can be laterally moved on the surface by voltage pulses, behaving like a nanocar. We have performed $n = 41$ dimer separations, about 40% of them result in two separated nanocars and 60% in a nanocar and a rotor.

The schematic Figure 42c summarizes the two observed adsorptions after dimer separation: Case **I** shows that the dimer forms a rotor and a nanocar; case **II** represents that both molecules can translate on the surface, i.e., they are nanocars. The red lines illustrate the phenolate undergoing chemisorption (Au-O bond) or physisorption on the surface. The corresponding DFT calculations (done by D. A. Ryndyk) demonstrate dimer **I** (rotor – nanocar), and dimer **II** (nanocar – nanocar), respectively. Hydrogen bonds lead to the formation of dimers, given the fact that DMNI-P is a zwitterionic molecule. The O atoms point to the second molecule, thus stabilizing each other. The calculated binding energy is 0.2 eV, which is sufficient for DMNI-P to form dimers in the gas phase (i.e., before the molecules reach the sample during deposition).

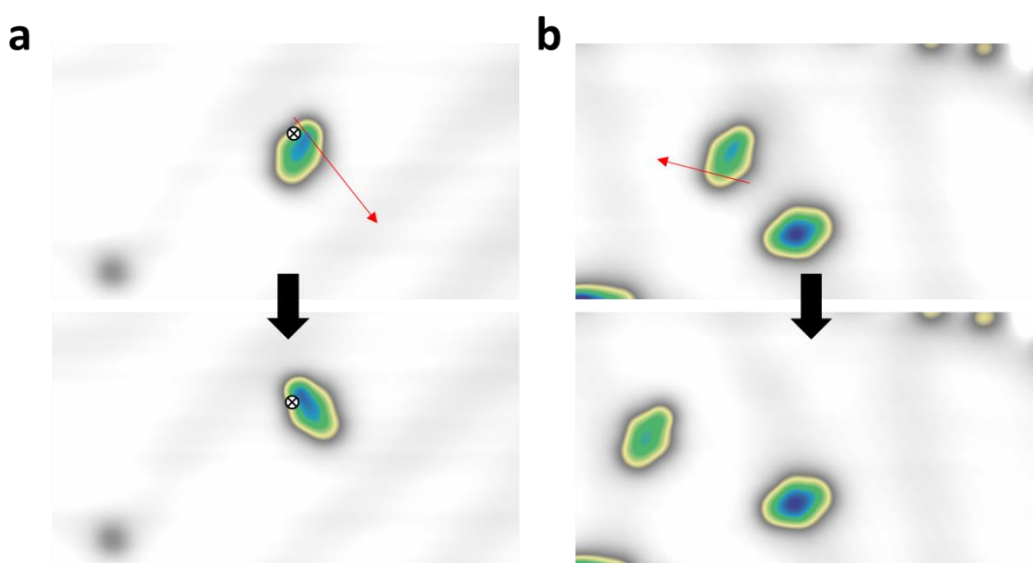


Figure 43. Lateral manipulation of DMNI-P rotor and nanocar. Red arrows indicate the trajectory of the manipulation. (a) Manipulation ($I = 1.3$ nA, $V = 10$ mV) of a rotor. The rotor is strongly anchored on the surface (purple dot as the axle). The rotor rotates CCW corresponding to the tip trajectory. (b) Manipulation ($I = 0.4$ nA, $V = 10$ mV) of a nanocar. After the manipulation, the subsequent image shows a lateral displacement of the molecule, following the trajectory of the tip. STM images (10 nm \times 5.5 nm) were taken at (a) $I = 10$ pA and $V = 0.2$ V, and (b) $I = 5$ pA and $V = 0.2$ V.

Since the STM topographies do not show obvious contrast for distinguishing between the adsorption modes, lateral manipulation has been employed for pushing the molecule as control experiments before the study of motion. The DMNI-P molecules are manipulated by the STM tip where the red arrows indicate the trajectory. In Figure 43a, after manipulation ($I = 1.3$ nA and $V = 10$ mV), the molecule merely rotates following the trajectory. By comparing the images before and after the displacement, a clear anchoring point can be observed, and hence, confirming the particular molecule is chemisorbed on the surface. On the contrary, after manipulating ($I = 0.4$ nA and $V = 10$ mV) the molecule in Figure 43b, a lateral displacement has been observed

where the displacement follows the tip trajectory. The molecule at the centre acts as a reference.

6.7 Physisorbed DMNI-P: Nanocar

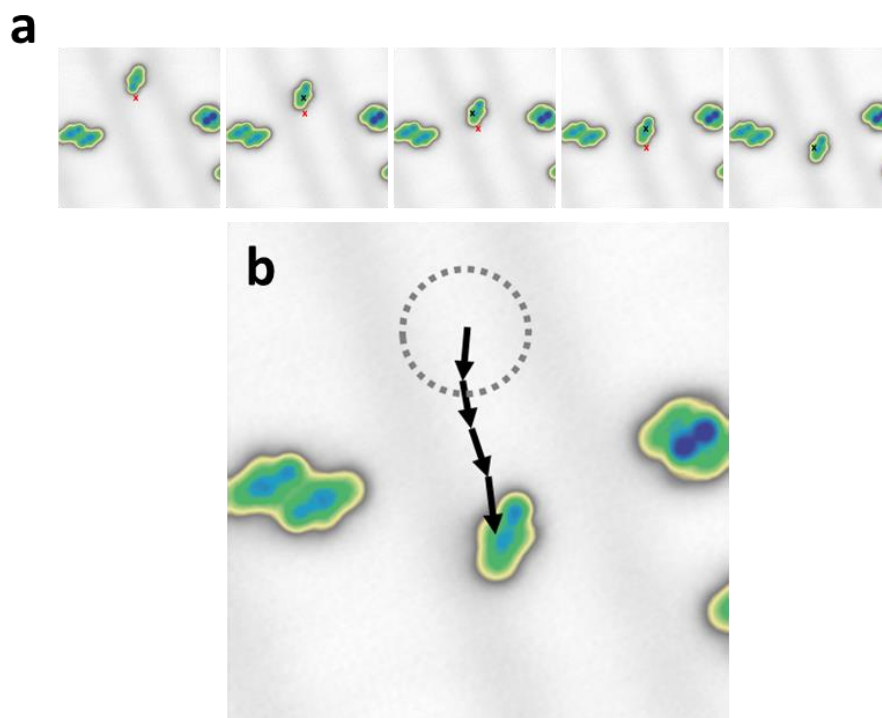


Figure 44. Manipulation of DMNI-P nanocar. (a) Controlled lateral translation starting from top to bottom of the $10\text{ nm} \times 10\text{ nm}$ area can be observed, where the molecule moves towards the pulsing positions. The red marks indicate the position of the tip during the voltage pulses before the displacement, respectively ($V = 0.5 - 0.8\text{ V}$). (b) Trajectory of the molecular movement from (a). STM images ($10\text{ nm} \times 10\text{ nm}$) were taken under $I = 21\text{ pA}$ and $V = 0.25\text{ V}$.

The movement of the DMNI-P nanocars by applying voltage pulses has been investigated. Figure 44a presents a lateral translation sequence of a nanocar. By applying pulses (positive bias) near the molecule, the nanocar translates on the Au(111) surface in a controllable way. In the case of positive bias, the nanocar is attracted by the tip. Similar to the case of the rotors, a sudden jump of the tunneling current signal indicates that a hopping event occurs. In this particular sequence, the nanocar has travelled about 4 nm with four individual pulses (Figure 44b). After investigating 379 pulses on different molecules, the molecule translates towards the tip position with very high precision at positive bias, independent of its chirality. On the contrary, negative bias leads to random motion (e.g., away from the tip). Figure 45 shows an exemplary sequence when applying negative bias. The nanocars can be driven at $V \geq 0.4\text{ V}$ and a few hundred pA, very similar to the case of the rotors. The

calculated adsorption geometry of physisorbed DMNI-P done by D. A. Ryndyk (Figure 46) has shown that the phenolate remains freely without binding to the Au(111) surface.

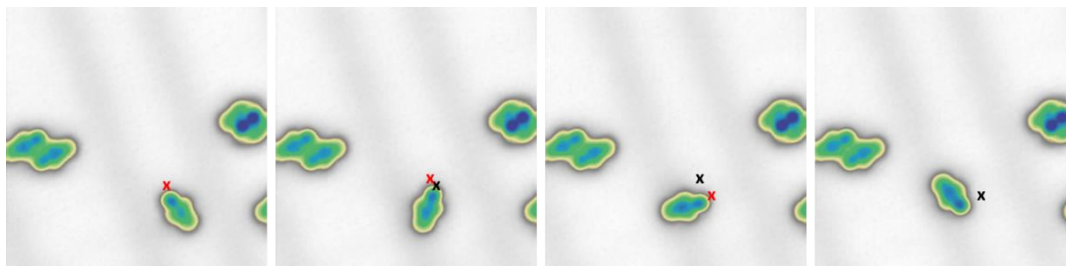


Figure 45. Manipulation of DMNI-P nanocar by negative bias. The molecule moves in random directions and away from the tip position. The voltage pulses were applied at -0.8 V and ~ 700 pA. The red and black marks indicate the position of the tip during the voltage pulses before and after the displacement. STM images ($10\text{ nm} \times 10\text{ nm}$) were taken under $I = 21\text{ pA}$ and $V = 0.25\text{ V}$.

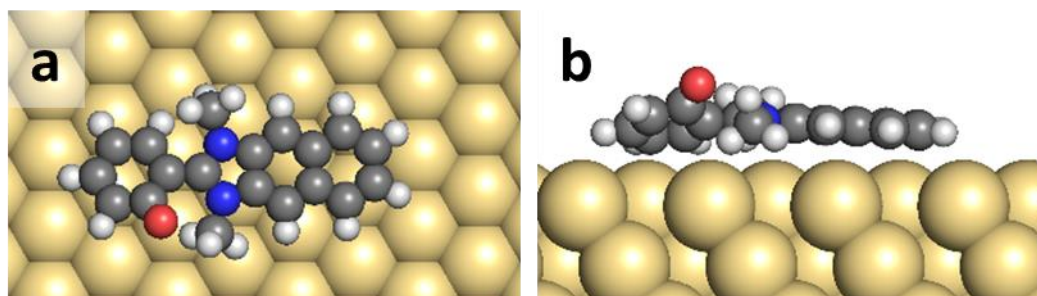


Figure 46. Adsorption geometry of the DMNI-P nanocar in (a) top and (b) side view respectively, calculated by DFT (calculations done by D. A. Ryndyk).

6.8 Action spectra: The role of inelastic tunneling electrons

A molecule-rotor and nanocar in the same species provide a unique opportunity for comparing the parametric dependence for movement. In STM tunnel junction, the initial excitation mechanism for rotation and translation is a priori the same. However, rotation requires a strong local molecule-substrate interaction providing a rotational axle, while a nanocar is laterally free to translate if its adsorption is weak. The comparison is presented as follows.

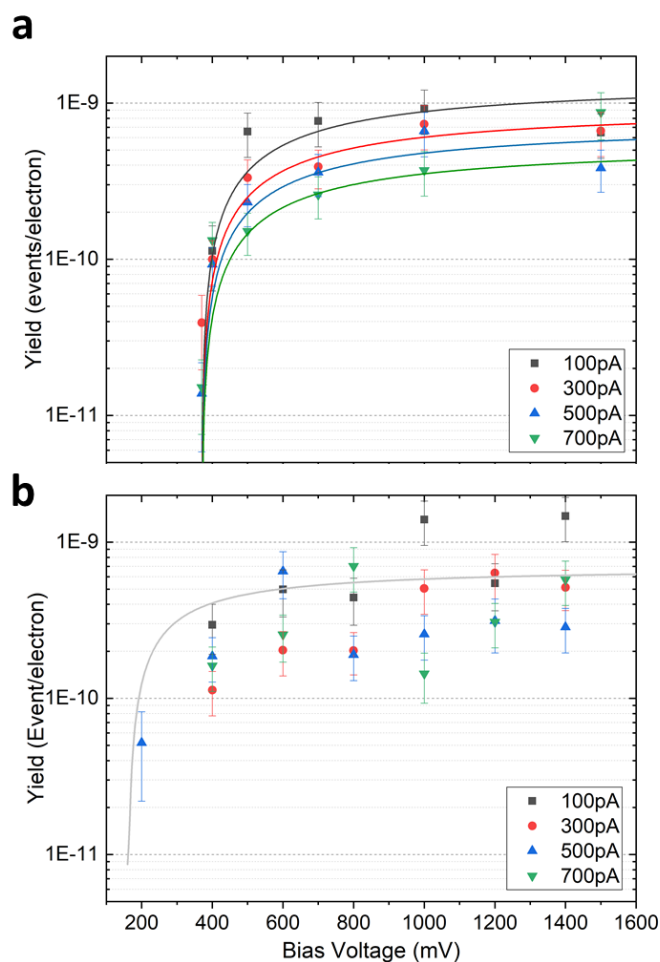


Figure 47. Yield (motion probability per electron) versus voltage bias for DMNI-P rotor and nanocar measured by individual pulses with the fixed tunnelling current. The curves for the rotor case have been calculated by fitting the experimental action spectra according to the theory of Ref. [107], obtaining a threshold at 370 meV. In the bottom panel, the curve is a simulation of the action spectra of the nanocar considering a threshold voltage of 165 meV and an overall yield constant of 3.5×10^{-10} event/electron. The fitting of the data at different currents was not possible because of the data spread. All the fitting curves were simulated by R. Robles and N. Lorente (CFM, Spain).

Figure 47 shows the electronic yield, or *action spectra* [107], for DMNI-P rotation and translation in the function of applied bias voltage from different fixed tunneling current. Action spectrum is defined as a reaction rate or yield as a function of bias voltage. It allows a quantitative analysis of the single adsorbate vibrational modes. In 1998, from a seminal work [57], B. C. Stipe, M. A. Rezaei, and W. Ho detected the vibrational modes from the rotation of O₂ molecule adsorbed on Pt(111) induced by inelastic tunneling electrons. This fascinating result raised great interest and extended to many more examples, e.g., the transformation yield of trans-2-butene on Pd(110) [108], and the hopping yield of isolated H₂O and D₂O molecules on Pt(111) [18].

For the cases of DMNI-P rotor and nanocar, the different adsorption positions of the molecule on the Au(111) surface reconstruction cause a spread of the experimental data, which apparently influences stronger in the case of the mobile nanocars. Totally 251 rotation events and 379 translation events were investigated statistically. To plot the yield, first of all, the response time of each event was extracted from the $z(t)$ signal (Figure 38d). The values were converted to the average rate ($1/t$), then the experimental yield was plotted by calculating $Y = R/I(e)$.

At $V > 400$ mV, the yield for both cases is very similar, resulting in a yield of about 5×10^{-10} event/electron. A threshold voltage at around 400 mV is clearly observed in the case of rotation, which can be explained by the onset of C-H stretch mode of the methyl group at the opposite side of the Au-O bond [19]. The fitting of the action spectra is done by using Eq. 5.1 [107],

$$Y = K \left[\frac{2}{\pi} \left(1 - \frac{\hbar\Omega}{eV} \right) \left(\tan^{-1} \frac{2(eV - \hbar\Omega)}{\sigma} + \tan^{-1} \frac{2\hbar\Omega}{\sigma} \right) + \frac{\sigma}{2\pi eV} \log \frac{((\hbar\Omega)^2 + (\sigma/2)^2)}{((eV - \hbar\Omega)^2 + (\sigma/2)^2)} \right] \quad (5.1)$$

where K is the overall yield that controls the order of magnitude of the measured Y , V is applied bias, Ω is the angular frequency of the vibrational mode mediating the reaction, and σ is the broadening of the reaction threshold. The fitting curves are controlled by two parameters; Ω fixes the threshold of a non-zero yield, and σ controls how fast the yield goes from zero to a measurable value. In this case, a threshold at 370 meV is obtained for the case of rotation. Here, the threshold/onset refers to the minimum energy required as an “entry port” for exciting an effective rotation or translation at specific vibrational modes of the molecules.

On the other hand, for the case of translation, it is more favorable at a lower bias ($V < 400$ mV) compared to unidirectional rotation. This indicates that low-energy vibrations are sufficient for inducing translation in the non-anchored physisorbed

conformation. Higher energy is needed to overcome the rotational barrier of the anchored chemisorbed conformation, which can be reached by exciting the C-H stretch mode. Done by R. Robles and N. Lorente (CFM, Spain), calculations of the vibrational modes of DMNI-P show similar modes for both rotor and nanocar (Figure 48). It also confirms the threshold of the C-H stretch mode at 370 meV and mixing of multiple lower vibrational modes, including the C-C and C-N stretch modes between 155 meV and 167 meV. The simulated curve in the lower panel of Figure 47 shows a threshold voltage of 165 meV, in good agreement with the experimental data. The most distinguishable structural difference between rotors and nanocars is essentially the Au-O bond. However, according to the simulations, the extra vibrational mode for the Au-O bond seems not to take an important role since the frequency is located at $V < 10$ meV. All experimental data and calculations suggest that inelastic tunneling electrons take the role of both DMNI-P rotation and translation at the onset of different vibrational modes.

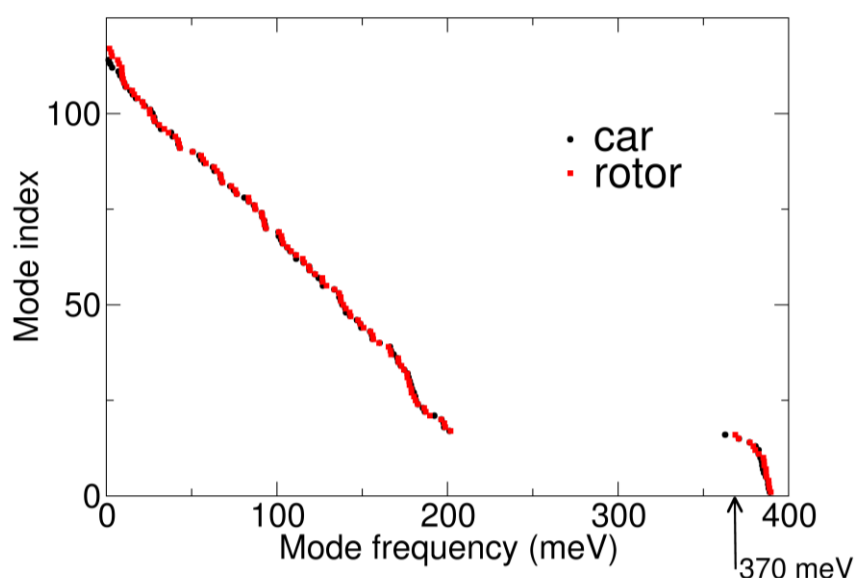


Figure 48. Simulation of vibrational modes for DMNI-P nanocar and rotor on Au(111), starting from the two adsorption geometries determined by DFT. The vibrational frequency is very similar between nanocar and rotor. Between 155 meV and 167 meV, C-C and C-N stretch modes are found, which are of interest for the nanocar. All calculations were done by R. Robles and N. Lorente (CFM, Spain).

6.9 Exploring the minimum energy for rotation

The simulation of the vibration modes for DMNI-P shed light on the lower vibration modes below 370 meV. This leads to an interest in experimentally exploring the minimum required tunneling current and voltage for directed rotation at 5 K. For the case of the rotor, by progressively reducing the bias voltage, the time needed for an effective event has extended from a few seconds to more than 10 hours (Figure 49a). Surprisingly, the first one-step directed rotation is observed while keeping the tip apex above the molecule at the same position for 35 950 s (around 10 h) in a 12 h pulse time window.

By measuring the response time in the range of $150 \text{ mV} \leq V \leq 700 \text{ mV}$, Figure 49b shows the statistics ($n = 139$ pulses) of the response time over bias voltage. Each response time is measured on the corresponding $z(t)$ curve (such as Figure a). The yield (rotations/electron) can then be calculated by $Y = R(I/e)$. For $V > 400 \text{ mV}$, the nearly constant yield of about 5×10^{-10} rotations/electron can be observed, in which this can be assigned to the onset of the C - H stretch vibrational mode at 370 meV. At lower bias voltage, a sharp drop of the yield between 330 and 400 mV can be seen, while another nearly constant region appears at 200 – 300 mV. For $V < 200 \text{ mV}$, a rapid decrease of yield is again observed, reaching the low yield of 6×10^{-15} rotations/electron at 150 mV. By fitting the data, there are two onsets revealing the energies at 165 meV and 370 meV. They correspond to a large density of the deformation mode (C-C stretch manifold) and the C-H stretch mode of DMNI-P, respectively. At low energy, these modes can inelastically contribute to providing the rotational energy for the unidirectional rotation. Note that this result is beneficial for the investigation of the interplay between thermal and electronic excitations shown in Chapter 7.

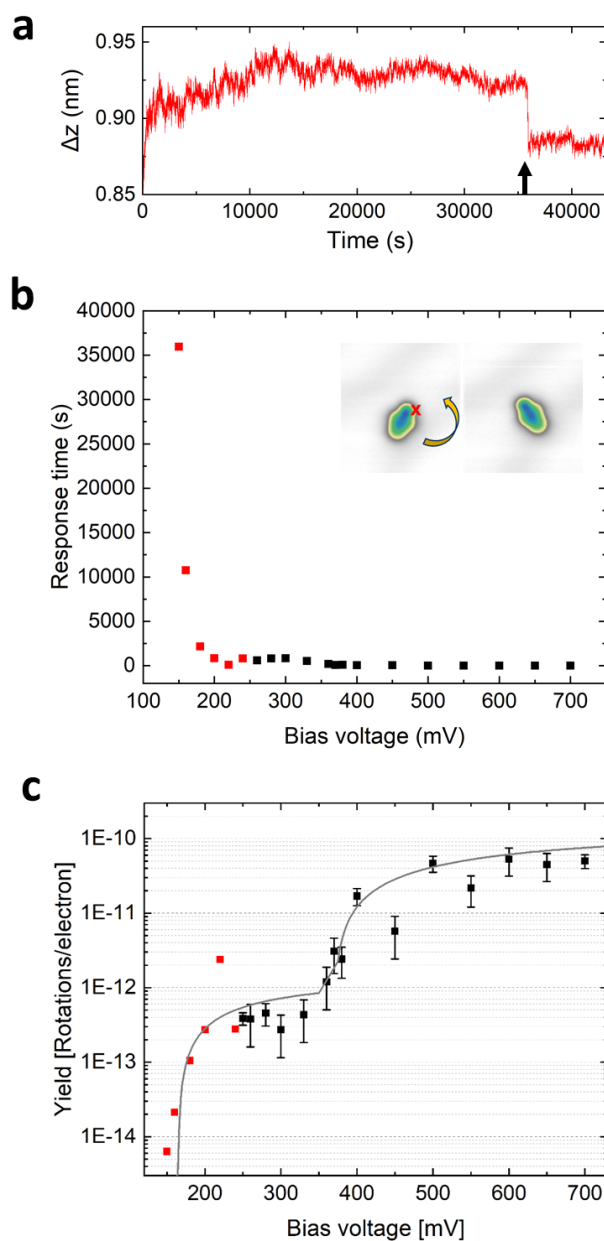


Figure 49. (a) Relative tip height time series $\Delta z(t)$ measured at the specific position to DMNI-P. A rotation event was observed after 35 950 s (around 10 h) in a 12 h pulse ($I = 700$ pA, $V = 150$ mV). (b) Response time (the time needed for an effective rotation event) over the applied bias voltage. Inset shows a one-step directional rotation of DMNI-P, where the red cross depicts the position of the tip during voltage pulse. (c) Plot of yield (rotations per electron) versus bias voltage for the rotor at pulses fixed at $I = 700$ pA. Due to this very long waiting time (up to 10 h) for the molecule-rotor to perform a one-step rotation, only one red-marked data point was recorded in (b). The data have been fitted with the action spectra function of Ref.[107] for two modes, one at 165 mV and one at 370 mV.

6.10 Electric field induced motion

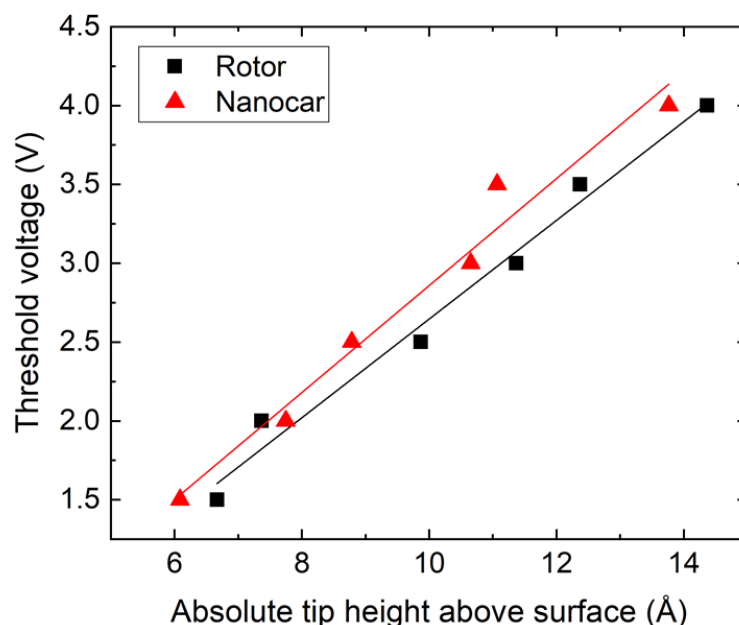


Figure 50. Threshold voltage for movement versus tip height, comparing the behaviours of molecule-rotor and nanocar. The absolute tip height was determined experimentally by the tip-surface point contact position. The slope of the linear fit function for molecule-rotor (black line) is $0.31 \text{ V } \text{\AA}^{-1}$, and for nanocar is $0.34 \text{ V } \text{\AA}^{-1}$, respectively.

As stated in Chapter 2, another possibility to manipulate molecules is via electrostatic interactions due to the presence of electric field in the STM junction ($|V| > 0$). On the other hand, tunneling electrons are also present in the junction. In other words, mixing the electric field effect with tunneling electrons, it is challenging to clearly distinguish the contribution from each excitation mechanism. In this case, it has been shown in the previous section (Figure 47) that at relatively low bias voltages, the inelastic tunneling electrons play the dominant role in the obvious energy onset at different vibrational modes. However, given the zwitterionic nature of DMBNI-P which has a large charge separation internally, it is important to include the electric field effect at relatively high voltages. Note that the polarity of the applied voltage can change the rotational direction (rotor) and the directed translation behaviour to less controllable (nanocar).

In this case, electric field induced motion (at high voltage; $V \geq 1.5 \text{ V}$), no or almost no tunneling current recorded) can excite the DMNI-P rotors and nanocars. The zwitterionic nature contributes to such electrostatic effect at high voltage. Figure 50 shows a plot of threshold voltage for movement over a range of tip height. The tip height was calibrated experimentally by the tip-surface point contact position (constant height mode). The data reveal a linear correlation between the threshold

voltage and tip height, with the slope of $0.31 \text{ V } \text{\AA}^{-1}$ and $0.34 \text{ V } \text{\AA}^{-1}$ for rotation and translation, respectively, in the range of 1.5 V to 4.0 V. A similar behaviour was reported for inducing motion of a metal-organic complex with a large charge separation adsorbed on Au(111) at the slope of $0.36 \text{ V } \text{\AA}^{-1}$ [47].

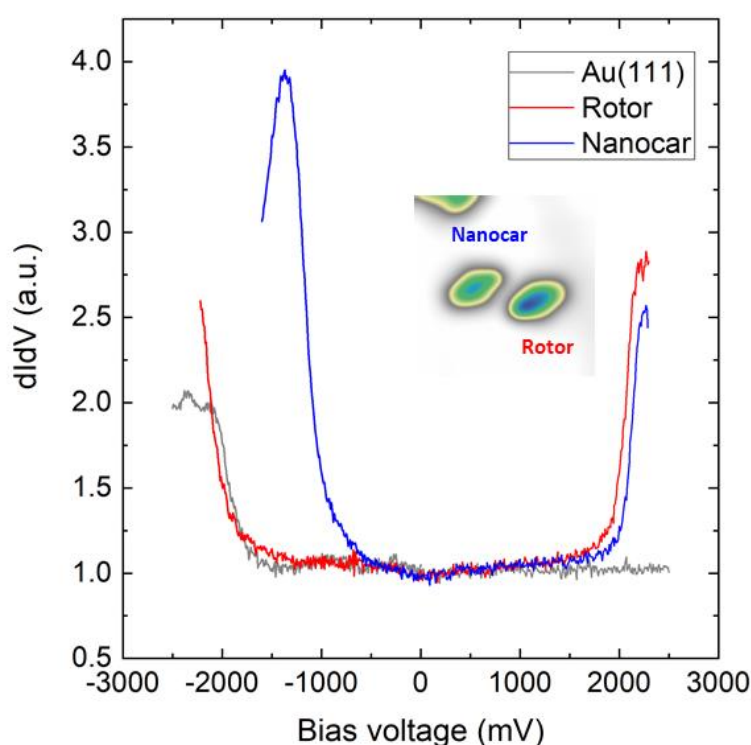


Figure 51. Scanning tunneling spectroscopy (STS) of the DMNI-P rotor (red) and nanocar (blue).

Another argument can be made where at high applied voltages, it is possible to inject tunneling electrons into the electronic excited states (HOMO and LUMO). To measure the electronic structure, scanning tunneling spectroscopy (STS) has been recorded for both the rotor and nanocar. For positive voltages, a well-resolved resonance at about 2.2 V, which can be assigned to the lowest electronic excited state for both cases. For negative biases, the highest electronic excited state for the nanocar has been shown at $V = -1.3 \text{ V}$. For the case of the rotor, a rapid climb of dI/dV signal has been observed at $V > 2.0 \text{ V}$. Due to the challenging spectroscopic measurement on a mobile molecule (i.e., exciting molecular movement at high V which frequently disturbs the measurements), the range of dI/dV measurement was limited.

Related to the movement, DMNI-P rotor and nanocar have a very similar lowest electronic excited state at around 2.2 V. At this high bias voltage, it is possible that the motions can benefit from the contribution of both inelastic tunneling electrons and electric field (Figure 51) at the electronic excited state are observed. A limitation here

is to experimentally disentangle the individual contributions of different excitations at the higher voltage bias regime ($V > 2.0$ V).

6.11 Summary and outlook

In this Chapter, a single-molecule machine shows two distinct functions depending on its adsorption conformation. Simultaneous observations of (1) rotors that are anchored at a fixed point (Au–O bond), and (2) mobile nanocars that can controllably translate across the surface with atomic precision were possible, thanks to the coverage-related selectivity. The direction of rotation (rotor) depends on its chirality (intrinsic symmetry breaking) on the surface. This can be inverted by manipulation, flipping the chirality without changing the anchoring position. On the other hand, the nanocar shows a bias polarity dependence on its directed motion, where positive bias leads to controlled translation, while negative bias leads to random motion.

Although the initial excitation mechanism for rotation and translation is a priori the same, the analysis of the electronic yield (event/tunneling electron), simulated ro-vibrational modes, electric field effect, electronic resonances (excited states) from STS provide insights on their interplay.

- (1) For bias voltage $V > 400$ mV, the yields for rotation and translation are similar.
- (2) At $V \leq 400$ mV, the nanocar retains a relatively high yield while the rotor shows a clear onset at 370 mV, which is ascribed to the C-H stretch mode. The combined experimental and calculated results reveal that low-energy vibrational modes at 150 – 170 meV (e.g., C-C stretch and C-N stretch modes) are sufficient to lead to translation for the non-anchored nanocar.
- (3) Applying the local electric field ($V > 2.0$ V) from the tip is able to induce rotation and translation in a similar way, while from the STS measurements, the lowest electronic excited states for both nanocar and rotor appear at 2.2 V. Hence, it is challenging to distinguish the individual contributions from different excitations at this high bias regime.

On the basis of the results, there are several possible directions and questions for exploration. It would be an important step if one can control the interchangeable functions, for example, switching from nanocar to rotor and vice versa at will. In this study, no change of conformation, and hence the functions were observed. One possible way is to introduce a switching group that can promote bistable chemical and electronic structures, where such switching is reversible by means of manipulation. However, in this case, chemisorbed molecules have to be excluded since they bind strongly on the surface, making it difficult to switch to another state/conformation.

Another possible direction is the investigation of a “multi-mode” single molecule machine, where within the same chemical structure, different functions like unidirectional rotation and switching can be induced simultaneously. It would be possible if the rotational and switching onsets of the different functionalities are distinguishable in this example.

7 Thermal and electronic contributions to unidirectional rotation of molecule-rotors

The directed motion of single molecules on a surface is essential for producing useful work at the nanoscale. In this Chapter, aiming at exploring the limits of the micro-reversibility principle, a single molecule-rotor has been chosen in order to investigate its unidirectional rotation. Analysis of the interplay between thermal and inelastic tunneling excitations has been performed.

7.1 The Maxwell's demon

In order to produce useful work, one has to always “pay” for the energy to reduce the entropy of a given system. Formally, the second law of thermodynamics states that the entropy of an isolated system tends to increase, leading to an equilibrium distribution statistically with maximum entropy. To achieve any distribution other than the thermodynamic equilibrium, work must be done on the system.

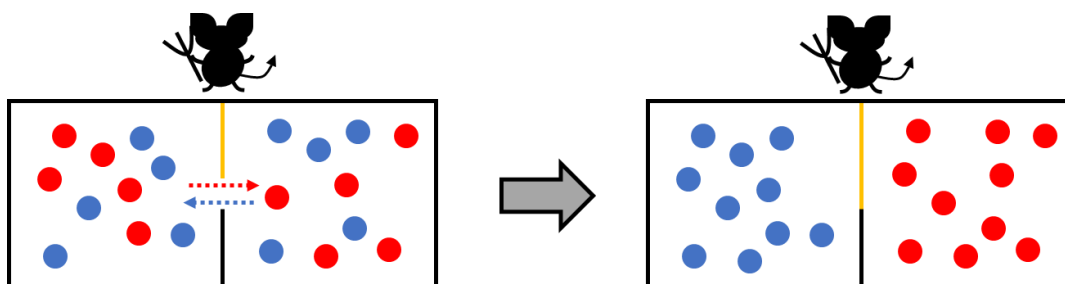


Figure 52. Maxwell's demon. Blue dots represent cold/slow molecules, and the red dots represent hot/fast molecules. Note the velocity of molecules can only be measured statistically but the demon can “sort” them individually similar to a quantum machine.

J. C. Maxwell envisioned that there are two boxes of molecules where they are at the same temperature ($T_1 = T_2$) according to his thought experiment [109]. (The famous *Maxwell's Demon* was first revealed by Maxwell in a letter to P. G. Tait in 1867, and this idea was later published in 1871 in *Theory of Heat*. The term “*demon*” was coined by Lord Kelvin in 1874.) The two boxes have a hole between them (Figure 52), and hence,

the molecules can travel in between. At the hole sits a demon (“an intelligent gatekeeper”) who can open and close the hole (orange gate). The demon can artificially sort and allow the fast (hot) molecules to go from the left box to the right, and keep the slow (cold) ones in the left box, relative to the average velocity. As a result, the right side eventually becomes hot and the left one is cold. This means that with the presence of the demon, even if the two boxes are at the thermal equilibrium, the system can still produce work, violating the second law of thermodynamics.

7.2 The Szilárd’s engine

Maxwell’s idea was quantified by L. Szilárd in 1929 [110], suggesting a quantitative relationship between the information used by the demon and the work from a single thermal reservoir. In Szilárd’s engine (Figure 53: left to right), there is a molecule inside a box in thermal equilibrium at a finite temperature T . A demon can determine the position of the molecule (left or right), and accordingly insert a partition together with a weight tied to the corresponding direction (left or right). The partition equally distributes the volume of the box V_0 into $V_0/2$ before extracting any work. This partition is allowed to expand into the full volume V_0 , spontaneously lifting the weight against gravity, hence extracting useful work. The partition is eventually removed again and the molecule inside is free to diffuse, this cycle can then repeat.

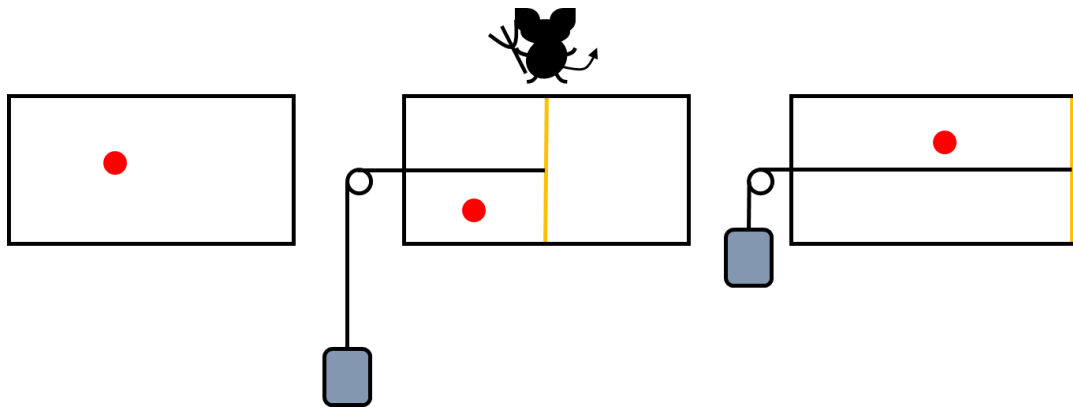


Figure 53. Szilárd’s engine. Red dot represents a molecule which can freely diffuse inside the box at a finite temperature T .

By doing this, in other words, at the beginning of each cycle, the molecule has equal probabilities on either left or right, and hence, the measurement can produce one bit of information from each cycle. As a result, the maximum of the average extracted work per cycle reaches the fundamental value of $k_B T \ln 2$, where k_B is the Boltzmann constant. (This fundamental value was proposed by R. Landauer as the theoretical limit of energy consumption of computation [111]). Such a direct conversion of heat

into work violates the second law of thermodynamics, since both the measurement and the feedback of the demon are done without generating extra entropy.

7.3 The Feynman's ratchet-and-pawl device

To further realize this idea in a mechanical device in the direction of thermal fluctuation, R. P. Feynman in his lecture (Chapter 46 of *The Feynman Lectures on Physics*) discussed the idea of a Brownian motor based on a ratchet-and-pawl device [112] inspired by the discussion of M. Smoluchowski [113] (Figure 54).

Ratchet-and-pawl machine is a mechanical device that permits continuous rotary motion in only one direction while preventing motion in the opposite direction (i.e., the pawl motion is rectified by the asymmetric shape of the ratchet). In its simplest case, the device consists of a ratchet wheel, which is a wheel with asymmetric teeth along its circumference, and a pawl that is a spring-loaded lever to engage with the teeth of the wheel. When the wheel is turned in one direction, the pawl spontaneously engages with the teeth, preventing the wheel from turning backward (i.e., in the forbidden direction).

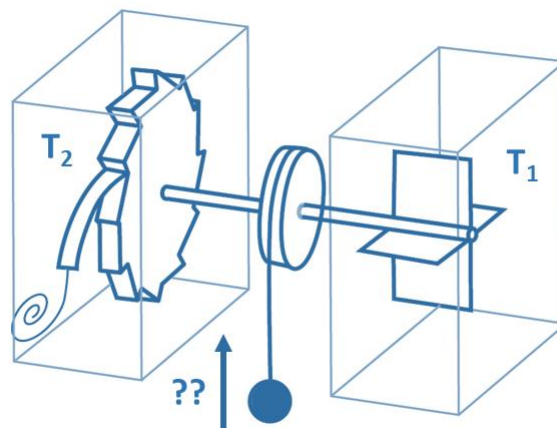


Figure 54. Schematic drawing of Feynman's ratchet and pawl machine [112].

In Feynman's ratchet-and-pawl device (a thought experiment), there are two isolated boxes filled with Brownian particles. One of the boxes consists of the ratchet-and-pawl kept at a definite temperature T_2 , and the other has a windmill with vanes at T_1 . They are connected with an axle, where this system is envisioned to lift a weight against gravity. When $T_1 > T_2$, the vanes attain the energy and the system will go in one direction due to the collisions of particles on the vanes. The asymmetry of the teeth of the ratchet cog was intended to drive directional movement. However, according to

Feynman, even if $T_1 = T_2$, the rectification of such thermal fluctuation/noise could be harnessed to perform work, violating the second law of thermodynamics.

While they are clearly ideas that violate the second law of thermodynamics, theoretical and experimental efforts on exploring the limit of the *law* have been spent in the past 150 years (which was in between the period of, e.g., the renowned works from Maxwell who unified the electromagnetic forces, and the paradigm shift of quantum mechanics). During this ongoing journey, studies instead of finding/failed to find the “demon” have boosted many fascinating theoretical and experimental studies of interesting phenomena, e.g., the connection between information and entropy [114], energy and information flow in biological systems [115], and quantum heat engines [116].

Since the nature of the demon who can intelligently sort or determine the position of individual molecules to reduce entropy involves quantum measurement phenomena from the view of the statistical nature of thermodynamics [109], single molecule machines (i.e., the mechanics of one molecule) that involve quantum processes may provide new perspectives in this context. In this work, we aim at exploring the limit of the *micro-reversibility principle* by manipulating a molecule-rotor that exhibits unidirectional rotation by STM with an external thermal source. This chapter will discuss a detailed study of the contributions of thermal and tunneling electronic excitations for unidirectional rotation.

7.4 Micro-reversibility principle

Unidirectional rotation represents one of the major challenges of single molecule machines since it leads to the prospect of obtaining a net production of useful mechanical work [117]. Pure thermal excitation cannot induce directed motion in its electronic ground state without breaking the micro-reversibility principle or “*the principle of microscopic reversibility*” [118]. It states that when the system is in its thermal equilibrium, the rates of all microscopic processes that can occur in both forward and reverse directions must be equal, and hence no directed motion. According to the energy equipartition theorem [119], thermal energy is equally distributed to all mechanical degrees of freedom of the rotor on the surface, leading to random movement. In a schematic view (Figure 55) in terms of potential energy as a function of reaction coordinate, the potential energy profile is harmonic according to the micro-reversibility principle, with the possibility that the energies of the local minima can be different.

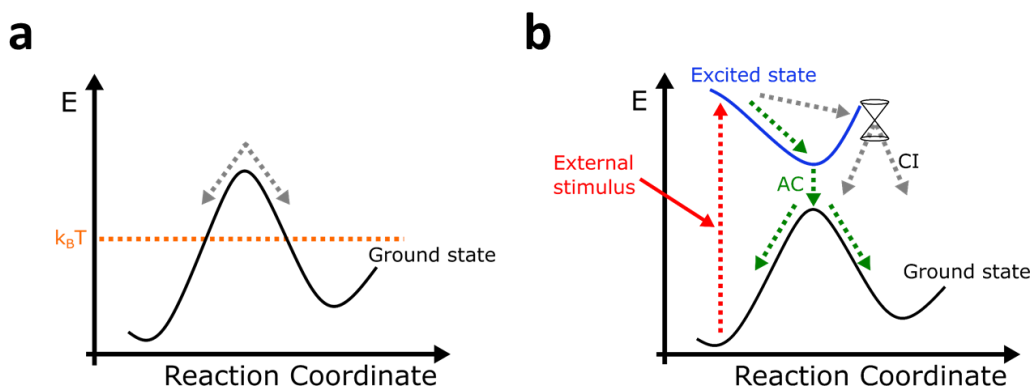


Figure 55. Schematic potential energy profiles in the simplest pictures. (a) Random rotation due to thermal excitation ($k_B T$). (b) A specific case of the Feringa motor. Ground and the lowest singlet excited state along the minimum energy path. External stimulus excites the molecule from the ground state to the excited state. Position of the conical intersection is shown, leading to unidirectional rotation. AC: Avoided crossing. CI: Conical intersection.

Aiming at exploring the limits of the micro-reversibility principle and the conditions to induce a directed motion of a single molecule as a quantum mechanical matter, the electronic excited states of the molecule should be included, a possibility that is absent in a classical mechanical rotor. A classical ratchet-and-pawl model is not sufficient to understand the processes behind it. In other words, it is important to note that only e.g., vibrational modes (only at the ground state) cannot address the full process of unidirectional rotation. As an analogy, the excitation of vibrational modes of a molecule acts similarly to the thermal excitation. In other words, a “demon” is required to achieve unidirectional rotation only with thermal fluctuation.

A well-studied system from B. L. Feringa may shed light on the dynamics of the unidirectional rotation of a molecular motor (“Feringa’s motor”) studied in solution chemistry [120]. It is a light-driven motor derived from chiral overcrowded alkenes, which can utilize repeatable cycles of photochemical and thermal rearrangement for the directed motion. From a theoretical study [121], the authors have suggested the possible dynamics behind the photoisomerization of the Feringa’s motor by analyzing experimental data, quantum chemistry, and molecular dynamics. Computation of potential energy surfaces (PESs) of the ground and excited states has been investigated, where it plays a crucial role to explain molecular dynamics and chemical processes based on Born–Oppenheimer approximation. From their results, the excited state and the subsequent relaxation process via a funnel in the hyperspace, namely conical intersection, to the next local energy minimum according to the reaction coordinate should be included. For conical intersection [122], it happens when two Born–Oppenheimer potential energy surfaces (the ground and first excited states) intersect forming a double cone (as a consequence of the breakdown of the Born–

Oppenheimer separation), where in these special locations, the system can funnel down from one potential energy surface to another by the adiabatic process. Currently, it is widely accepted that it plays a crucial role in nonadiabatic processes, e.g., physiological vision and light harvesting. The conical intersection point seems to explain the funnels for highly efficient nonadiabatic relaxation that is a sub-picosecond process if the molecular system is only described in terms of nonadiabatic coupling in the avoided crossing region which predicts a much longer time scale [123]. It also explains the unidirectional rotation of the Feringa's motor. The dynamics of the Feringa's motor may aid the understanding of the unidirectional rotation of a single molecule rotor adsorbed on the surface triggered by STM tip voltage pulses.

Here, Figure 55a and b are simplified pictures of the potential energy profiles that allow the description of the simplest system. As an example, the schematic Figure 55a shows two local minima at the ground state together with a possible transition between stable and metastable stations. The presence of thermal excitation ($k_B T$) leads to random rotation because it "fills up" the potential energy profile at a certain T at the ground state. In other words, rapid interconversions (grey arrows) between the two local minima (e.g., rotational stations) take place where the thermal contribution makes them inseparable. Therefore, unidirectional rotation is not possible in this case.

On the other hand, taking the Feringa's motor as an example, when an external stimulus is applied to the molecules, they can be excited electronically from the ground to the excited state at a given energy (i.e., a few electron Volts), undergoing photoisomerization. In this case (Figure 55b), instead of channeling the avoided crossing region (green arrows; a "leakage" channel for the electron flows from higher down to the lower potential energy profiles), the system undergoes an electronic quenching to the next local minimum via conical intersection on the right (grey arrows), leading to unidirectional rotation. To achieve this, an asymmetry geometry of the excited state profile is required, in which such asymmetry is the contribution (i.e., not the only contribution) of the asymmetric structure from the Feringa-motor. Nonetheless, one should note that the processes involving tunneling electrons and adsorption on metal surfaces are different from photochemistry in solution. It is possible that the conical intersection may not be required in the case of tunnelling electrons excitation if the local energy minimum of the excited state has an asymmetric geometry, relative to the local maximum of the ground state profile. In addition, the real-time structural evolution and how to tune the excited state potential energy surface to optimize quantum yield are not well-understood yet.

In short, aiming at going beyond the second *law*, tuning of potential energy profiles/surfaces at both the ground state and excited state seems to be a possible way by, for example, designing a molecule-surface system with asymmetry at both ground and excited states involving the conical intersection with external excitation. From the

understanding of Feringa's motor, one experimental accessible way of a molecule-surface system with external stimulus for directed motion is to break the symmetry of the potential energy profiles projecting from the structures.

7.5 The rotor unit

DMNI-P molecule has been chosen for the following temperature dependent measurement due to its ability of unidirectional rotation chemisorbed at the Au-O bond at low coverage as discussed in Chapter 6. In addition, chemisorbed molecule is an ideal system for temperature dependent measurement because of its stability, where physisorbed molecule (Nanocar) can already diffuse across the surface when reaching $T > 10$ K, observed from the mixture of DMNI-P rotors and nanocars experiments. In the STM junction, the structural asymmetry is carried internally by the rotor itself. Symmetry breaking has been considered as a contributor for unidirectional rotation/directed motion because this can project the asymmetry onto the potential energy curve. At the temperature of 5 K, the isolated DMNI-P molecules reliably rotate in one direction by bias voltage pulses of $V \geq 350$ mV applied for a few seconds (Chapter 6).

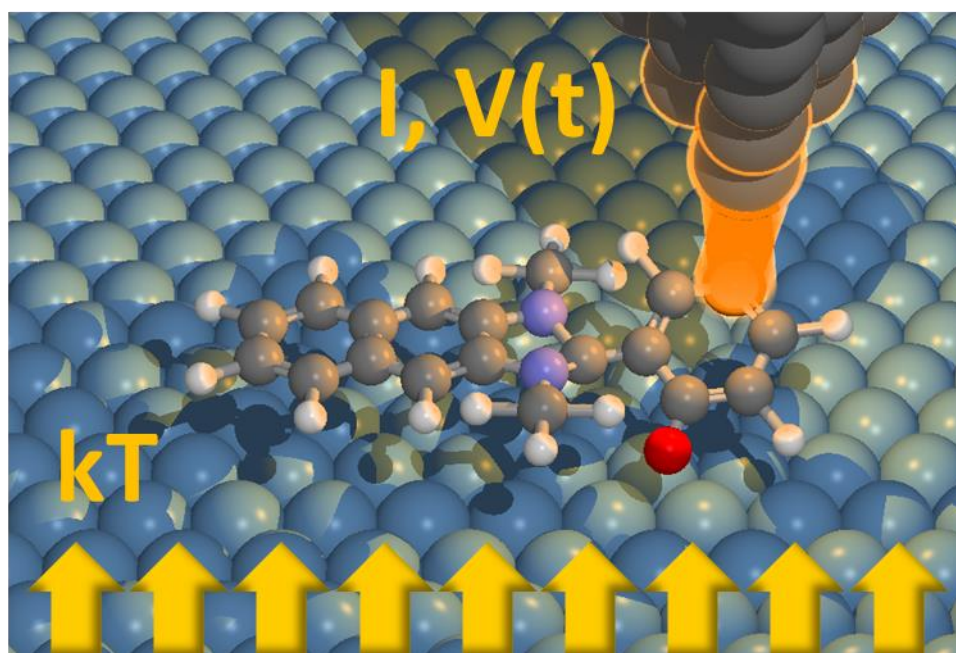


Figure 56. Schematic diagram of DMNI-P rotor chemisorbed on Au(111). The experimental work focuses on the interplay between inelastic tunneling ($I, V(t)$) and thermal excitations (kT).

7.6 Experimental conditions for thermal excitation

The experimental procedure for the specific temperature dependent measurement is described as follows:

After sublimation of DMNI-P molecules on the Au(111) surface held at room temperature, the sample was immediately cooled down to low temperature according to the standard preparation procedure. A Zener diode (mounted on the scanner) has been employed where the temperature can be changed stepwise by altering the electronic parameters (I , V). At each desired temperature step, the system was stabilized for > 1 hour ($T_{\text{error}} = \pm 0.5$ K including fine-tuning manually) to obtain a homogenous temperature in the whole STM head (including the STM tip and the sample).

7.7 Thermal excitation

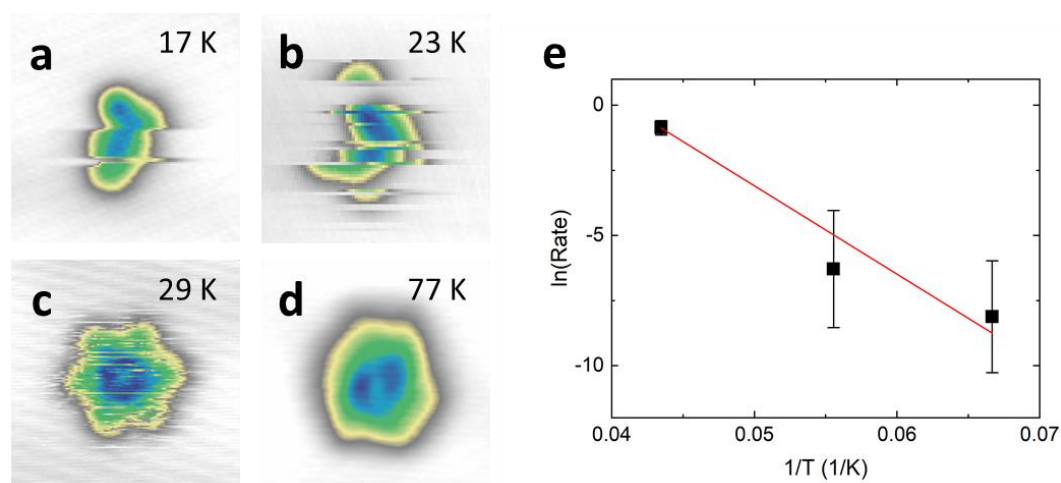


Figure 57. Thermal excitation of DMNI-P rotation. (a) The molecule starts rotating at $T = 17$ K, (b) while it becomes faster at 23 K. (c) At 29 K, it appears as a hexagonal shape since it rotates faster than the scanning of the STM image. (d) The rotor rotates at $T = 77$ K. STM images ($4 \text{ nm} \times 4 \text{ nm}$) were taken under (a) $I = 5 \text{ pA}$, $V = 100 \text{ mV}$, (b) $I = 5 \text{ pA}$, $V = 200 \text{ mV}$, (c) $I = 5 \text{ pA}$, $V = 10 \text{ mV}$, scanning speed: 17.3 s/image , and (d) $I = 28 \text{ pA}$, $V = 500 \text{ mV}$. (e) The thermally excited rotation frequency shows an Arrhenius behaviour, resulting $E_{\text{ex}} = (29.2 \pm 4.7) \text{ meV}$; $R_0 = 10^{6.03 \pm 1.06} \text{ Hz}$, obtained from the linear fit over the plot of $\ln(\text{rate})$ over $1/T$.

The rotation behaviour excited thermally is first tackled. Minimum stable imaging parameters ($I = 5 \text{ pA}$ and $V = 10 \text{ mV}$) were used to prevent any unintended rotation during the scanning process. At these conditions, the effects of inelastic tunneling, which involves electronic excited states and strong tip interactions (e.g., electric field effect) are negligible. By progressively increasing the surface temperature in the steps

of 0.5 – 1 K, the minimum required temperature can then be determined. Sufficient relaxation time was provided in order to reach thermal equilibrium of the STM (i.e., to avoid piezo-drift and stabilize temperature measurement).

The first rotary motion was detected at $T = 12$ K after waiting 17 hours repeating STM images every 15 minutes. When increasing T further, more frequent random rotation can be observed as shown in Figure 57a – c for 17 K, 23 K, and 29 K, respectively. Note that at 29 K, the STM image formed by horizontal lines (forward + backward scan) shows a hexagonal shape, depicting that the rotor visits the six stable stations (i.e., local minima) randomly at a very fast rate. By plotting $\ln(\text{rate})$ over $1/T$, an Arrhenius behavior can be found. The linear fit shows the excitation energy $E_{\text{ex}} = (29.2 \pm 4.7)$ meV. The result is similar to the previous study of DMBI-P (a shorter rotor) estimated with $E_{\text{ex}} = (5 \pm 2)$ meV. This can be explained by the increasing van der Waals interactions with an elongated six-membered ring on the Au(111) surface. In addition, it was observed that the chemisorbed rotor can survive at least 77 K (Figure 57d).

In agreement with the micro-reversibility principle, pure thermal excitation does not yield unidirectional rotation. In other words, such structural asymmetry from this prochiral molecule is insufficient to bring the energy profile to the excited states.

7.8 Interplay between thermal and inelastic electronic excitation

The question now is: can both thermal heating and electronic excitation contribute together to induce unidirectional rotation? If so, to what extent can we control it? We therefore repeated the above rotation experiments by applying STM voltage pulses ($50 \text{ mV} \leq V \leq 500 \text{ mV}$) and increasing progressively the temperatures from $5 \text{ K} < T \leq 17 \text{ K}$.

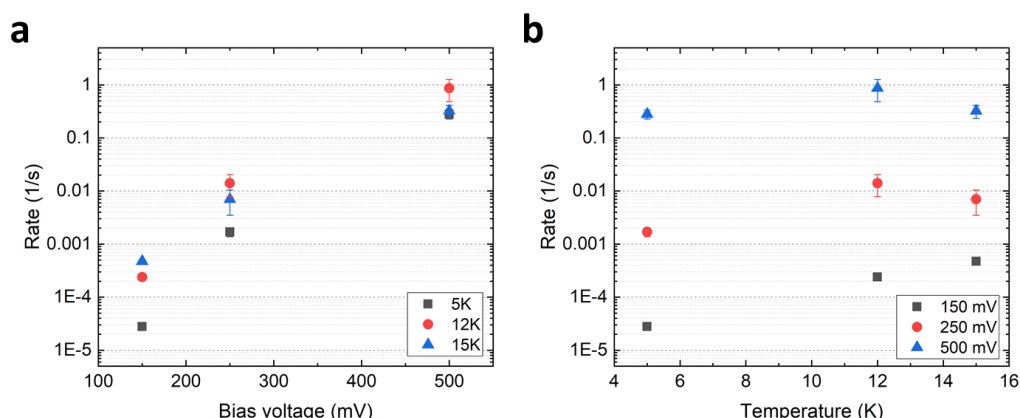


Figure 58. (a) Rate over bias voltage at different fixed temperatures. (b) Rate over temperature at different fixed bias voltages.

In these conditions, a faster rate of unidirectional rotation for $T > 5$ K has been observed with voltage pulses. In Figure 58a, the rate of directed rotation (1/response time) depending on different bias voltages is plotted for three fixed temperatures (all data point measured at $I = 700$ pA). Increasing the temperature indeed leads to a faster rate, while this effect diminishes by increasing the voltages and eventually becomes weaker at $V > 500$ mV. This situation becomes clearer when converting the plot (Figure 58a) into the function of rate over temperature for three different fixed voltages (Figure 58b). The results indicate that at this energy, the C-H vibrational mode ($V > 370$ mV) is excited, and hence the inelastic electronic excitation is now again the main energy entry port for the directed rotation which overcomes thermal contribution at the STM junction.

From Figure 59, the resulting yields at 12 K and 15 K ($I = 700$ pA) show similar behavior (three regions) when compared to the curve at 5 K. In other words, the two main vibrational modes as the onsets excited by the inelastic tunneling electrons contribute to the unidirectional rotation, while the thermal energy lowers the overall energy barriers for triggering any rotary motion (including non-directed one). However, one should note that the excited vibrational modes are not sufficient to describe how unidirectional motion begins, even by an intrinsic chiral molecular structure. Triggering vibrational modes intramolecularly acts similarly to thermal excitation, where this will lead to random rotation according to the micro-reversibility principle.

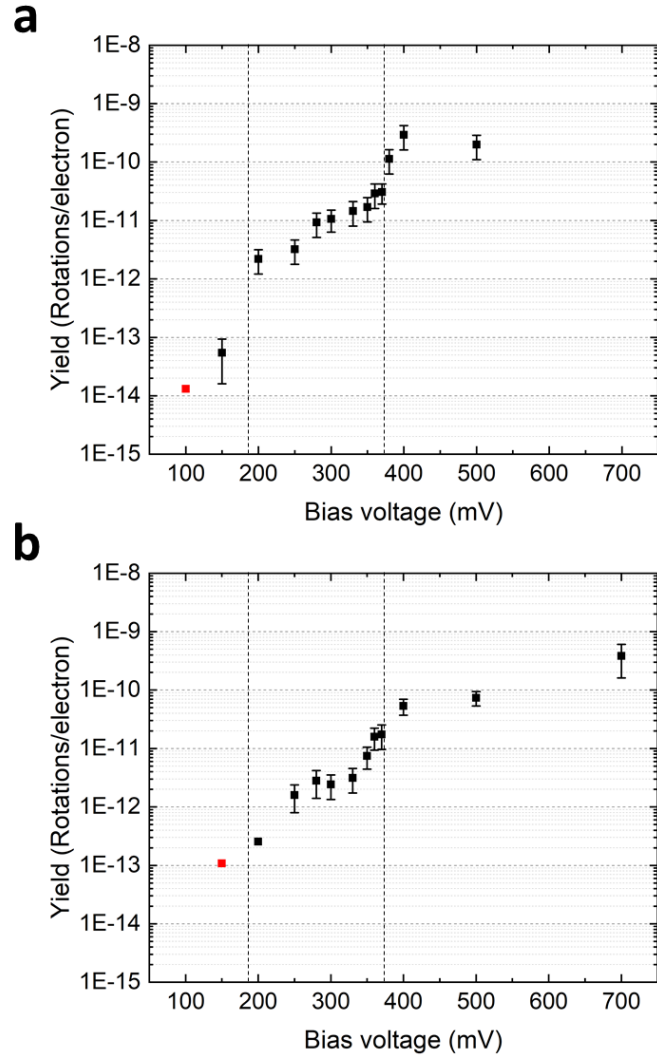


Figure 59. Plots of yield (rotations/electron) over bias voltage for (a) 12 K, and (b) 15 K, respectively. The red points represent the lack of data population ($n = 1$) due to the limitation of long excitation time. Voltage pulses were applied at $I = 700$ pA, $V = 100$ mV – 700 mV.

To address that, the combined thermal and electronic measurements have been extended into the experimental available range of temperatures, and summarized in Figure 60, including the results from Chapter 6 at 5 K. In the Y, V plot, it is a schematic curve obtained from the fit of Figure 49c, revealing the two main vibrational onsets (Figure 48). In the T, V plane, the blue dots correspond to observed unidirectional rotation induced by STM voltage pulses, and the orange dots to random rotations. For the dotted lines, they divide the plot into the three regions from the fitted yield for the inelastic electronic excitation at $T = 5$ K (Figure 49): the excitation energy threshold of soft mechanical and the C-H stretch modes at 165 and 370 meV, respectively.

- (1) Grey area: No observable rotation can be found in the grey area due to the extremely low temperature and bias voltages. These conditions are probably not sufficient to create a minimum energy path on the ground state of the potential energy surface.
- (2) Light blue area: For $5\text{ K} < T < 12\text{ K}$, STM voltage pulses induce unidirectional rotation from ($150\text{ mV} < V < 700\text{ mV}$) with $d > 0.99$ as shown in Chapter 6. As discussed before, the inelastic tunneling electrons contribute to the vibrational energy onset. The chirality of the molecule and its charge separation in the electric field of the STM junction contributes to the asymmetry of the excited state profile/surface with respect to the ground state, and therefore contribute to the observed unidirectional motion.
- (3) Yellow area: Both blue and orange dots are present in this area, i.e., both unidirectional rotation and random-direction rotations are possible. While reducing the pulse voltage to near 0 V , the molecules rotate randomly for $12\text{ K} < T < 20\text{ K}$. In the same range of temperature, voltage pulses with low voltages at $50\text{ mV} \leq V \leq 250\text{ mV}$ can induce unidirectional rotation with an enhancement of rotational rate (Figure 58). In this narrow range (T, V), the inelastic tunneling effect is weak with a low probability of exciting low-energy vibrational modes at 165 meV and below. Given that the tunneling current is described by a quantum mixing of the ground and excited virtual electronic configuration that happens at each electron transfer event. Therefore, at each electron transfer event, part of the thermal energy coming from the gold surface can be redistributed intramolecularly and trigger a dynamical path on the excited state potential energy surface. This means that the rotational barrier on the excited state can be overcome, and a one-step of unidirectional rotation happens similarly as discussed above for inelastic effects. In other words, each electron transfer event “projects” part of the thermal energy captured by the molecule-rotor on the excited state, practically sharing it between ground and excited states.
- (4) Orange area: for $T > 17\text{ K}$, regardless of the applied voltage pulses ($0\text{ V} \leq V \leq 700\text{ mV}$), the random rotary motion (e.g., visiting all six stable stations randomly at 29 K) cannot be stopped, obeying the micro-reversibility principle. The surface temperature is too large for benefitting from the topology of the S_1 potential energy profile relative to the ground state for a one-way rotation.

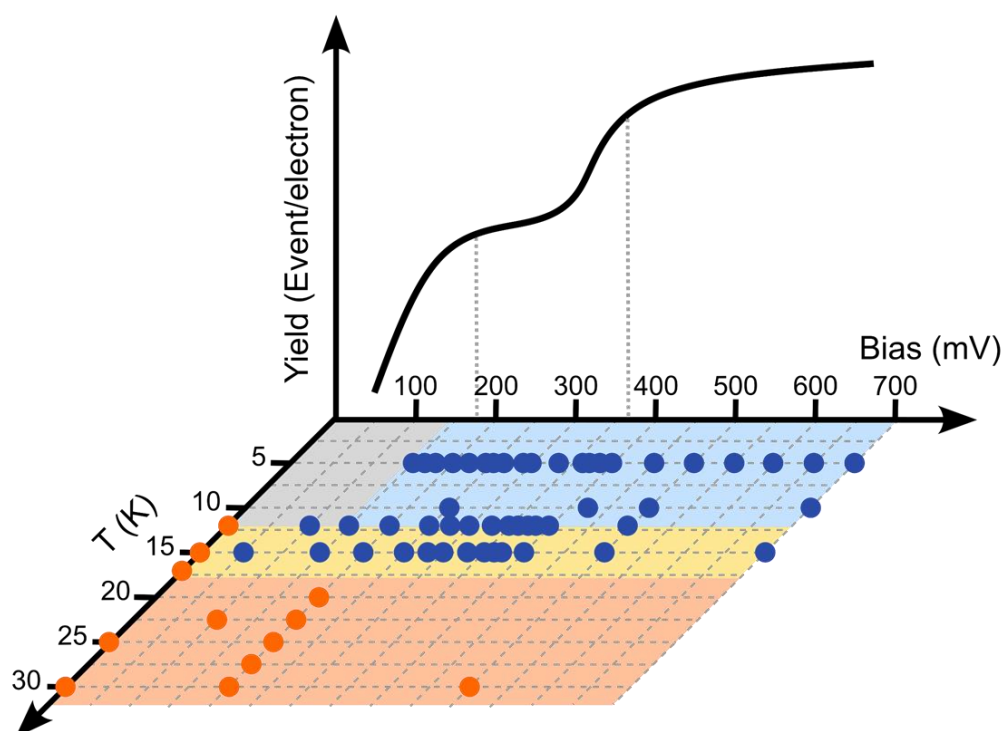


Figure 60. Summary of combining thermal and electronic excitations. Plot of yield over bias voltage and temperatures for rotation. The orange dots indicate the conditions for random rotation, the blue ones the unidirectional rotations.

7.9 Summary

This chapter examines the rotation of DMNI-P molecule-rotors on the Au(111) surface due to thermal and tunneling electronic excitations. The study aims to investigate the relationship between these two types of excitations. In agreement with the micro-reversibility principle, a pure thermal excitation induces random rotation for $T \geq 15$ K with an experimentally determined energy barrier of $E_{\text{ex}} = (29 \pm 5)$ meV. On the other hand, unidirectional rotation ($d > 0.99$) can be induced with the presence of tunneling current in the STM junction. Two vibrational modes as onset energies are quantitatively identified as C-H stretch mode and also the low-energy modes ($V < 370$ mV). While the two distinguishable areas for thermal and tunneling electronic excitations can be clearly identified, the overlapping area (T, V) shows a narrow range where the thermal excitation enhances the rate for unidirectional rotation of the rotor under the STM tip.

Computational analysis of PESs is a possible way to understand the underlying processes. However, it is very challenging and probably not possible to compute quantitatively the multi-dimensional potential energy surfaces especially for molecule

on a surface involving the ground and excited states even with the state-of-the-art methods. In addition, the contributions (and to what extent) from individual excitation “contributors” cannot be easily addressed one by one experimentally. There is so far no unified or general physical mechanism to predict and explain the motion of a given molecule actuated by the STM tip. So far, no general selective rules can predict which molecule-surface system can rotate in one direction.

On the other hand, the findings of the interplay between thermal and electronic excitations shed light on the design of quantum motor on surface and open a possible new perspective on energy storage. This also provides experimental evidence on the possibility to pump surface heat energy into a single molecule. In terms of quantum engineering, this opens fascinating perspectives in the direction of mono-thermal motors. By using only thermal excitation, a “demon” is required for unidirectional rotation. One suggestion would be to explore the possibility to design a molecule-surface system with a “ratchet-like” potential energy profile at the ground state, violating the micro-reversibility principle.

8 Summary and outlook

In summary, this thesis studies the motion of single molecule machines adsorbed on the Au(111) surface, where three different classes of single molecules have been examined in different aspects by means of STM manipulation. With the rational designs of five-tooth molecule-gears in Chapter 5, they allow the study of the transmission of stable rotation between the PPCP-based molecules by STM lateral manipulation. Comparison of anchoring strategies and markers for STM visualization shed light on the complex processes in the tip-molecule-surface tunneling junction.

For single molecule machines driven by STM voltages pulses (Chapter 6 and 7), molecular coverage-related selectivity reveals two distinct functionalities depending on the nature of chemisorption or physisorption of DMNI-P molecules (Chapter 6). The chemisorbed rotors exhibit unidirectional rotation, while the physisorbed nanocars show controllable translation. The co-existence of two functionalities allows the direct comparison of the rotary and translational dynamics which demonstrates different threshold energies for the rotors and nanocars. The study on the unidirectional rotation of a single-molecule rotor DMNI-P in Chapter 7 aims at exploring the limit of the micro-reversibility principle and the contributions from thermal and tunneling electronic excitations. The results show two well-identified regimes, where the thermal excitation from the gold surface can induce random rotation and the tunneling electronic excitation in the STM junction can trigger unidirectional rotation over a long timeframe. The narrow overlapping regimes between both excitations show a cooperative effect where the thermal excitation enhances the rate of directed rotation. The results have opened a new perspective of realizing a quantum heat motor.

To build a nano-device, mechanical (including active and passive) and/or electronic components are the basic requirements. Although integrating different components into a device is an almost clear possible direction, one should not neglect the possibility given by many more parameters, e.g., the collective effect (Chapter 5), adsorption geometries (Chapter 6) and variable surface temperature (Chapter 7).

Taking collective effect as an example, while transmission of rotation has been demonstrated in Chapter 5, cooperative effect of switching (on/off) between neighboring single porphycene molecules has been demonstrated earlier [124]. A more recent example [125] has shown that single diamagnetic H₂ phthalocyanine molecules adsorbed on a superconducting Pb(100) surface exhibit tunable magnetic moment by arranging the neighbors. If one can manipulate the (mechanical) configuration of molecule, then transmit controlled motion to the interlocked neighbor with careful arrangement, and eventually artificially tune the properties of the whole

molecular assembly (or device), it may open a new direction on tunable spintronic devices at single molecule level.

On the other hand, researchers should face directly the challenges of finding the Maxwell's demon. Quantum processes may provide new perspectives which are absent in the macroscopic scale, aiming at producing useful work with the help of the "demon". The results from Chapter 7 may shed light on the new designs of quantum motors, most likely in the direction of tuning the energy barrier and the projected asymmetry in the potential energy curves or PESs from the molecule. All in all, the works on designing novel single molecule machines and understanding the fundamental driving forces will be continued, where "*there's plenty of room at the bottom.*" [1]

9 Appendix

9.1 On surface synthesis: Cyano-vinylene linked chains via Knoevenagel Condensation

On-surface synthesis [126] is a newly developing field of research that makes use of well-defined solid surfaces as confinement templates to initiate chemical reactions and to create organic materials and nanostructures in an ultra-clean environment. The extension of on-surface synthesis to the formation of covalent linkages or networks is presently on the focus of scientific research and represents a unique challenging strategy to obtain atomically pure single-layer one-dimensional to two-dimensional conjugated polymers with designed properties. By combining on-surface synthesis with the high spatial resolution of scanning tunneling microscopy (STM) and spectroscopy (STS) at low temperature, the atomically precise structure and electronic properties can be investigated. Parts of the text and figures are reproduced from ref. [127] with permission of Chemistry - A European Journal.

9.1.1 Methods

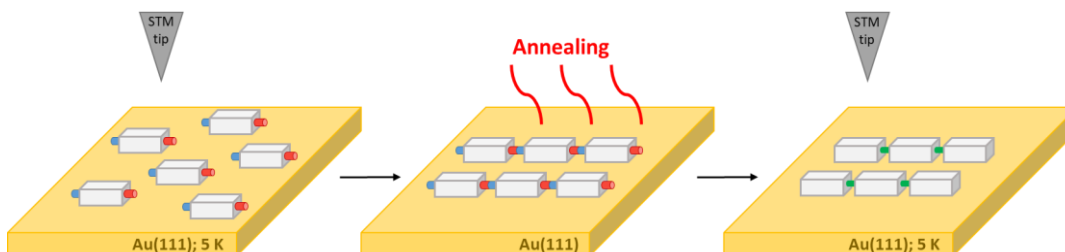


Figure A 1. Schematic drawing of the general experimental procedure on activating chemical reaction thermally on surface investigated by low-temperature STM.

In general, the experimental methods for low-temperature STM investigation can be described in three main steps: (1) the molecular precursors are deposited by sublimation on the surface. Then after cooling the sample to 5 K, imaging and characterization of the precursors can be performed. (2) The sample is then taken out of the cryostat and brought to the preparation chamber for activating the chemical reaction on surface. Different approaches of the annealing process have been reported, e.g., slow dosing on a hot surface [128] (by combining step 1 and 2). The time and temperature are the basic parameters in this process. (3) After annealing, the sample is brought back to the cryostat for further STM investigation.

In the following, the formation of CN-substituted phenylene vinylene chains on the Au(111) surface will be presented. The chain formation is driven by a thermally induced Knoevenagel polycondensation (Figure A 1). The precursor 4-formyl(4,4''-terphenyl)-4''-methylenenitrile (1) and the target conjugated oligo-phenylenevinylene (3) are investigated.

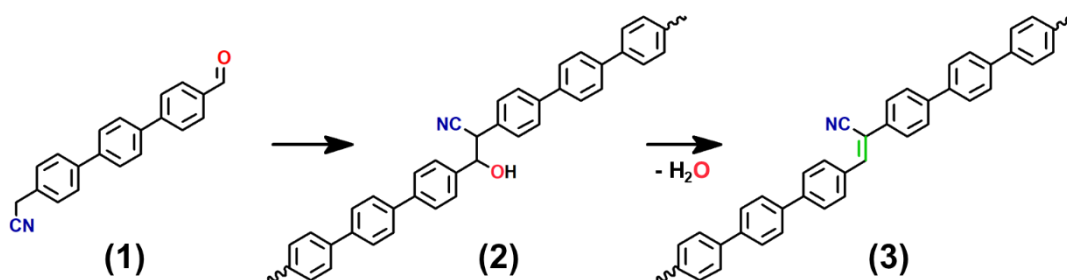


Figure A 2. Proposed reaction pathway of CN-substituted phenylene vinylene chains on surface under UHV conditions.

9.1.2 Deposition and activation of reactions on Au(111) surface

Precursor molecules (1) were deposited thermally ($T_{\text{evap}} = 170^{\circ}\text{C}$) on the clean Au(111) surface kept at room temperature under UHV conditions. STM experiments were performed after cooling the sample to $T = 5\text{ K}$. After deposition, self-assembled and densely packed monolayer islands of the precursors can be observed in the STM images (Figure A 3). The molecules can be clearly identified as the linear features oriented in parallel. Different spacing between the molecules is observed possibly due to both the mismatch to the Au(111) lattice and the different intermolecular interactions (i.e., van der Waals interactions) at the methylene nitrile and aldehyde ends.

To induce the formation of molecular chains, we annealed stepwise the adsorbed precursors. After each annealing step, the sample was cooled down to $T = 5\text{ K}$ and STM images were recorded. The first annealing step at $T = 200^{\circ}\text{C}$ causes partial desorption and molecular diffusion. Figure A 3 shows that the monolayer islands deform into parallel structures, still formed by individual precursors. After annealing at 220°C , the coverage decreases sharply and chains of molecules are visible.

The last annealing step at 240°C causes further desorption of monomers and short chains, with a slight improvement of the average chain's length. At this stage, only the kinks of the Au(111) reconstruction sites are still populated with molecular chains. Furthermore, after annealing at $T \geq 220^{\circ}\text{C}$, further structures probably due to van der Waals or metalorganic bonds with Au adatoms are visible.

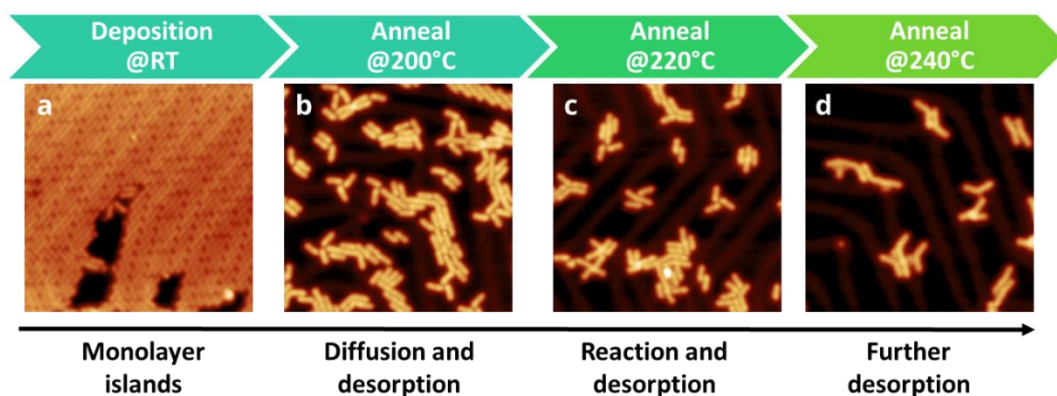


Figure A 3. Overview STM images (23 nm x 23 nm) from stepwise annealing preparations. (a) Formation of monolayer islands after thermal deposition of the precursor (**1**) on the Au(111) surface kept at RT. Stepwise growth of the phenylene vinylene chains after annealing at (b) 200°C, (c) 220°C, and (d) 240°C. STM images are taken in constant current mode under (a) $V = 300$ mV and $I = 3$ pA, (b) $V = 500$ mV and $I = 5$ pA; (c – d) $V = 500$ mV and $I = 10$ pA.

9.1.3 Formation of molecular chains

The proposed thermally induced Knoevenagel condensation following the reaction pathway of Figure A 2 happened on surface after annealing at a temperature between 220°C and 240°C. Following the pathway, the aldehyde and methylene nitrile substituents of the precursor molecules (**1**) could approach each other and react, then form a covalent bond (**2**). Spontaneous dehydration is expected to obtain the chain (**3**) as a final product. The formation of intermediate (**2**) and the elimination of water molecules cannot be imaged by STM, because the annealing step takes place outside the microscope, however suggesting that the thermal energy upon annealing triggers the water desorption and the final reaction step.

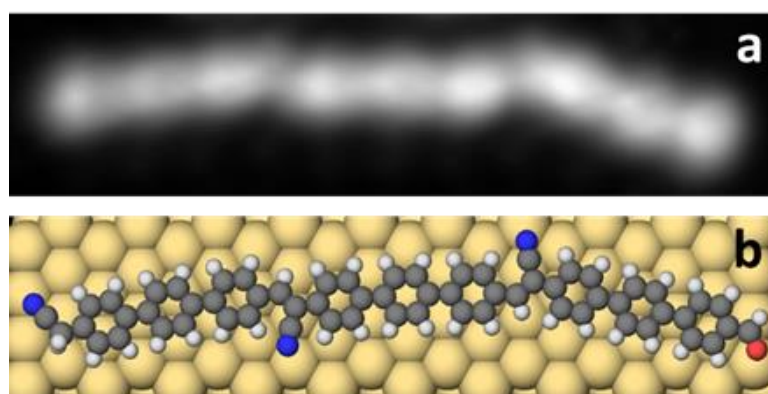


Figure A 4. Structure of a CN-vinylene-linked trimer. (a) Constant height high-resolution STM image (4.6 nm \times 1.1 nm) is taken under $V = 10$ mV. (b) The corresponding calculated adsorption geometry of (a) on Au(111) surface.

Figure A 4a shows a high-resolution STM image of a trimer with three interlinked phenylene vinylene units measured-with a CO-functionalized tip in constant height mode. Small dosing of CO molecules can be deposited on the Au(111) surface at low-temperature, and by using STM manipulation, one can pick up the CO molecule physisorbed on the surface for functionalization. The bright round lobes clearly show the 9 individual phenyl rings. The calculated adsorption geometries (done by D. A. Ryndyk, TU Dresden) confirmed the proposed chain formation (Figure A 4b).

9.2 Testing non-contact atomic force microscopy and obtaining bond-resolved images

Non-contact atomic force microscopy (nc-AFM) is the state-of-the-art technique used to study nano-meter scale forces. The basic principle is that the probe interacts with the van der Waals forces between the atoms or molecules on the surface and the tip of the probe. This interaction causes the probe to oscillate at its natural resonant frequency, which can be detected and used to generate an image of the sample surface. In practical, studies have successfully shown the bond-resolved resolution of nc-AFM [129,130].

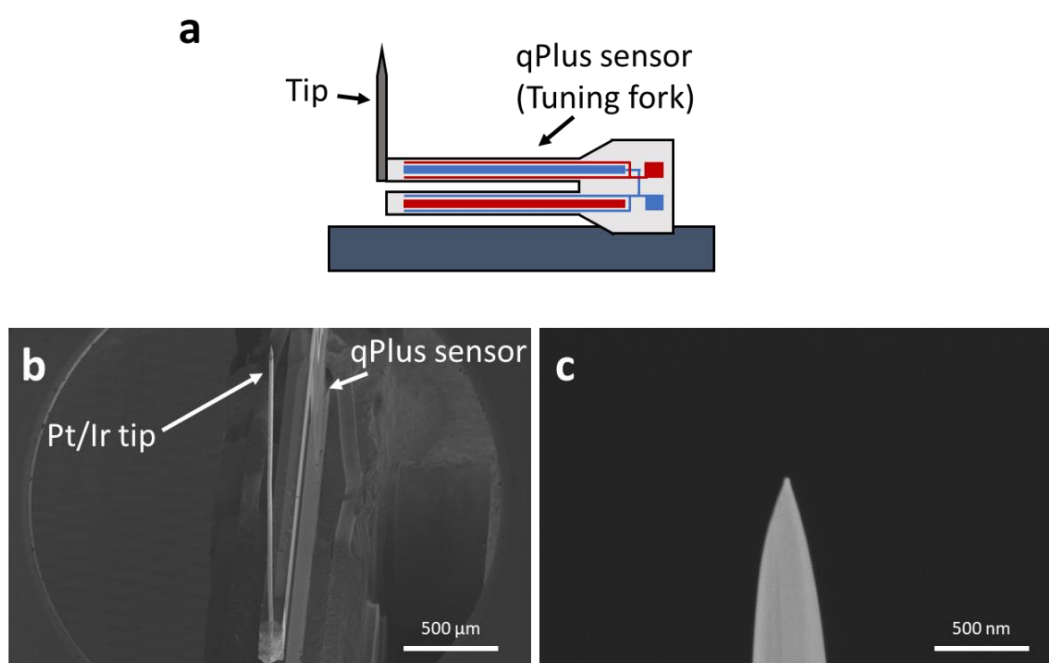


Figure A 5. Scheme of a qPlus sensor. Scanning electron micrographs of (b) the construction of the qPlus sensor and the Pt/Ir tip (scale bar = 500 μm), and (c) the close-up of the Pt/Ir tip after sharpening by focused ion beam (scale bar = 500 nm).

There are several ways to combine the two powerful techniques, nc-AFM and STM, for the study of the adsorbates on the surface. One way is to employ the qPlus sensor [131]. The qPlus sensor consists of a small quartz tuning fork with a sharp tip attached to one end (Figure A 5a – b). The tuning fork is made to vibrate at a specific resonant frequency by applying an alternating current to it. When the tip of the sensor is brought close to a surface, the interaction between the tip and the surface causes frequency changes of the vibration of the tuning fork. By measuring the changes of the frequency (hence generating contrast), images can be generated line-by-line in the real space. The sensor typically has a high stiffness of 1800 N/m.

In 2022, we tested the nc-AFM in Barkhausen Bau, TU Dresden. The tip (attached with the qPlus sensor) was firstly etched chemically. Then, the tip was sharpened by employing focused ion beam technique (done by A. Tahn, TU Dresden). The electron micrograph (Figure A 5c) shows the condition of the tip after the sharpening procedure (imaged by A. Tahn).

By replacing the normal STM tip with the qPlus sensor in the UHV chamber, we tested the resonant frequency ($f_{\text{center}} = 26866.0449 \text{ Hz}$) and Q factor = 2928.1 as shown in Figure A 6a. Additional challenges for acquiring images were expected because of the additional side peaks on the shoulder of the resonance (imperfect tip shape). After several optimizations, we successfully obtained the first image of an organic molecule adsorbed on the Au(111) surface (Figure A 6b) with bond-resolved resolution (CO-terminated tip).

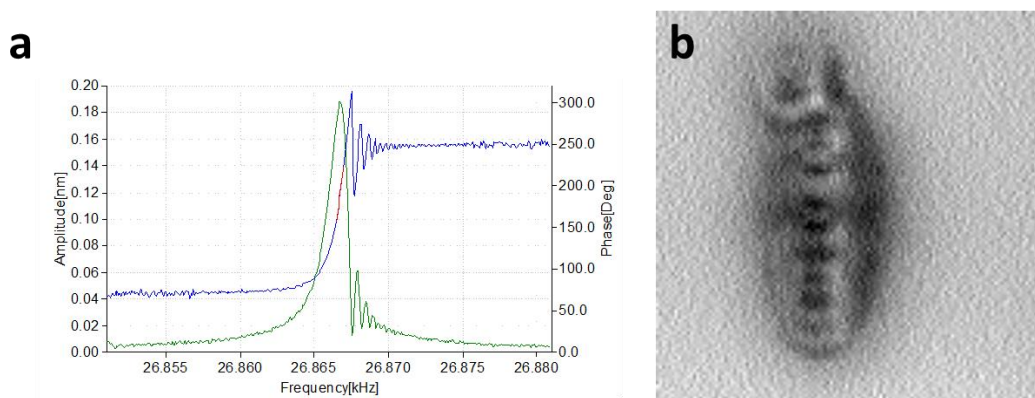


Figure A 6. (a) Frequency sweep for identifying the resonant frequency (f_{center}), PLL-phase and q-factor. (b) First bond-resolved image (raw image: $3 \text{ nm} \times 3 \text{ nm}$) of an organic molecule in the laboratory.

10 Bibliography

- [1] R. P. Feynman, Resonance **16**, 890 (2011).
- [2] C. D. Bruzewicz, J. Chiaverini, R. McConnell, and J. M. Sage, Appl. Phys. Rev. **6** (2019).
- [3] C. J. Bustamante, Y. R. Chemla, S. Liu, and M. D. Wang, Nat Rev Methods Primers **1**, 25 (2021).
- [4] R. Sarkar and V. V. Rybenkov, Front. Phys. **4** (2016).
- [5] D. M. Eigler and E. K. Schweizer, Nature **344**, 524 (1990).
- [6] P. Lussis, T. Svaldo-Lanero, A. Bertocco, C.-A. Fustin, D. A. Leigh, and A.-S. Duwez, Nat. Nanotechnol. **6**, 553 (2011).
- [7] G. J. Simpson, V. García-López, A. Daniel Boese, J. M. Tour, and L. Grill, Nat. Commun. **10**, 4631 (2019).
- [8] U. G. E. Perera *et al.*, Nat. Nanotechnol. **8**, 46 (2013).
- [9] A. Nickel, R. Ohmann, J. Meyer, M. Grisolia, C. Joachim, F. Moresco, and G. Cuniberti, ACS Nano **7**, 191 (2013).
- [10] F. Moresco, G. Meyer, K.-H. Rieder, H. Tang, A. Gourdon, and C. Joachim, Phys. Rev. Lett. **86**, 672 (2001).
- [11] Z. Li, C. Y. Gao, D. Su, C. Jia, and X. Guo, ACS Mater. Lett. **3**, 1484 (2021).
- [12] R. Wiesendanger, *Scanning Probe Microscopy and Spectroscopy: Methods and Applications* (Cambridge University Press, Cambridge, 1994).
- [13] G. Binnig, H. Rohrer, C. Gerber, and E. Weibel, Phys. Rev. Lett. **50**, 120 (1983).
- [14] A. Gourdon, D. G. de Oteyza, and J. Zhu, ChemPhysChem **20**, 2249 (2019).
- [15] Y. He, S. K. Gorman, D. Keith, L. Kranz, J. G. Keizer, and M. Y. Simmons, Nature **571**, 371 (2019).
- [16] T. F. Watson, B. Weber, Y.-L. Hsueh, L. C. L. Hollenberg, R. Rahman, and M. Y. Simmons, Sci. Adv. **3**, e1602811 (2017).
- [17] R. J. Driscoll, M. G. Youngquist, and J. D. Baldeschwieler, Nature **346**, 294 (1990).
- [18] E. Fomin, M. Tatarkhanov, T. Mitsui, M. Rose, D. F. Ogletree, and M. Salmeron, Surf Sci. **600**, 542 (2006).
- [19] F. Eisenhut *et al.*, Nanoscale **13**, 16077 (2021).
- [20] X. Zhang, C. Wolf, Y. Wang, H. Aubin, T. Bilgeri, P. Willke, A. J. Heinrich, and T. Choi, Nat. Chem. **14**, 59 (2022).
- [21] S. S. Sunku *et al.*, Nat. Commun. **12**, 1641 (2021).
- [22] A. Vezzoli, R. J. Brooke, S. J. Higgins, W. Schwarzacher, and R. J. Nichols, Nano Lett. **17**, 6702 (2017).
- [23] H.-H. Lin, A. Croy, R. Gutierrez, and G. Cuniberti, (Springer International Publishing, Cham, 2023), pp. 157.
- [24] D. Civita, M. Kolmer, G. J. Simpson, A.-P. Li, S. Hecht, and L. Grill, Science **370**, 957 (2020).
- [25] P. Roy, A. S. Sardjan, A. Cnossen, W. R. Browne, B. L. Feringa, and S. R. Meech, J. Phys. Chem. **12**, 3367 (2021).
- [26] T. E. Wiley, A. Konar, N. A. Miller, K. G. Spears, and R. J. Sension, J. Phys. Chem. A **122**, 7548 (2018).

- [27] C. Joachim and F. Moresco, (Springer International Publishing, Cham, 2023), pp. v
- [28] R. Robles, V. Zobač, and N. Lorente, (Springer International Publishing, Cham, 2023), pp. 41.
- [29] J. Echeverria, S. Monturet, and C. Joachim, *Nanoscale* **6**, 2793 (2014).
- [30] Y. Liu *et al.*, *J. Am. Chem. Soc.* **127**, 9745 (2005).
- [31] T. Seki, *Bull. Chem. Soc. Jpn.* **91**, 1026 (2018).
- [32] V. García-López *et al.*, *Nature* **548**, 567 (2017).
- [33] C. Ren, F. Chen, R. Ye, Y. S. Ong, H. Lu, S. S. Lee, J. Y. Ying, and H. Zeng, *Angew. Chem. Int. Ed.* **58**, 8034 (2019).
- [34] Y. Xu, J. Fei, G. Li, T. Yuan, and J. Li, *ACS Nano* **11**, 10175 (2017).
- [35] B. Voigtländer, in *Scanning Probe Microscopy: Atomic Force Microscopy and Scanning Tunneling Microscopy*, edited by B. Voigtländer (Springer Berlin Heidelberg, Berlin, Heidelberg, 2015), pp. 1.
- [36] N. Bohr, *Nature* **121**, 580 (1928).
- [37] J. R. Oppenheimer, *Phys. Rev.* **31**, 66 (1928).
- [38] R. H. Fowler and L. Nordheim, *Proceedings of the Royal Society of London. Series A, Containing Papers of a Mathematical and Physical Character* **119**, 173 (1928).
- [39] G. Gamow, *Zeitschrift für Physik* **51**, 204 (1928).
- [40] K.-H. Rieder, *CHIMIA* **66**, 8 (2012).
- [41] J. Bardeen, *Phys. Rev. Lett.* **6**, 57 (1961).
- [42] J. Tersoff and D. R. Hamann, *Phys. Rev. B* **31**, 805 (1985).
- [43] I. Lawson, *Notes and Records: the Royal Society Journal of the History of Science* **70**, 23 (2016).
- [44] R. M. Feenstra, *Surf Sci.* **299-300**, 965 (1994).
- [45] R. S. Becker, J. A. Golovchenko, D. R. Hamann, and B. S. Swartzentruber, *Phys. Rev. Lett.* **55**, 2032 (1985).
- [46] F. Moresco, G. Meyer, K.-H. Rieder, H. Tang, A. Gourdon, and C. Joachim, *Phys. Rev. Lett.* **87**, 088302 (2001).
- [47] T. Kühne, K. H. Au-Yeung, F. Eisenhut, O. Aiboudi, D. A. Ryndyk, G. Cuniberti, F. Lissel, and F. Moresco, *Nanoscale* **12**, 24471 (2020).
- [48] F. Eisenhut, C. Durand, F. Moresco, J.-P. Launay, and C. Joachim, *Eur. Phys. J. Appl. Phys.* **76**, 10001 (2016).
- [49] C. Joachim and G. Rapenne, *ACS Nano* **7**, 11 (2013).
- [50] A. van Venrooy, V. García-López, J. T. Li, J. M. Tour, and A. V. Dubrovskiy, *J. Org. Chem.* **85**, 13644 (2020).
- [51] N. Lorente and C. Joachim, in *Building and Probing Small for Mechanics*, edited by C. Joachim (Springer International Publishing, Cham, 2020), pp. 181.
- [52] P. Liljeroth, J. Repp, and G. Meyer, *Science* **317**, 1203 (2007).
- [53] B. C. Stipe, M. A. Rezaei, and W. Ho, *Phys. Rev. Lett.* **81**, 1263 (1998).
- [54] W. Auwärter, K. Seufert, F. Bischoff, D. Eciya, S. Vijayaraghavan, S. Joshi, F. Klappenberger, N. Samudrala, and J. V. Barth, *Nat. Nanotechnol.* **7**, 41 (2012).
- [55] T. Kudernac, N. Ruangsapichat, M. Parschau, B. Maciá, N. Katsonis, S. R. Harutyunyan, K.-H. Ernst, and B. L. Feringa, *Nature* **479**, 208 (2011).
- [56] Z. Hai-Gang, M. Jin-Hai, L. Qi, J. Nan, Z. Hai-Tao, G. Hai-Ming, S. Dong-Xia, and G. Hong-Jun, *Chin. Phys. B* **19**, 018105 (2010).
- [57] B. C. Stipe, M. A. Rezaei, and W. Ho, *Science* **279**, 1907 (1998).

- [58] Y. Sainoo, Y. Kim, T. Okawa, T. Komeda, H. Shigekawa, and M. Kawai, *Phys. Rev. Lett.* **95**, 246102 (2005).
- [59] G. Meyer, *Rev. Sci. Instrum.* **67**, 2960 (1996).
- [60] K. Besocke, *Surf Sci.* **181**, 145 (1987).
- [61] B. Voigtländer, in *Scanning Probe Microscopy: Atomic Force Microscopy and Scanning Tunneling Microscopy*, edited by B. Voigtländer (Springer Berlin Heidelberg, Berlin, Heidelberg, 2015), pp. 65.
- [62] A. Mugarza, R. Robles, C. Krull, R. Korytár, N. Lorente, and P. Gambardella, *Phys. Rev. B* **85**, 155437 (2012).
- [63] P. Li and F. Ding, *Sci. Adv.* **8**, eabq2900 (2022).
- [64] D. Nečas and P. Klapetek, *Open Phys.* **10**, 181 (2012).
- [65] F. Moresco and A. Gourdon, *Proc. Natl. Acad. Sci.* **102**, 8809 (2005).
- [66] M. Schied, D. Prezzi, D. Liu, P. Jacobson, S. Corni, J. M. Tour, and L. Grill, *J. Phys. Chem. C* **126**, 9034 (2022).
- [67] D. Mailly and G. Faini, (Springer International Publishing, Cham, 2020), pp. 41.
- [68] C. Joachim, (Springer International Publishing, Cham, 2020), pp. 1.
- [69] J. Yang, J. Deng, C. Troadec, T. Ondarçuhu, and C. Joachim, *Nanotechnology* **25**, 465305 (2014).
- [70] W.-H. Soe, C. Troadec, C. Manzano, J. Deng, F. Ample, Y. Jianshu, and C. Joachim, (Springer International Publishing, Cham, 2015), pp. 187.
- [71] M. D. Alvey, J. T. Y. Jr., and K. J. Uram, *J. Chem. Phys.* **87**, 7221 (1987).
- [72] F. Chiaravalloti, L. Gross, K.-H. Rieder, S. M. Stojkovic, A. Gourdon, C. Joachim, and F. Moresco, *Nat. Mater.* **6**, 30 (2007).
- [73] C. Manzano, W. H. Soe, H. S. Wong, F. Ample, A. Gourdon, N. Chandrasekhar, and C. Joachim, *Nat. Mater.* **8**, 576 (2009).
- [74] W.-H. Soe, S. Srivastava, and C. Joachim, *J. Phys. Chem.* **10**, 6462 (2019).
- [75] W.-H. Soe, M. Kleinwächter, C. Kammerer, G. Rapenne, and C. Joachim, *J. Phys. Chem. C* **124**, 22625 (2020).
- [76] G. S. Kottas, L. I. Clarke, D. Horinek, and J. Michl, *Chem. Rev.* **105**, 1281 (2005).
- [77] J. Gimzewski, C. Joachim, R. R. Schlittler, V. Langlais, H. Tang, and I. Johannsen, *Science* **281**, 531 (1998).
- [78] H. L. Tierney, C. J. Murphy, A. D. Jewell, A. E. Baber, E. V. Iski, H. Y. Khodaverdian, A. F. McGuire, N. Klebanov, and E. C. H. Sykes, *Nat. Nanotechnol.* **6**, 625 (2011).
- [79] H.-P. Jacquot de Rouville, S. Adrouche, X. Bouju, J.-P. Launay, G. Rapenne, and C. Joachim, (Springer International Publishing, Cham, 2023), pp. 59.
- [80] C. Joachim, H. Tang, F. Moresco, G. Rapenne, and G. A. Meyer, *Nanotechnology* **13**, 330 (2002).
- [81] G. Jimenez-Bueno and G. Rapenne, *Tetrahedron Lett.* **44**, 6261 (2003).
- [82] M. Schunack, F. Rosei, Y. Naitoh, P. Jiang, A. Gourdon, E. Lægsgaard, I. Stensgaard, C. Joachim, and F. Besenbacher, *The Journal of Chemical Physics* **117**, 6259 (2002).
- [83] H.-P. Jacquot de Rouville, R. Garbage, A. M. Sirven, C. Kammerer, and G. Rapenne, (Springer International Publishing, Cham, 2015), pp. 65.
- [84] L. Grill, K. H. Rieder, F. Moresco, G. Rapenne, S. Stojkovic, X. Bouju, and C. Joachim, *Nat. Nanotechnol.* **2**, 95 (2007).
- [85] S.-W. Hla, *Nat. Nanotechnol.* **2**, 82 (2007).
- [86] G. J. Simpson, V. García-López, P. Petermeier, L. Grill, and J. M. Tour, *Nat. Nanotechnol.* **12**, 604 (2017).

- [87] G. Flechet, (CNRS News, 2022).
- [88] K. H. Au Yeung *et al.*, J. Phys. Chem. **11**, 6892 (2020).
- [89] K. H. Au Yeung, T. Kühne, F. Eisenhut, and F. Moresco, (Springer International Publishing, Cham, 2020), pp. 117.
- [90] G. Vives and G. Rapenne, Tetrahedron **64**, 11462 (2008).
- [91] L. Grill, M. Dyer, L. Lafferentz, M. Persson, M. V. Peters, and S. Hecht, Nat. Nanotechnol. **2**, 687 (2007).
- [92] H. H. Lin, A. Croy, R. Gutierrez, C. Joachim, and G. Cuniberti, Physical Review Applied **13**, 034024 (2020).
- [93] R. Zhao, Y.-L. Zhao, F. Qi, K. E. Hermann, R.-Q. Zhang, and M. A. Van Hove, ACS Nano **12**, 3020 (2018).
- [94] R. Zhao, F. Qi, Y.-L. Zhao, K. E. Hermann, R.-Q. Zhang, and M. A. Van Hove, J. Phys. Chem. **9**, 2611 (2018).
- [95] H.-H. Lin, J. Heinze, A. Croy, R. Gutierrez, and G. Cuniberti, (Springer International Publishing, Cham, 2020), pp. 165.
- [96] E. Sharma, R. Rathi, J. Misharwal, B. Sinhmar, S. Kumari, J. Dalal, and A. Kumar, Nanomaterials **12**, 2754 (2022).
- [97] K. H. Au-Yeung *et al.*, ACS Nano **17**, 3128 (2023).
- [98] R. Pawlak *et al.*, ACS Nano **11**, 9930 (2017).
- [99] A. Barragán, T. Nicolás-García, K. Lauwaet, A. Sánchez-Grande, J. I. Urgel, J. Björk, E. M. Pérez, and D. Écija, Angew. Chem. Int. Ed. **62**, e202212395 (2023).
- [100] G. Srivastava *et al.*, ACS Nano **17**, 3931 (2023).
- [101] J. Ren *et al.*, Nano Lett. **20**, 5922 (2020).
- [102] P. Wei, T. Menke, B. D. Naab, K. Leo, M. Riede, and Z. Bao, J. Am. Chem. Soc. **134**, 3999 (2012).
- [103] B. Lüssem, C.-M. Keum, D. Kasemann, B. Naab, Z. Bao, and K. Leo, Chem. Rev. **116**, 13714 (2016).
- [104] M. Schwarze *et al.*, ACS Appl. Mater. Interfaces **10**, 1340 (2018).
- [105] H. L. Tierney, C. J. Murphy, and E. C. H. Sykes, Phys. Rev. Lett. **106**, 010801 (2011).
- [106] S. Stolz, O. Gröning, J. Prinz, H. Brune, and R. Widmer, Proc. Natl. Acad. Sci. **117**, 14838 (2020).
- [107] Y. Kim, K. Motobayashi, T. Frederiksen, H. Ueba, and M. Kawai, Prog. Surf. Sci. **90**, 85 (2015).
- [108] Y. Kim, T. Komeda, and M. Kawai, Phys. Rev. Lett. **89**, 126104 (2002).
- [109] H. S. Leff and A. F. Rex, Am. J. Phys. **58**, 201 (1990).
- [110] *Maxwell's Demon*
Entropy, Information, Computing (Princeton University Press, 1990).
- [111] J. V. Koski, V. F. Maisi, J. P. Pekola, and D. V. Averin, Proc. Natl. Acad. Sci. **111**, 13786 (2014).
- [112] R. P. Feynman, *The Feynman lectures on physics* (Reading, Mass. : Addison-Wesley Pub. Co., c1963-1965., 1963).
- [113] M. Smoluchowski, *Experimentell nachweisbare, der üblichen Thermodynamik widersprechende Molekularphänomene* 1912).
- [114] Y. Masuyama, K. Funo, Y. Murashita, A. Noguchi, S. Kono, Y. Tabuchi, R. Yamazaki, M. Ueda, and Y. Nakamura, Nat. Commun. **9**, 1291 (2018).
- [115] I. Walker, Acta Biotheoretica **25**, 103 (1976).

- [116] M. O. Scully, M. S. Zubairy, G. S. Agarwal, and H. Walther, *Science* **299**, 862 (2003).
- [117] J.-P. Launay, in *From Non-Covalent Assemblies to Molecular Machines* (2010), pp. 379.
- [118] R. L. Burwell, Jr. and R. G. Pearson, *J. Phys. Chem.* **70**, 300 (1966).
- [119] J. B. Dence, *J. Chem. Educ.* **49**, 798 (1972).
- [120] N. Koumura, R. W. J. Zijlstra, R. A. van Delden, N. Harada, and B. L. Feringa, *Nature* **401**, 152 (1999).
- [121] A. Kazaryan, J. C. M. Kistemaker, L. V. Schäfer, W. R. Browne, B. L. Feringa, and M. Filatov, *J. Phys. Chem. A* **114**, 5058 (2010).
- [122] D. R. Yarkony, *J. Phys. Chem. A* **105**, 6277 (2001).
- [123] B. G. Levine and T. J. Martínez, *Annu. Rev. Phys. Chem.* **58**, 613 (2007).
- [124] T. Kumagai, F. Hanke, S. Gawinkowski, J. Sharp, K. Kotsis, J. Waluk, M. Persson, and L. Grill, *Nat. Chem.* **6**, 41 (2014).
- [125] J. Homberg, A. Weismann, R. Berndt, and M. Gruber, *ACS Nano* **14**, 17387 (2020).
- [126] Q. Shen, H.-Y. Gao, and H. Fuchs, *Nano Today* **13**, 77 (2017).
- [127] K. H. Au-Yeung, T. Kühne, D. Becker, M. Richter, D. A. Ryndyk, G. Cuniberti, T. Heine, X. Feng, and F. Moresco, *Chem. Eur. J.* **27**, 17336 (2021).
- [128] S. Clair and D. G. de Oteyza, *Chem. Rev.* **119**, 4717 (2019).
- [129] L. Gross, F. Mohn, N. Moll, P. Liljeroth, and G. Meyer, *Science* **325**, 1110 (2009).
- [130] J. Cai *et al.*, *Nature* **466**, 470 (2010).
- [131] F. J. Giessibl, *Rev. Sci. Instrum.* **90**, 011101 (2019).

Scientific contributions

Articles

R. Robles, V. Zobač, *K. H. Au-Yeung*, F. Moresco, C. Joachim, N. Lorente. Supramolecular chemistry based on 4-acetylbiphenyl on Au(111), *Phys. Chem. Chem. Phys.*, 2020, 22, 15208-15213

K. H. Au-Yeung, T. Kühne, F. Eisenhut, M. Kleinwächter, Y. Gisbert, R. Robles, N. Lorente, G. Cuniberti, C. Joachim, G. Rapenne, C. Kammerer, F. Moresco. Transmitting stepwise rotation among three molecule-gear on the Au (111) surface. *J. Phys. Chem. Lett.* 2020, 11, 16, 6892–6899

T. Kühne, *K. H. Au-Yeung*, F. Eisenhut, O. Aiboudi, D. A Ryndyk, G. Cuniberti, F. Lissel, F. Moresco. STM induced manipulation of azulene-based molecules and nanostructures: the role of the dipole moment. *Nanoscale*, 2020, 12, 24471-24476

K. H. Au-Yeung, T. Kühne, D. Becker, M. Richter, D. A Ryndyk, G. Cuniberti, T. Heine, X. Feng, F. Moresco. On-surface formation of cyano-vinylene linked chains by Knoevenagel condensation. *Chem. Eur. J.* 2021, 27, 17336.

K. H. Au-Yeung, T. Kühne, O. Aiboudi, S. Sarkar, O. Guskova, D. A Ryndyk, T. Heine, F. Lissel, F. Moresco. STM-induced ring closure of vinylheptafulvene molecular dipole switches on Au(111). *Nanoscale Adv.*, 2022, 4, 4351-4357.

K. H. Au-Yeung, S. Sarkar, T. Kühne, O. Aiboudi, D. A Ryndyk, R. Robles, N. Lorente, F. Lissel, C. Joachim, F. Moresco. A Nanocar and Rotor in one Molecule. *ACS Nano*, 2023, 17, 3, 3128-3134

Other publications

K. H. Au-Yeung, T. Kühne, F. Eisenhut, F. Moresco. Anchoring molecular rotors by on-surface synthesis. In: Joachim, C. (eds) *Building and probing small for mechanics. advances in atom and single molecule machines*, 2020, Springer, Cham.

T. Kühne, *K. H. Au-Yeung*, S. Sarkar, F. Moresco. Azulene Based Nanocars. In: Moresco, F., Joachim, C. (eds) *Single Molecule Mechanics on a Surface. Advances in Atom and Single Molecule Machines*, 2023, Springer, Cham.

Talks

Exploring novel on-surface synthesis pathway: Knoevenagel condensation

MGK Seminar, TU Dresden

Online (July 2021)

Nanocar Race II official presentation

Online (September 2021)

Voltage-pulse manipulation of azulene-based single molecules and dimers: the role of the dipole moment

FET Open MEMO Project workshop, C'Nano 2020

Toulouse, France (November 2021)

On surface synthesis: Cyano-vinylene linked chains via Knoevenagel Condensation

DPG Surface Science division

Regensburg, Germany (September 2022)

A nanocar and a rotor in one molecule

DPG Surface Science division

Dresden, Germany (March 2023)

Posters

LT-STM investigation of transmitting rotation between molecule-gears on Au(111)

DPG Surface Science division

Online (March 2021)

On surface synthesis: Cyano-vinylene linked chains via Knoevenagel Condensation

CRC 1415 Meeting

Online (May 2021)

On surface synthesis: Cyano-vinylene linked chains via Knoevenagel Condensation

On-surface synthesis workshop (OSS22)

Girona, Spain (September 2022)

STM induced ring closure of molecular dipole switches on Au(111)

PriOSS Symposium

Marburg, Germany (May 2023)

Outreach

Images and oral presentation contribution

“Imaging Science – Die Schönheit der Wissenschaft” Exhibition
Dresden, Germany (September 2021)

Nanocar co-pilot

The Second International Nanocar Race
Toulouse, France (July 2021)

Acknowledgement

This thesis would not have been possible without the support of many people during the last years that I would like to acknowledge here. Firstly, I would like to express my gratitude to Prof. Dr. Gianaurelio Cuniberti for giving me the support and opportunity to be part of the Chair of Materials Science and Nanotechnology.

I am grateful to work with Prof. Dr. Christian Joachim, also as my thesis referee, for his endless inspiration and enthusiasm about single molecule machines. He is a great and patient teacher in explaining complex topics in quantum mechanics both experimentally and theoretically.

I thank Prof. Dr. Lukas Eng who showed so much interest in my work and was willing to be the referee of this thesis.

I thank my supervisor Dr. Francesca Moresco for her patience, inspiration, enthusiasm, and immense knowledge. Her day-to-day guidance helped me in all the time of experiments, planning, writing, and suggestions, especially bearing the risk and taking me as her student who was working in a Bio-lab in the past and have had no prior experience in complex UHV systems and STM experiments. Her advices on my career are very valuable.

My sincere thanks to my colleagues in the Single Molecule Machines group. I am grateful to meet Dr. Frank Eisenhut, a senior lab member, who showed me the vast majority of the fundamentals in the lab, even only in a short period of time before his graduation. I thank Dr. Tim Kühne who show me his technical know-how and how to efficiently and creatively solve technical problems. I thank Suchetana Sarkar, who also share the second half of my PhD period, where we have had very fruitful discussion on everyday lab matters. There are more colleagues in the group, Dresden Center of Nanoanalysis, the chair, and the cfaed institute, who I cannot thank one-by-one, but I would like to express my gratitude to them – without them my PhD work would not run smooth, especially during the COVID-19 period.

Without the support of my family and friends, it would not be possible to finish the work. I thank my wife Yun-Yen who always gives full support on what I want to do. I thank my father and mother in Hong Kong, and my sister in Sydney, despite of the physical distance, who always keep me in their prayers and support me in any directions in my 10-year life aboard. I thank my best friend Aoyu Tan who is always patience enough to listen to my ideas on science, work, and life.

Statement of authorship

Folgende Erklärung gebe ich hiermit ab:

1. Ich versichere, dass ich die vorliegende Arbeit ohne unzulässige Hilfe Dritter und ohne Benutzung anderer als der angegebenen Hilfsmittel angefertigt habe; die aus fremden Quellen direkt oder indirekt übernommenen Gedanken sind als solche kenntlich gemacht.

2. Bei der Auswahl und Auswertung des Materials sowie bei der Herstellung des Manuskripts habe ich Unterstützung von folgenden Personen erhalten:

- a. Prof. G. Cuniberti
- b. Dr. F. Moresco
- c. Prof. C. Joachim
- d. Prof. F. Lissel
- e. Prof. N. Lorente
- f. Prof. G. Repenne
- g. Dr. D. A. Ryndyk
- h. Prof. X. Feng
- i. Prof. T. Heine

Weitere Personen waren an der geistigen Herstellung der vorliegenden Arbeit nicht beteiligt. Insbesondere habe ich nicht die Hilfe eines kommerziellen Promotionsberaters in Anspruch genommen. Dritte haben von mir keine geldwerten Leistungen für Arbeiten erhalten, die in Zusammenhang mit dem Inhalt der vorgelegten Dissertation stehen.

3. Die Arbeit wurde bisher weder im Inland noch im Ausland in gleicher oder ähnlicher Form einer anderen Prüfungsbehörde vorgelegt und ist auch noch nicht veröffentlicht worden.

4. Die Promotionsordnung der Fakultät Maschinenwesen an der TU Dresden vom 22.03.2018 wird anerkannt.